INSTITUTE
FOR
AEROSPACE STUDIES

UNIVERSITY OF TORONTO

AN INVESTIGATION OF THE NORMAL MOMENTUM TRANSFER FOR GASES ON TUNGSTEN

by

E. J. Moskal

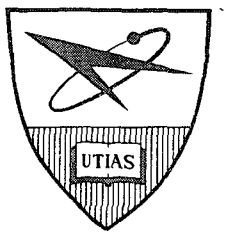

June, 1971.

UTIAS Report No. 166

AN INVESTIGATION OF THE NORMAL MOMENTUM TRANSFER FOR GASES ON TUNGSTEN

by

E. J. Moskal

Submitted May, 1971.

June, 1971.

UTIAS Report No.166

ACKNOWLEDGEMENTS

I would like to thank Professor J. B. French for initiating this project and enthusiastically supervising its progress.

The discussions that I had with fellow students and members of the UTIAS staff are gratefully acknowledged. They assisted in broadening my knowledge and in helping the progress of my work.

Thanks are in order for the excellent machining of the UTIAS Technical Support Staff, to NRC and ORF for their help in the preparation and characterization of the single crystal targets, and to J. Locke and R. Prince for their contribution in obtaining the beam velocities.

Thanks are due to my wife, Ann, for her continued support and encouragement throughout the experiment.

Financial support for the project came from the U. S. National Aeronautics and Space Administration Agency under grant NsG 367 (Supplement 4) and from the Defence Research Board and the National Research Council of Canada under contract NRCA-2731, and for myself from an NRC Studentship. This support is gratefully acknowledged.

SUMMARY

A high energy molecular beam facility, utilizing a free jet expansion, was used to obtain a near mono-energetic beam of neutral helium and argon particles. The molecular flux was obtained by stagnating the beam in a chamber upon which was mounted a mass spectrometer. The velocities of the beam particles were obtained from a metastable time-of-flight velocity analyzer. In this way, the incoming momentum of the beam was characterized. The argon atoms, in particular, had an energy which could be varied from 0.06 e.v. to 0.53 e.v.

This beam of neutral atoms impinged on a single crystal tungsten target, with the (100) face exposed to the beam. The target was mounted on a torsion balance. The rotation of this torsion balance was monitored by an optical lever, and this reading was converted to a measurement of the momentum exchange between the beam and the target.

The tungsten target was flashed to a temperature in excess of 2000°C before every "clean" run, and the vacuum levels in the final chamber were typically between 5×10^{-10} to 1×10^{-9} torr.

The momentum exchange for the helium gas - (100) tungsten surface, and the argon gas - (100) tungsten surface combination, was obtained over approximately a decade of incoming energy (for the argon gas) at angles of incidence of 0°, 30° and 41°, on both "clean" and "dirty" (gas covered) surfaces.

The results exhibited a significant variation in momentum transfer between the data obtained for the "clean" and "dirty" surfaces. The values of normal momentum accommodation coefficient for the clean surface were found to be lower than the values previously reported.

TABLE OF CONTENTS

		PAGE
	Acknowledgements	
	Summary	
	Notation	
1.	INTRODUCTION	1
2.	GENERAL OUTLINE OF PROBLEM AND PREVIOUS WORK	1
	2.1 Formulation of Problem	1
	2.2 Discussion of Experimental Procedures Used To Obtain Momentum Accommodation Coefficients	2
	2.3 Consideration of the Velocity Range	3
	2.4 Previous Experimental Work On Momentum Accommodation Coefficients	4
3.	EXPERIMENTAL APPARATUS	6
	3.1 The Beam Generating System	6
	3.1.1 Expansion (First) Chamber	6
	3.1.2 Collimation (Second) Chamber	6
	3.1.3 The Stagnation Chamber (Source) Tube)	7
	3.2 The Beam	10
	3.3 The Beam Velocity	13
	3.4 Ultra-High Vacuum Chamber	16
	3.4.1 Bayard-Alpert Gauge Calibration	17
	3.4.2 Mass Spectrometer	18
	3.4.3 Calibration of the Mass Spectrometer vs. B.A.G.	18
	3.5 The Optical Lever	19
	3.6 Torsion Balance	19
	3.6.1 Construction of the Balance	19
	3.6.2 Physical Parameters of the Balance	20
	3.6.3 Targets	21
	3.6.4 Caging Fixture	21
	3.6.5 Target Temperature	22
	3.6.6 Damping of the Torsion Balance	23
	3.7 Operation of Combined Optical Lever and Torsion Balance	23
	3.8 The Bulk and Surface State of the Tungsten Targets	24
	3.8.1 The Polycrystalline Target	24
	3.8.2 The Single Crystal (100) Target	25
	3.8.2.1 Surface Faceting	25
	3.8.2.2 Carbon on Surface	26
	3.8.2.3 Hydrogen on Surface	27

		PAGE
	3.9 Retarding Field Diode	27
4.	EXPERIMENTAL RESULTS	32
	4.1 "Dirty" Surface Results	33
	4.2 Clean Surface Results	35
	4.2.1 Trapping	37
	4.3 Helium Results	38
	4.4 Normal Momentum Accommodation	39
	4.5 Comparison with Theoretically Calculated Normal Momentum Accommodation Coefficients	41
5.	CONCLUSIONS	42
	REFERENCES	44
	APPENDIX	
	TABLE	
	FIGURES	

NOTATION

A_c	Area of orifice of the collimator
A_s	Area of orifice of skimmer
C	Torsional constant of fibre
c_m	Most probable random molecular speed
$\bar{c}$	Mean random molecular speed
d_*	Minimum nozzle diameter
F_n	Particle flow through the nozzle
I	Beam flux
I	Moment of inertia
I_A	Anode current of retarding field diode
^oK	Degrees Kelvin
K	Clausing's factor
Kn	Knudsen number
k	Boltzmann constant
L	Separation distance
M_f	Freezing Mach number
m	Mean molecular mass
n	Number density of gas particles
N_c	Number of molecules at collimator
P	Pressure
P	Normal momentum flux
S_{max}	Position of maximum in beam intensity
T	Temperature
t	Time
V	Volume
V	Voltage

X_m	Position of Mach disc

Greek Symbols

α	Thermal accommodation coefficient
γ	Specific heat ratio
γ	Secondary electron yield
θ_i	Angle of incidence
θ_r	Angle of reflection
λ	Mean free path
ρ	Density
σ	Tangential momentum accommodation coefficient
σ'	Normal momentum accommodation coefficient
Φ	Work function

Subscripts

A	Anode
b	Background
c	Collimator
c	Cold
e	Emitter
H	Hot
i	Incident
o	Stagnation conditions
r	Reflected
s	Skimmer
v	Volume
w	Wall
1	First (expansion) chamber
2	Second (collimation) chamber
3 or uhv	Third (ultra-high vacuum) chamber
ll	Parallel

1. INTRODUCTION

In considering upper atmospheric flight problems (concerning satellite aerodynamics), it is necessary to deal with highly rarefied gases. In this flow regime, the aerodynamic parameters are governed by gas-surface interactions. Measurement devices on the satellites for upper atmosphere research, and for flying through rarefied planetary atmospheres, are also affected by the mechanisms involved in gas-surface interactions. The satellite velocities involved in passing through the upper atmosphere of the earth, are equivalent to a gas particle approaching a surface with a velocity on the order of 8 Km/sec. (approximately 9 e.v. for N_2). Energies in the range of 2-100 e.v. encompass those typical of chemisorption, sputtering, penetration, and other processes at a surface, and also of gas-gas reactions such as excitation, dissociation, ionization and chemical reactions.

Thus, it becomes mandantory to look at the fundamental concepts involved in molecular transfer properties. Using uncharged, monatomic particles in free molecular flow, it may be possible to obtain basic information on the physics of interaction of gas particles with a solid boundary. To this end, it is hoped that the information on total momentum transfer obtained by this experiment under well-characterized conditions, will aid in the experimental validation of theoretical models of gas-surface interactions in the higher energy ranges. In doing so, perhaps this work, in particular, will contribute to a better knowledge of interaction potentials, lattice dynamics, surface structure on the atomic level, and also engineering values for drag coefficients of satellites.

2. GENERAL OUTLINE OF PROBLEM AND PREVIOUS WORK

2.1 Formulation of Problem

At the present time, theoretical studies of gas-surface interactions have dealt with relatively simple systems so that the problem, as formulated, could be solved with a reasonable amount of effort. In order to obtain data which can be compared to these theoretical results, the experiment must be done under precise and highly-controlled conditions. Basically, the problem can be divided into two areas of consideration, the surface to be used, and the incoming gas beam.

The surface should be both flat and smooth down to the atomic level. The target should be of a material which can be cleaned of surface contaminants, so that the interaction is truly between the gas atom and a lattice surface atom, rather than an adsorbed contaminant atom, and the target should be at some known, constant temperature throughout the experiment. Finally, the surface exposed to the beam should have a known crystal orientation.

The incoming gas molecules should be monoenergetic at a measured velocity, and the flux should be known. This means that the incoming momentum is known, and it is not necessary to depend on momentum traps, which, due to experimental difficulties, may introduce errors in the measurement of the total incoming momentum. If the beam were composed of inert gas atoms, internal degrees of freedom and dissociation problems could be ignored, and one would have less problems with adsorption on the target surface. It would be preferable to study the diatomic case after the monatomic case was understood. The energy of the incoming molecules or atoms should be kept to a reasonable level so that problems of excited levels, dissociation, penetration into the

lattice, and sputtering of the target surface would not give erroneous results.

2.2 Discussion of Experimental Procedures Used to Obtain Momentum Accommodation Coefficients

The method of obtaining integrated momentum transfer to a target has normally involved the use of a torsion balance because of the low force levels. Consequently, experimental difficulties arise from fragile equipment, problems with calibrations, poor signal-to-noise levels, and various problems of a mechanical nature.

One of the first problems to solve is the necessity of having a clean surface. With a sensitive torsion balance, it would be difficult to epitaxially grow a single crystal on a target substrate, as it is necessary to heat the surface, and to measure and maintain the surface temperature within a narrow range about the predetermined absolute value for growth of a single crystal. Then, after deposition, the mass balancing of the instrument could be upset. It can also be shown that temperature gradients affect the performance of the balance. Because of the physical constraints necessary for the deposition operation, the force measurements would undoubtedly be made only after deposition ceased, and the target was free to rotate. If the background pressure were high enough, the surface of the target would become gas covered before a force measurement could be recorded.

This problem of a clean surface condition can be avoided by the use of an ultra-high vacuum system where the target can be cleaned by high temperature outgassing, and the pressure in the vacuum chamber remains low enough such that balance equilibrium can be achieved, and experimental data extracted, before a monolayer of gas can form on the surface. However, the use of an ultra-high vacuum chamber introduces other problems. The experimenter is restricted in the use of construction materials in the chamber, and the "turn-around" time after the chamber is let up to atmospheric pressure, is long.

It is also important to design the balance and its support structure so that there is no possibility of reflected molecules being re-directed from support structures near the balance (and targets) and impinging on the target.

Momentum traps have been used in conjunction with torsion balances to obtain the total incoming momentum of ion or molecular beams. This value is then used to obtain the normal momentum accommodation coefficient σ'. Because of space and weight limitations on most torsion balances, the momentum traps have been kept small. Su and Willis[1] have theoretically analyzed the effectiveness of two-dimensional momentum traps of various common shapes and dimensions. Assuming that the interior surfaces behave as diffusely reflecting surfaces, they obtained (by solving the resulting Clausing integral equation) the ratio of the reflected normal momentum flux for a momentum trap, to that of a plane, diffusely reflecting surface. All geometries resulted in an enhanced reflected normal momentum flux for the trap (in some cases, up to 16%).

Other problems can arise in the use of momentum traps. First, it is necessary to ensure that the entire beam is intercepted by the momentum trap. Secondly, there can be a problem with a specific momentum trap geometry, and the assumption that the first bounce or reflection of the gas atom is

characteristic of either specular reflection (until sufficient energy is lost on subsequent collisions deep in the trap), or of diffuse reflection, thermally accommodated to the surface. It has been shown that there is a possibility of back scattering,[2,3,4,5] or scattering with relatively high energies in a non-specular direction. Thus, a certain number of molecules can leave the trap after this first bounce, unaccommodated to the surface. As the use of momentum traps is to accommodate the molecules to the surface temperature of the trap, and have the molecules leave the trap in a cosine (diffuse) pattern, then it can be seen that errors can be introduced into the incoming normal momentum measurements.

Because of these uncertainties, the use of a momentum trap was abandoned, and the incident momentum was calculated from flux and velocity measurements (to be described later).

The beam generating equipment used in momentum exchange experiments, has involved the use of seeded or unseeded supersonic beams, ion beams, or change-exchange ion beams. In general, the seeded supersonic beams are capable of achieving neutral gas beams with relatively high fluxes, but are limited in their velocities (up to velocities corresponding to energies of 15 e.v.). Ion beams (or use of charge-exchange to produce electrically neutral molecules) have been unable to achieve high flux levels at the lower energies with a narrow velocity distribution. However, they have a very flexible energy range. The advantages and disadvantages of both of these systems are discussed in greater detail in Appendix A.

2.3 Consideration of the Velocity Range

In the energy range considered by this paper, a number of processes may occur which can affect the energy or momentum of the rebounding gas particle, and cause difficulties in an analysis of the results, and comparison with theory. Simple back-scattering (reflection) occurs at the lower energies, and this result can be easily interpreted. As incoming energies increase for the atom or ion, it is possible to obtain sputtering effects, entrapment and re-emission, and penetration [17]. The phenomenon of secondary electron emission was discussed in Appendix A, and will not be treated here.

From Appendix B, it can be concluded that for the incoming gas energies and for the surface used to obtain results for this thesis, no problem would be experienced due to sputtering. However, other investigators have operated with beams of higher energies with metal targets where significant sputtering effects would be expected. The sputtered target atoms can have an appreciable amount of momentum when compared to the incident momentum of the gas beam. Another serious effect is that the surface becomes eroded, and various crystal planes at various angles of incidence (to the nominal surface normal) are then exposed to the incoming beam. Thus, it would be difficult to draw conclusions when comparing the results of this thesis with the work of other authors, who would have had sputtering of their surfaces.

Also, from Appendix B, penetration would not be expected for the energies used for this investigation, and hence would not have an effect on the momentum transfer results.

2.4 Previous Experimental Work On Momentum Accommodation Coefficients

Until recent interest in momentum accommodation coefficients was aroused due to drag problems on satellites, there had been very little work done since the data obtained by Millikan[24]. The work to date in this field is summarized in the following section. Some of the work has been done specifically to obtain drag results for surfaces which are typical of satellite materials, and as such, little effort was expended in characterizing the surface conditions. Boring and Humphris[25,26] have obtained drag forces due to N_2 molecules impinging on surfaces of aluminum evaporated on Mylar (Echo I), aluminum on Mylar with a coating of Alodine (Echo II), and gold. The electrically neutral beam was formed by creating an N_2^+ beam at some energy level, and neutralizing the ions by charge transfer in an N_2 gas cell. The beam system was linear. Beam energies were in the range 8-200 e.v.. The force measurements were normalized by the amount of rotation of a torsional balance due to stagnating the beam in a momentum trap. The surfaces were rough, uncharacterized, and gas covered. The results for all surfaces (at 0° incidence) were essentially the same.

Knechtel and Pitts[27] have obtained results for the momentum accommodation coefficients σ and σ' for Ar^+ ions on gold and aluminum surfaces. The argon ions were formed in an electrical discharge, extracted (in a system of aligned holes) then decelerated at a final plate to the desired energy. The beam system was linear, and beam energies were in the 15 to 50 e.v. range, with an energy spread of about 2 e.v.. To obtain the momentum accommodation coefficients, the flux on the target was measured by measuring the ion current on the target. The surfaces were either thin rolled sheets (of both metals) or vapour deposited metal on thin quartz discs. As the background pressure was 2×10^{-5} torr, the targets were expected to be gas covered. Surface roughness was not mentioned. It was noted by the authors that the target surface temperature could increase by over 100° K during two hours of ion-gun operation. Their experiment provided values of σ and σ' as functions of incident angle and ion energy.

Mair, Viney and Colligon[28] reported measurements of transfer of momentum from a beam of N_2^+ ions to a copper target. The N_2^+ ions were formed by electron impact in a low pressure ion source. After extraction, the ions passed through a 180° magnetic analyzer to select singly charged ions of one momentum and to remove problems with impurities and neutral molecules. Ion energies ranged from 4 e.v. to 100 e.v. as determined by a "stopping potential measurement". Over most of the energy range, the spread at half-maximum was about $\pm$ 3 e.v., but was less at lower energies. The rate of molecular impingement was determined by measuring the current to the target. The target was a piece of copper in the "as received" condition, and was probably gas covered as the vacuum chamber pressure was on the order of 10^{-7} torr. The authors discussed the extension of their N_2^+ results to a neutral N_2 beam result. They postulated that an equivalent N_2 beam would approach the surface with an additional energy of 2 e.v. and the only difference would be a slightly different recoil due to the higher energy. This would be true at 0° incidence (as for their results). However, at glancing angles of incidence, the path of the N_2^+ ion would be perturbed, causing a change in the angle of interation with the surface.

Doughty and Schaetzle[29] presented results for atmospheric air, nitrogen and argon on surfaces of aluminum and fresh varnish. The beam particles

were formed using an electron bombardment ion accelerator, neutralizing some particles, and deflecting the remaining charged particles from the beam. This beam system was also linear. Beam energies varied from 4 to 200 e.v.. No actual velocity measurements seem to have been taken, and no velocity spread was given. Momentum accommodation coefficient results were obtained by using a ratio of the fibre twist due to force on the target, to the fibre twist due to the beam impinging upon a momentum cavity. The target surface for the case of aluminum was engineering-grade aluminum (7 R.M.S. surface finish), and was in a vacuum of 7×10^{-5} to 1×10^{-6} torr.

McGinn[30,31] investigated the force transfer system for combinations of monoenergetic Ar, N_2, Kr, and O_2, on targets of gold, aluminum, brass, mica, BeCu, and silver paint under various conditions. The beam particles were formed by a supersonic expansion of pure gases from a source into a vacuum. The source was an electrically heated tantalum tube which could be heated from 280° to 2,000°K. For argon, energies in the range 0.06 to 0.4 e.v. would be expected. No velocity measurements were taken. Force ratio results (the force in the direction of the beam divided by the force on a momentum trap at normal incidence) were obtained. Background pressures were on the order of 10^{-10} torr. Basically, groupings of results were obtained. The first grouping of results were on mica, and gold plating on the mica target, concentrating mainly on the combination Ar on Au, with some N_2 and Kr results on the same Au surface for comparison. This gold surface was clean, and was optically smooth. Momentum exchange for Ar and Kr on clean silver surfaces were given. However, this vapour deposited silver surface was quite granular, the grains being "irregular in shape, with the longest dimension being for the most part between 10 and 50 microns". The next group of results concerned mainly Ar and N_2 on clean gold and aluminum, and compared the results with contaminated gold and aluminum. The final results were an attempt to ascertain if rough surfaces could be substituted for momentum traps. Target materials of aluminum, brass, beryllium copper, mica and colloidal silver painted on a mica laminate, were used. The metal targets were roughened by a liquid honing process such that the surface roughness was on the order of 5 microns. The gases used for this test were argon and nitrogen. From his Table III, no specific trends could be seen from the results. The values of his force ratio for almost all the gas-surface combinations could be encompassed by the figure 1.025 ± 0.015. Thus it was concluded that none of the above surfaces could replace a momentum trap. Surface roughness seems to have obliterated the effect of different surface materials on the momentum exchange.

Abuaf and Marsden[32] obtained values for normal momentum accommodation coefficients and normalized forces for monoenergetic argon atoms on etched aluminum foil, smooth deposited aluminum on mica, and mica. The argon beams were formed by a free-jet expansion using pure or seeded gases in the source. The essentially monoenergetic argon atoms had an energy range from 0.064 e.v. to 4.11 e.v.. The surfaces were of an engineering nature as described above, and were in a vacuum of approximately 10^{-6} torr, and thus were gas covered. Also included were ratios of deduced fluxes from a reference momentum trap and test surfaces. A null system was used for balance measurements. For the mixed beam cases, values of impinging momentum for the argon and for the helium portions were given.

Stickney[33] obtained force measurements using the gases helium, hydrogen, neon, nitrogen, argon and carbon dioxide on surfaces of tungsten, blackened

tungsten, aluminum, and platinum. The gas beams were Maxwellian beams from an effusive source. The incident beam energy was kept constant and the target temperature was varied. The test surfaces were "probably coated with oxides, oil films and adsorbed gases".

Savage and Bader[34] have investigated the normal and tangential momentum accommodation of N^+, N_2^+ and A^+ on copper and aluminum for energies from 0.5 to 4 K.e.v. at angles of incidence from 0° to 50° from target normal. The ions were formed in an rf source, magnetically analyzed to obtain the desired ions, and electrostatically focussed on the target. The energy dispersion in the beam was typically 40 e.v.. The metal targets were of an engineering type material which was cleaned and polished before insertion on the balance.

The results of these authors will be presented and compared with the results of this thesis in the discussion section at the end of this report.

3. EXPERIMENTAL APPARATUS

The apparatus used for this experiment can be discussed under three basic headings; the beam generating system, the ultra-high vacuum chamber which contains the torsion balance and related measuring equipment, and the chamber containing the metastable time-of-flight velocity analyzer. A schematic of the apparatus is given in Figure 1. Photographs of the actual apparatus are shown in Fig's. 2, 3, and 4. The details of this apparatus will be given in the following sections.

3.1 The Beam Generating System

3.1.1 Expansion (First) Chamber

The first chamber was basically a stainless steel box, 8" x 8" x 12-1/2" deep, mounted on an NRC HS-10, 4200 litre/sec unbaffled oil diffusion pump. The box had two concentric holes milled through opposing sides of the box so that the source tube (mounted on one side) and the skimmer (mounted on the opposing wall) would be in good alignment. On the other side walls, two windows were installed for viewing, and on the top, a Balzers IMR 6 ionization gauge (shielded from direct oil deposition) was mounted and used with a Balzer's IMG 2 controller to monitor the pressure P_1. P_1 was on the order of 2.0 - 2.6 x 10^{-4} torr (beam on). A line-of-sight shield was installed below the source-skimmer combination to help prevent oil molecules from condensing on these surfaces. A conical skimmer with an 0.018" diameter hole was mounted on a tube which was connected to the back wall. The skimmer had an external angle of 70°, and an internal angle of 50°. The distance from the back plate to the beginning of the skimmer was 2-1/4", and the axial length of the skimmer itself was 1-1/4", so that the distance from the skimmer entrance to the end wall was 3-1/2". Thus it was expected that the back wall would have no effect on the free jet at the skimmer entrance[35].

3.1.2 Collimation (Second) Chamber

The second chamber consisted of a QVF "Quickfit" PX6 glass cross, bolted to the first chamber. The glass cross was pumped by an Edwards F 903 1500 l/sec unbaffled oil diffusion pump. Pressures in it were also monitored by an IMR 6 ionization gauge, and were on the order of 1.4 - 1.7 x 10^{-7} no gas flow, 2.5 - 3.5 x 10^{-7} torr when gas was in the stagnation chamber, beam

off (flagged), and there was a pressure rise, ΔP, of approximately 3.5×10^{-7} torr with the molecular beam entering the collimation chamber. Both oil diffusion pumps were backed by an Edwards "Speedivac" ISC 3000 single stage mechanical pump having a nominal pumping speed of 2750 l/min..

At the far end of the collimating chamber, a 3 m.m. diameter orifice was used to stop most of the gas flow. Six inches further downstream was the final beam defining orifice having a diameter of 0.0454" (1.15 m.m.). This collimating orifice was approximately 32" from the stagnation chamber, and the collimating orifice to target distance was approximately 30". A straight-through valve was at the end of the collimation chamber so that the beam generating equipment could be started and operated without affecting the ultra-high vacuum system.

3.1.3 The Stagnation Chamber (Source Tube)

The stagnation chamber was basically composed of two pieces, the tungsten tube which was heated, and the stainless steel tube used for construction and service purposes (Fig's. 5 and 6). The tungsten tube was machined from a solid rod of 2% thoriated tungsten, 1/2" in. diameter, 2-1/2" long. From one end, a 1/4" hole was drilled down the length, almost to the end of the tube. Then the tungsten tube was reversed, and a hole was ground through the end. Just as the tool broke through, drilling was stopped, and the resulting hole ground and polished to a more circular shape. The result was a conical converging-diverging nozzle, with the minimum diameter d* being 0.00583", and the diameter at the exit plane (end of rod) being 0.0316". It was possible to grind back the end of the rod to reduce the diameter at the exit plane. For a $\gamma = 5/3$ gas, the theoretical Mach number at the exit plane (before the resulting expansion into the vacuum) was approximately M = 8. The tungsten tube was silver soldered to a stainless steel reducer which was welded to the 1" stainless steel tube (Fig. 6). The stainless steel reducer was cooled by water to prevent the silver solder from melting. The tungsten tube had a radiation shield around it, and the tungsten tube and skimmer were shielded from pump oil backstreaming by a baffle placed between them and the diffusion pump.

The stainless steel tube was 1" in diameter and 10" long. The water flow to the cooling coil near the tungsten-stainless steel joint came in through pipes in this tube. The gas heater leads were mounted in this tube, and the inlet for the gas was attached to it.

The gas and the tungsten tube were heated by a tungsten filament. The heater assembly is shown in Fig. 6. The heater filament was wound from an 0.027" diameter tungsten wire, and was held in position (both in the concentric and axial position) by a boron nitride spacer. Power was fed to the filament from an A.C. low voltage, high current power supply. The whole heater assembly could be removed and the filaments replaced, without disturbing the source-skimmer alignment or position.

The nozzle-skimmer separation was varied by means of a gearing arrangement. This arrangement operated as follows; a worm gear (driver) turned a larger trapped gear (see Fig. 6). This trapped gear had its internal diameter threaded. As it turned, it advanced or pulled back a 1" length of threaded tube locked to the 1" diameter stainless steel tube. A key and keyway arrangement prevented the stainless steel tube from rotating. One rotation of the worm gear advanced (or withdrew) the source by 0.0005".

Gas was supplied to the stagnation source chamber at a constant mass flow rate. The gas train was as follows; the gas was obtained from standard high purity gas bottles, having typical impurity levels of 10 p.p.m. O_2, 5-6 p.p.m. H_2O and 0.1 p.p.m. CO_2. Three separate cylinders were used (one for each gas, pure helium, pure argon, and the 10.3% argon, 89.7% helium mixture). The bottle pressures were on the order of 2500 psi for the pure helium gas, and over a period of 3 runs, only varied by an average of 7 psi. This pressure drop included purging procedures to ascertain no other remnant gases were in the source chamber. Thus over any given run, the bottle pressure did not vary appreciably. The bottle pressure regulator was used to reduce the gas pressure to 50 psi. The next items in the gas train were a shut-off valve, and a Nupro B-2SA needle valve which was left at a constant setting (undisturbed). This system was used to supply a constant mass flow to the stagnation tube. The pressures which built up in the stagnation tube were read by a Wallace and Tiernan absolute pressure gauge (0-200 mmHg) and a Heise gauge (0-100 psia). Typical values for the stagnation pressures at room temperature were as follows; pure argon, P_o = 160 mmHg; pure helium, 77 mmHg, and for 10.3% argon - 89.7% helium, 89 mmHg.

Since there was a constant mass flow to the stagnation tube, the approximate temperature of the gas (when heated) could be derived by monitoring the pressure of the gas. The appropriate relation is given by

$$\frac{T_{o_H}}{T_{o_C}} = \left(\frac{d_{*_H}}{d_{*_C}} \right)^4 \left(\frac{P_{o_H}}{P_{o_C}} \right)^2 \qquad (1)$$

The non-dimensionalizing temperature and pressure values were taken to be those for room temperature conditions. The value of d_* was assumed to vary only because of thermal expansion when the source was heated. The theoretical value of $(d_{*_H}/d_{*_C})^4$ varied from 1 at room temperature, to 1.03 at 1000°K.

Govers, LeRoy and Deckers[36] have investigated the discharge coefficient versus Reynolds number Re, based on the experimental flow and viscosity for stagnation conditions, The results exhibited a large variation in discharge coefficient as Re increased, and a variation in behaviour with increased temperature. Based on the theoretical flow for the operating conditions of this experiment, the Reynolds numbers for room temperature conditions were 380 for the argon case, and 65 for the helium case. From Ref. 36, for the above range of operating conditions, the discharge coefficient could vary for both argon and helium on heating the source. Thus, the temperatures derived from pressure ratios were only approximate.

The temperature of the gas was varied only from room temperature to 800°K in order to avoid problems of what was believed to be carbon contamination in the beam, and carbon build-up on the nozzle throat. It was found that on heating the gas to approximately 1100°K, the source pressure began to climb rapidly at a constant heater power level (d_* became smaller). On heating to approximately 1600°K, the pressure dropped; that is, the accumulated of foreign material had been heated and desorbed from the point of minimum area of the nozzle. On heating to higher levels, another build-up of foreign material was experienced, and the filament became an open circuit. On looking at the

residue collected on a plate in front of nozzle exit, two types of material were found, a black material which disappeared on indirect heating in air (carbon probably), and a metallic substance, which was probably from the internal tungsten filament. By limiting the maximum source gas temperature to 800°K, it was found that repeatable source pressures and beam fluxes could be attained. The repeatability of the beam fluxes was within 3%. (there was less variation at higher flux levels).

The nozzle-skimmer separation was a compromise between maximum beam intensity and low pressure (P_2) in the second chamber. The beam maximum was found at an x/d_* of 122. However, as the collimation chamber pressure P_2 was quite high, it was decided to increase the source-skimmer distance to decrease the gas load into the collimation chamber. While monitoring the beam, x/d_* was increased until further increases made no appreciable difference in P_2. The beam measured in the mass spectrometer stagnation area dropped by 1%, whereas the pressure P_2 fell from the upper 10^{-6} torr levels into the 10^{-7} torr range. The source-skimmer separation was left at this x/d_* value of 149 for all the experimental runs. As can be seen in the plots of reference 36 for beam intensity vs. x/d_* for various background pressures, the decrease in intensity as x/d_* increased was small for low background pressures (in the first chamber) on the order of 2×10^{-4} torr.

The next factor to be considered was the position in maximum beam intensity as the source temperature varied. It was necessary to see if the peak could shift enough to cause a major distortion in signal levels. Using the notation of Ref. 36.

$$S_{max} \alpha P_o^{0.37} P_b^{-0.17} T_o^{-0.28} \qquad (2)$$

where S_{max} is the position of maximum beam intensity, and P_b is the background pressure. The powers in the formula have been roughly validated by experiment for argon and helium. Now, in this experiment, P_b was constant for a particular gas as T_o (and thus P_o) was varied. Thus,

$$S_{max} \alpha P_o^{0.37} T_o^{-0.28} \qquad (3)$$

Now for a constant mass flow case, $T_o \alpha (P_o)^2$ (equation 1). Therefore,

$$S_{max} \alpha T_o^{-0.1}, \text{ and } \left(\frac{S_{MAX}\ 800^\circ K}{S_{MAX}\ 300^\circ K} \right) \approx 0.91$$

As the source is heated to 800°K, the position of the maximum is expected to decrease on the order of 10%, and one does not expect the beam intensity to change radically as the source is heated (due to this effect).

The next problem to be considered concerned the fact that the maximum in this experiment occurred at such a large x/d_* setting (122), whereas most experimenters reported their maximums in the region $20 < x/d_* < 70$. Vick et al [37] have investigated the primary parameters which influenced exhaust plume size and shape, observing the free jet expansion from a Mach 1 nozzle and Mach no. > 1 nozzle. The parameters they varied involved Mach no. at the exit plane, static pressure at the exit plane, the angle of the

jet at the exit plane, and the background pressures. In general, they found that on going from a sonic nozzle to a converging-diverging nozzle, the diameter of the expanding jet decreased at a fixed distance downstream measured from the minimum area (for a constant source pressure P_o and a constant background pressure P_∞), and that the Mach disc (Riemann wave) moved further downstream. Along with this lengthening of the free jet, one would expect that the "plane of last collisions", or point of free molecule flow, would also move downstream. The maximum in beam intensity is expected to occur for skimmers positioned in the neighbourhood of this plane. Thus, for the case of the converging-diverging nozzle, where the jet is axially lengthened, and radially compressed, one would expect the position for the maximum in beam intensity to be at larger x/d_* values than for sonic orifices. Unfortunately, this fact makes comparisons difficult with the work done by other investigators (who have used sonic orifices in general).

However, some use can be made of formulae derived by other investigators for free jets emanating from sonic orifices. The information derived from these sources would have to be adjusted to take into account the size and shape of a free jet emanating from a converging-diverging nozzle as compared to a sonic nozzle. For example, one can calculate the expected location of the Mach disc, using a free jet-sonic nozzle formula, and consider the x/d_* position to be a minimum. The pressures in the first chamber of the beam generating system were 2.6×10^{-4} torr for argon at a source pressure of $P_o = 160$ torr, and 2.0×10^{-4} torr for helium at a source pressure of $P_o = 77$ torr at room temperature. Ashkenas and Sherman[38] have checked the formula

$$\left(\frac{x_M}{d_*}\right) = 0.67 \left(\frac{P_o}{P_1}\right)^{1/2} \qquad (3)$$

which gives the position of the Mach disc (independent of γ), in the region $15 \leq P_o/P_1 \leq 17{,}000$. Using this formula,

$$\left(\frac{x_M}{d_*}\right)_{ARGON_{R.T.}} = 466, \left(\frac{x_M}{d_*}\right)_{HELIUM_{R.T.}} = 414.$$

Bier and Hagena,[39] using a CO_2 beam and a 90° external angle skimmer, found that if the source-skimmer distance were greater than 2/3 the source-Mach disc distance, then the Mach disc would come out in front of the skimmer, drastically reducing the beam intensity. Thus, it can be seen that under the conditions of this experiment, where the source-skimmer distance was 149 nozzle diameters, no Mach disc (shock wave) effects would be expected.

3.2 The Beam

To characterize the beam, it was necessary to know the incoming flux, the velocity distribution, and the relative amounts of helium to argon in the mixed gas case.

To obtain the beam flux, the torsion balance was moved out of the way, and the beam was stagnated in a chamber eight inches long, one and one-half inches in diameter. The beam entered this chamber through a 3.54 m.m. diameter hole in a piece of glass, 0.0057" thick, (K = 0.963). The maximum diameter of the beam was expected to be 2.86 m.m. (or 2.55 m.m. assuming a

point source for the beam) at the entrance. A mass spectrometer was mounted on the side of this stagnation chamber. This mass spectrometer was calibrated by two methods for both the helium and argon gases. The first method involved comparison of a calibrated Bayard-Alpert gauge and the mass spectrometer. The calibration procedure for the Bayard-Alpert gauge will be given in the section dealing with the ultra-high vacuum chamber. There were many steps involved in the process, and the cumulative experimental error was expected to be high. The re-calibration, using fewer steps, involved expanding a gas in a small known volume at a high pressure, readable by a calibrated, primary standard pressure gauge, into a large known volume, giving a low pressure where a reading could be taken by the mass spectrometer. A schematic of the method used to obtain known pressure levels in the UHV tank is shown in Fig. 7. The results of this calibration method were used for the partial pressure measurements of this thesis.

One of the problems involved the accurate pressure readings over the large ranges required for this calibration. Ishii and Nakayama[40] have shown that there can be significant errors in pressure readings with McLeod gauges, due to the phenomenon of mercury streaming to the cold trap causing a pumping action. The magnitude of the effect also varied with room temperature. The work of Utterback and Griffith[41] compared a capacitance manometer to a McLeod gauge, and found that "the capacitance manometer was clearly superior to the McLeod gauge as a universal pressure sensor, and appears capable of reliable readings accurate to a few percent at 10^{-4} torr". Consequently, the pressure measurements for the calibration were taken with an M.K.S. Baratron Pressure Meter, (type 77), with the 77 H-1 head (1 m.m. full scale).

First, the stainless steel "small" volume was cleaned and degassed thoroughly. This "small" volume was flushed many times with the calibrating gas to try to ensure that the background was mainly of either the helium or the argon gas being used. To obtain the volume ratio, the helium gas was used for the expansion (so that there would be less problem of gas displaced from the stainless steel walls of the UHV chamber). A quantity of gas at a high pressure (~ 1 m.m. Hg) in the small volume was expanded into the large volume, where a pressure on the order of 2.3×10^{-3} torr was measured. Both of these pressure levels were measured by the same capacitance manometer (to reduce the error). The volume ratio $V_{\text{small tube}}/V_{\text{UHV chamber}}$ was 2.15×10^{-3}. A calculated value (based on best estimates of the physical dimensions as the internal volume of the UHV system had equipment in it, whose measurements were not precisely known) was obtained as a check. The calculated ratio, which should be accurate to approximately 5%, was 2.09×10^{-3}.

The next step was to have a lower pressure in the small volume, read the gas pressure on the Baratron, and expand this gas into the UHV sytem. The gas partial pressure in the UHV system was obtained from the volume ratio. The peak of the ion current reading of the mass spectrometer mounted on the stagnation chamber (which of course, was open to the UHV system), was recorded and compared to the true pressure levels of the desired gas.

The plot of Baratron pressure in microns, versus mass spectrometer current, is given for helium and argon in Fig. 8. The argon curve was corrected for the non-linearity of output at the higher pressure levels. The performance

of the mass spectrometer at higher argon pressures will be described in section 3.4.3, which dealt with the calibration of the mass spectrometer against a Bayard-Alpert gauge. To obtain the gas partial pressure readings, the capacitance manometer readings shown in Fig. 8 must be multiplied by the volume ratio (2.15×10^{-3}). Thus for Baratron readings of 1 to 10 microns, pressures in the UHV chamber were 2.15×10^{-6} to 2.15×10^{-5} torr. It is noted that the intercept of 0.6 on the ordinate was due to the fact that background pressure in the tube was 0.66 μ, the limit of the mechanical pump. The mass spectrometer output was linear for argon from 6×10^{-6} torr down to 5×10^{-8} torr (to be shown later), and should remain linear down to levels below 10^{-11} torr[42].

The helium results for the calibration against the capacitance manometer were linear over the pressure range where the argon results became non-linear. This effect was thought to be due to space charge effects as helium had a lower ionization cross-section, and for the same pressure, fewer ions were formed. The sensitivity for the mass spectrometer was 1.28×10^{-5} amps/torr for argon, and 3.99×10^{-6} amps/torr for helium.

The other calibration method, as previously stated, involved comparison of a calibrated Bayard-Alpert gauge with the mass spectrometer ion current reading. Both instruments were mounted on the UHV tank, and argon gas was leaked into the system through a variable leak valve. The final result was a sensitivity for the mass spectrometer within 6% of the sensitivity of the above method.

Because of the above calibration of the mass spectrometer, the number flux of the beam could be determined. From the Agardograph by French,[6]

$$IA_C = \frac{1}{K} \quad \frac{n_s \bar{c}_s A_s}{4} \qquad (4)$$

The partial pressure measured by the mass spectrometer gave the number density of the gas n_s, the area of the orifice of the stagnation chamber A_s was measured, $\bar{c}_s$ was taken for a room temperature gas, K was calculated, and A_c was the measured value of the final orifice. Thus it was possible to obtain the flux of the beam I (at the collimator), and the number of molecules of the argon or helium species colliding with the target surface.

It is necessary to investigate the assumption that the number of molecules entering the stagnation chamber is the same as the number of atoms hitting the target. A mechanism for decreasing the number of atoms in the beam as the path length increases, is beam-beam collisions, with the deflections being large enough to cause the collision partners to miss the stagnation orifice. However, Valleau and Deckers[43] have stated that as the distance downstream increase, the number of collisions rapidly diminish, and the attenuation in density approaches that due to the inverse square law. A calculation, inserting the dimensions of this experiment in the formulation of Valleau and Deckers, showed that the effect of beam-beam collisions in the path between the target and the stagnation chamber entrance, could be safely ignored.

Figures 9 and 10 show the values of the molecular flux for the pure gas and seeded beams, plotted against a stagnation pressure ratio normalized to the pressure measured for the particular room temperature gas. The flux plotted on the ordinate, was based on the diameter of the last beam defining orifice. However, for the final results, the forces were plotted on a per atom basis, removing the uncertainty of the area to use (as the mass spectrometer

results directly gave the number of molecules entering the chamber). For a beam formed from a free jet expansion, the particle flow through the nozzle, F_n [36], should approach the value

$$F_n = \frac{\pi d_*^2}{4} P_o \; T_o^{-1/2} \left[\frac{\gamma}{KM} \left(\frac{2}{\gamma+1} \right) \frac{\gamma+1}{\gamma-1} \right]^{1/2} \qquad (5)$$

For a constant mass flow, $P_o \propto T_o^{1/2}$, and thus the particle flow should remain constant. However, from Figs. 9 and 10, it is seen that the flux varied. Over the given temperature range, the flux for the pure helium beam dropped 7%, a 9% increase was seen for helium in the seeded beam case, an 8% increase for argon in the seeded beam case, and a 61% increase of the pure argon beam as the source temperature increased.

As discussed in Appendix C, there are a variety of reasons which could account for minor variations in beam flux. However, it was believed that the large variation in the pure argon beam flux as the stagnation temperature was increased, was due to condensation effects. It was further believed that although a large fraction of argon beam atoms (in the pure beam case) condensed at the lower stagnation temperatures, only a small fraction would reach the target and the flux detector, due to the small solid angle of acceptance of the beam defining orifices. It then becomes necessary to discuss the effects of the condensed particles remaining in the beam, to see if they would affect the momentum transfer results. First of all, as quoted in Appendix C, the mean velocity of the dimers was (within detection limits) equal to the mean velocity of the atoms. Secondly, the dimers would break up after a collision with the wall in the flux detector volume, and the correct number of atoms striking the target would be recorded. The final consideration would be the type of interaction of the dimer on the tungsten surface. It was concluded that either this interaction was similar to individual argon atom interactions with the surface, or that the number of dimers striking the surface was negligible, as the momentum transfer results (for example, on a clean tungsten surface at $\theta_i = 0^o$) were linear over the entire incoming velocity range. No condensation of argon was expected in the seeded case, and minimal condensation was expected for the high velocity (high temperature) range of the pure argon beam. Condensation was expected in the lower velocity range of the pure argon beam.

At room temperature, based on the collimating orifice, the pure argon beam had an intensity of 3.9×10^{18} molecules/steradian-sec., the pure helium 1.28×10^{19} molecules/steradian-sec., the argon (in the mixed beam case) 2.56×10^{18} molecules/steradian-sec., and the helium (in the mixed beam case) 4.13×10^{18} molecules/steradian-sec. The enrichment factors for the 10% argon - 90% helium beam were on the order of 3.7. These values were of the same magnitude as those found by Wang and Bauer[52] in a helium-argon mixture.

3.3 The Beam Velocity

A velocity analysis was performed on the pure argon and the argon in the seeded beam using the metastable time-of-flight equipment designed and built by Locke[8]. A pulse of electrons cross the molecular beam at right angles to it, and provide a metastable and ionized group of particles. The ions are removed, and the metastable molecules continue over a known flight base and strike an electron multiplier. The electron beam is pulsed

repetitively, and the detector counts over a 1 or 2 μsec length of time, (at specific time intervals after the original pulse), are stored in a 512 channel memory unit until enough counts are stored to obtain a statistically smooth signal. The resulting time-of-flight distribution is then converted to a velocity distribution and the average velocity and mean temperature of the molecules are found. A typical output is shown in Fig. 12A. The curve shown is for a pure argon jet, where P_o = 160 mmHg, P_1 = 2 x 10^{-4} torr, and T_o = room temperature. The time scale was 2 μsec/channel, and the gun pulse width was 25 μsec. The peak in velocity corresponded to a time of 274 μsec. The flight base was 15.21 cm. Figure 12B shows the output for a higher velocity beam, where the time scale has been expanded.

Figure 13 shows the average velocities obtained by the above apparatus (for the argon gas). A number of points are of interest. The pure argon, room temperature beam expanded to a velocity of 555 meters/sec., and the half width of the velocity distribution corresponded to a parallel temperature of T_{11} = 2.34°K (if one can assume that the temperature distribution is of a Maxwell-Boltzmann type). From a table of free-jet centre line properties for a $\gamma = 5/3$ gas, a temperature T_{11} = 2.34°K, corresponds to an argon velocity of 554.5 meters/sec, and a Mach number just over 19.

It is noted that the velocity reading could be in error by ± 1%, and thus the theoretical T_{11} deduced from it could then vary from 8°K down to zero. However, the halfwidth of the velocity (and thus the temperature) distribution was known to better than 10%; that is, the temperature distribution was the more sensitive method for obtaining the Mach number, and from the same table, would give a lower limit for the Mach number of 19.

Anderson and Fenn[44], using a rotating disc chopper and sonic orifices, investigated velocity distributions for pure argon in a free jet (for various P_o's and d_*'s) expanding from a room temperature source. From a theoretical derivation, they found that

$$M_f = 2.05 \quad \epsilon^{0.4} \quad Kn_o^{-0.4} \tag{9}$$

where ϵ is a measure of the change in mean random velocity per collision per molecule. From their experimental results, they found a relationship giving

$$M_f = 1.17 \quad Kn_o^{-0.4} \tag{10}$$

Using the above formula, the pure argon beam used in this experiment for a room temperature source at a P_o of 160 mm, should reach a M_f = 13.5, corresponding to a $T_{11} \approx 4.9$ from the theoretical curve.

Miller and Andres[53] investigated the value of M_f with P_o d_* at T_o = 300°K (argon gas). At a P_o d_* equal to the conditions of this experiment, a straight line through their experimental points gave a $M_f \approx 13$ whereas the results of Anderson and Fenn gave a value of approximately 15. The work done by Abuaf et al[54] agree with the theoretical curve found by Anderson and Fenn, as well as that done by Scott and Phipps[55]. Bier and Hagena[49] reached a high Mach number for Argon, but only at higher values of P_o d_*.

The above results obtained by other investigators for Mach numbers were obtained with a jet expanding from a converging sonic orifice, or a hole drilled in a flat plate. The results in this thesis were obtained with a conical converging-diverging nozzle, and thus may not scale the same as the Mach numbers and the values of T_{11} obtained by Ref's. 53, 54 and 55. The following argument was used to account for the lower values of T_{11} obtained in this experiment.

First, the divergent section of the nozzle slows down the rate of expansion, and more collisions are experienced. Also, as discussed in a previous section, the free jet expanding after the conical converging-diverging nozzle exit, is "compressed" radially, and "lengthened" axially. This may act to keep the overall number density near the axis higher, such that there are more collisions at the lower temperatures when compared to a free jet emanating from a sonic orifice, resulting in a lower T_{11} and a higher M_f. A sensitive indicator of the lower T_{11} and relatively higher number densities would be the fact that condensation occurs at a lower value of $P_o d_*$ (of 24 Torr-mm) than that found by Bier and Hagena (85 Torr-mm), implying a greater number of multiple body collisions. The fact that T_{11} may possibly be in error by more than the 10% due to experimental error, is immaterial to the momentum transfer results of this experiment, because even if it were in error by 100%, the difference in the bulk beam velocity would be negligible.

The argon velocity for the 10.3% argon - 89.7% helium mixed beam is given in Fig. 13. The theoretical line was drawn assuming that the gas had stagnation temperatures corresponding to that derived by the stagnation pressure ratios and that the gas expanded to $M = \infty$. As can be seen by the pure argon case, the pressure ratio was not an accurate means of obtaining the temperature ratio. Thus to discuss the velocity results for a known temperature, one must look at the room temperature case. The argon in the room temperature gas mixture case expanded to a value of 11.37×10^4 cm/sec and a $T_{11} = 2.05^oK$, whereas the u_∞ for the particular gas mixture should be 12.67×10^4 cm/sec. The gas mixture was checked by the supplier and the amount of argon was accurate to $\pm$ 1%. Thus the value of u_∞ was only accurate to this value, as this quoted value was the means of obtaining the mean weight of the mixture. The velocity slip of the argon (from the theoretical) for this experiment amounted to 10%. Abuaf et al[54] have investigated velocity slip for various mixtures of helium-argon. They have found that the ratio of the actual heavy species velocity to the theoretical continuum expansion value levelled out at approximately 0.97 (3% slip) for both a 5% argon - 95% helium, and a 10% argon - 90% helium mixture at high values of K_n^{-1} slip. From the given formula, the values of K_n^{-1} slip for the conditions of this experiment indicated that the amount of slip should be the same (3%).

Miller and Andres[53] have found a different result. From their velocity curves for gas mixtures, they found a velocity slip dependent on $P_o d_*$. Using Miller and Andres results for the conditions of this thesis where $P_o d_* = 13.2$ torr-mm, one would obtain the results shown in the following chart at $T_o = 295^oK$.

Gas Mixture	5%A-95% He	20%A-80%He
Mean Ideal Velocity U_∞ cm/sec. x 10^{-5}	1.47	1.05
Mean Velocity, Helium Component cm/sec. x 10^{-5}	1.33	0.985
Mean Velocity, Argon Component cm/sec x 10^{-5}	1.23	0.935
% Slip Argon to Helium	7.5	5.1
% Slip Argon to Ideal	16.3	11

The velocity slip of 10% for the 10% A - 95% He mixture seems to agree with Miller and Andres' results, bearing in mind that the divergent nozzle would tend to lessen slip because of the expected larger number of collisions between the helium and argon atoms.

In the present experiment for the mixed beam case, it became necessary, in an integrated momentum transfer experiment, to consider the contribution of the incoming helium momentum as compared to that for the incoming argon momentum. As was shown before, the enrichment factor was 3.7. If one assumed that the incoming helium and argon velocity were identical, then for the 10% argon-90% helium gas mixture the helium portion of the beam contained ~ 16% of the incoming momentum. However, for purposes of subtracting out the incoming helium momentum, the ideal velocity of the mixture was used for the velocity of the helium component. From the work of Miller and Andres, this assumption would be in error by some value between 6% to 10%. If it is assumed that V_{helium} is in error by 10%, then as the helium incoming momentum contribution is 16% of the total value, the result of using the above method in subtracting the helium momentum from the total value, would give the incoming argon momentum to within 2%. Thus, it was not necessary to know the incoming velocity of the helium in the mixed beam to a high degree of accuracy.

3.4 Ultra-High Vacuum Chamber

Basically, the ultra high vacuum chamber was a 20" internal diameter cylinder, four feet long, standing on end. The walls and all flanges were made of type 304 stainless steel. Pumping was provided by a 500 litre/sec. G. E. "Trio Vac" triode-ion pump, and a 5000 l/sec liquid nitrogen cooled G. E. titanium sublimation pump. Both pumps were mounted in the bottom of the stainless steel cylinder. Additional pumping could be provided by an Andonian liquid helium cryopump with a pumping speed of 2000 litres/sec. The cylinder was separated into an upper and lower chamber by a butterfly type valve. The closed conductance of the valve was found to be on the order of 2 x 10^{-2} litre/sec. Test gas or contaminating gases entered into the upper chamber through a Granville-Phillips leak valve. As the butterfly valve could separate the triode-ion and T.S.P. pumps from the upper chamber, the evolution of other gases

from the triode-ion pump due to the presence of a test gas, would be minimized. The valve was also used to screen the nude Bayard-Alpert gauge from spurious signals due to the triode-ion pump. A Granville-Phillips type L straight-through valve separated the UHV chamber from the beam apparatus. At the "rear" of the UHV chamber was mounted a stagnation chamber (discussed previously) with a mass spectrometer attached to the side of this chamber. The outer end of this chamber had a glass viewing port on it, or another Granville-Phillips type L straight through valve when the metastable time-of-flight apparatus was attached to the ultra-high vacuum chamber. It was possible to see through to the source stagnation chamber for purposes of alignment of the system components. A telescope was adjusted to the beam axis, and subsequently was used to position the collimating orifices and the target. The telescope was also used to obtain the moment arm of the balance. The other ports in the upper part of the chamber were a 2" window for observation and monitoring purposes, a roughing line with a 1" Granville-Phillips type L valve, and a port for a Bayard-Alpert gauge which was operated in the nude configuration; that is, the filaments and collectors were exposed to the chamber volume. There were electric heater elements on both the upper and lower chambers so that the chambers could be baked out and the outgassing rates of the walls reduced. The top of the cylindrical chamber was closed by a large rotating UHV flange system which contained the torsion balance, and held the optical lever. The rotating UHV seal mechanical design, and its performance, are described in Appendix D. The whole vacuum chamber was mounted on a concrete block 6-1/2" x 9' x 3' deep. This concrete was isolated from the floor of the building, so that any vibrations from the building had to be transmitted down through three feet of sand to the level on which the concrete block was sitting. The ultra-high vacuum chamber was connected to the beam generating system through a soft stainless steel bellows, 7-1/2" active length, 1" I.D. The vibration problem was further reduced by mounting the large mechanical backing pump on an isolation pad, and by connecting the pump to the beam generating system by means of a large, circular loop of 2" I.D., flexible, internally reinforced, tygon-type tubing.

3.4.1 Bayard-Alpert Gauge Calibration

A Bayard-Alpert gauge was used for accurate pressure readings, since the pump ion current reading was not sufficiently accurate for calibration purposes. The Bayard-Alpert gauge was mounted in a nude configuration; that is, the elements of the gauge were totally exposed to the chamber volume. It was noted that the triode-ion pump operation affected the gauge reading. When the gauge was open to the pump, a reading of approximately 2.1×10^{-9} torr was observed. With a flat plate shield between the gauge elements and the pump, a reading of 3×10^{-9} torr was obtained.

The calibration of the B.A.G. was accomplished by the use of a constant flow of dry N_2 gas flowing through a series of chambers having various conductances between them. Basically, a three chamber system was used. The N_2 gas was let into the first chamber through a needle valve. The gas flowed into a second chamber through a small bore tube having a diameter of 0.295 cm., and a length of 3.18 cm. The second chamber held the gauges to be calibrated. The third chamber was the triode-ion pump chamber, and the conductance between the second and third chambers was due to a circular orifice, 1.254" in diameter. The pressure in the first chamber was measured by a McLeod gauge, which could also be connected to the second chamber. The conductance of the tube was found by reading the pressures in the first and second chamber with the McLeod gauge (at high enough first and second chamber pressures) under constant flow conditions.

The flow rate Q was measured by timing a soap film moving down a pipette. Then from $Q = C_{12} (P_1 - P_2)$. The conductance C_{12} of the tube was found to be 0.104 litres/sec. The conductance C_{23} of the circular orifice was found by using the relationship

$$Q = C_{12} (P_1 - P_2) = C_{23} (P_2 - P_3)$$

where P_3 was obtained by use of the ion pump current. The value of C_{23} was found to be 62.3 litres/sec. Pressures in the micron range were used in the first chamber for ease of reading of the McLeod gauge. This resulted in P_2's on the order of 10^{-5} torr and lower. A plot of the particular gauge used (in terms of controller reading), versus N_2 pressure is given in Fig. 18. The pressure calibration was over approximately two decades (2×10^{-7} torr to 5×10^{-6} torr). The behaviour of a Bayard-Alpert gauge has been thoroughly studied, for example in the works of Ref's. 42, 58, 59, 60 and 61. Over the range of interest for this experiment (10^{-4} torr to 10^{-9} torr), the response of a B.A.G. is linear for N_2 (and other gases). Thus it is only necessary to calibrate a segment of the response of the B.A.G. to known pressures, and extend this calibration to other pressure levels.

3.4.2 Mass Spectrometer

A commercial residual gas analyzer (an Aerovac model AVAI 60° sector mass spectrometer) was used to provide information on the residual gases in the chamber, and for beam flux measurement. A sensitive electrometer (a Keithley model 640 vibrating capacitor electrometer), was used to improve the sensitivity of the spectrometer. The pre-amplifier of the electrometer was directly coupled to the Faraday cup to minimize noise. The Faraday cup and sensitive electrometer combination, rather than the use of a mass spectrometer with an electron multiplier, enabled an accurate, absolute calibration to be maintained. As mass spectrogram of the residual gases in the system, at a total pressure of approximately 7×10^{-9} torr, is given in Fig. 19. Depending on the pressure levels and the previous history of chamber treatment, the main constituent (80 to 95%) of the residual gas was hydrogen. The remainder was CO_2, CO or N_2, water, CH_4, and argon if the beam had entered the chamber recently. The water peak was high in the particular spectrogram shown in Fig. 19, as the mass spectrometer itself had not been sufficiently outgassed (normally it was approximately the same height as the mass 28 peak). The residual gases found in this system were similar to those found by other authors[62] in similar vacuum systems.

3.4.3 Calibration of the Mass Spectrometer vs. B.A.G.

The first calibration of the mass spectrometer (against the B.A.G., as opposed to the capacitance manometer method previously discussed), yielded some interesting results, discussed in this section. The first calibration was attempted with argon gas, as it was felt that this gas would give the greatest problem with displacement of other gases from the UHV chamber walls and the pumps[63]. Initially, great difficulty was found in obtaining repeatable readings when comparing the B.A.G. to the mass spectrometer for the argon gas. It was noted that for a steady leak of argon (mass spectrometer reading constant), the B.A.G. reading dropped from 5.12×10^{-7} to 4.55×10^{-7} torr over a two hour period. The mass spectrometer was then used to scan the range of masses to measure the other gases which were present. An increase in all gas

peaks was seen when argon was introduced into the chamber. H_2 increased at a faster rate than the argon. The mass peaks 16, 18 and 28 also increased substantially. It was found by trial and error that liquid nitrogen (LN_2) added to the cryopump drastically decreased the 16 peak (CH_4), and that turning off the triode-ion pump would keep the H_2 peak at a low level, with the introduction of the argon gas. Eventually, the point was reached where the main constituent was argon, and the peak height outputs were in the ratio 446/3.7/7.3/4.0 for the gases with mass numbers 40/16/4/2. The other residual gas peaks could not be detected. Figure 20 is a plot of mass spectrometer peak height reading vs. the uncorrected B.A.G. pressure controller reading. From the plot, it can be seen that the displaced gases were important up to a level of 5×10^{-8} torr, giving a high B.A.G. reading. The mass spectrometer would not "see" these other displaced gases which evolve even from a relatively clean system. A linear relationship between the two instruments was then obtained until the mass spectrometer output (for argon) became non-linear at 5×10^{-6} torr. The non-linearity at the higher pressures was ascribed to the mass spectrometer, as the B.A.G. output should remain linear up to 10^{-4} torr[61]. This non-linearity of the spectrometer was probably a space charge effect at high ion densities. At the same pressures for helium, where the ion current was lower, the mass spectrometer output was still linear.

It was also noted that the argon gas bombardment of the walls during the calibration runs helped to lower the ultimate pressures in the UHV chamber. After six calibration runs, the total base pressure in the system (read the morning after a run) dropped from 2.1×10^{-8} torr to 4.2×10^{-9} torr. This seemed to suggest that an argon gas treatment could take the place of a bake-out of the UHV system.

3.5 The Optical Lever

The optical lever was the device which was used to detect the rotation of the torsion balance. A schematic of the lever is shown in Fig. 21 and Fig. 22 is a photograph of the optical bench and the components of the lever. A description of the optical lever is contained in Appendix E. The details of the performance of the lever are described in the following paragraph.

The noise level of the lever itself (with a fixed mirror) was equivalent to a mirror rotation of 9.8×10^{-9} radians, and the sensitivity was on the order of 3.3×10^{-10} radians/microvolt. The long term drift from all sources was found to be 1.5×10^{-8} radians/minute. The output of the photocells were linear over at least 50% of the theoretical operating range from maximum to minimum illumination on the photocell. The linear portion was over the mid-portion of the operating range, and amounted to an equivalent mirror rotation of approximately 7.5×10^{-4} radians.

3.6 Torsion Balance

3.6.1 Construction of the Balance

The basic construction of the torsion balance is shown in Fig's. 23, 24, and 25. As can be seen from the figures, the whole torsion balance and supporting equipment could be removed as an intact assembly from the UHV chamber. The torsion balance support rod was directly fixed to the conflat flange. The connection between the support rod and torsion fibre holder was accomplished by a piece of boron nitride, so that the target could

be electrically floated. The torsion fibre holder was lock-nutted to the boron nitride. An electrical connection was made to the continuation of the tungsten torsion fibre which went up through the fibre holder, so that grounding of the balance could be accomplished externally. The torsion fibre was a length of tungsten wire, nominally 0.001" in diameter, with the active portion 6 cm. in length. It was attached to a cylindrical mirror mount approximately one-half inch in length. A portion of the front face of this mirror mount was shaved back to the axis of rotation so that the mirror could be mounted, and the back face of the holder had an amount of material removed so that the mirror holder was statically mass balanced. A front surfaced mirror, 3 mm. wide, 6 mm. long, 0.005" thick was attached by bending two tabs over the end of the mirror and fixing the mirror (at the ends) with a small amount of GEVAC. A stiffer fibre was used to transmit the rotation of a copper bob to the mirror. This stiff fibre was an 0.006" diameter type 304 annealed stainless steel wire, 29 cm. long. The lower end of the stainless wire was attached to a copper bob (slug) 3.2 cm. long, 7 mm. in diameter. The slug was used as a mounting platform and a weight to keep the tungsten and stainless steel wires taut. The targets were mounted on the bob by means of 3 pair of 0.010" diameter tungsten wires which gave a 3 point grip of the targets. Each pair of tungsten wire holders was spot welded together near the end. Then the thin target could be slipped between the wires and be held in place by friction. The centre of the tungsten target was nominally 1 cm. from the axis of rotation of the torsion balance.

The method of attachment of the wires of the torsion balance assured axial alignment of the wires and the balance components. This method has been fully described in Appendix F.

3.6.2 Physical Parameters of the Balance

A limit on the copper bob size was imposed by the desirability of a low moment of inertia so that the period of the balance would be reasonable, and by the strength of the fibres. A large weight was preferable to keep the wires taut. At 400°C (maximum bake-out temperature) the permissible load of the tungsten fibre was approximately 90 grams, and that of the stainless steel wire was approximately 290 grams. The copper bob was the largest weight, all other components being under 1 gram. It weighed only 10.9 grams, with the moment of inertia being the determining consideration.

Theoretically, the torsion constant for the 6 cm, 0.001" wire should be:

$$C_{.001"\ w} = 1.01 \text{ dyne-cm/radian}$$

The relative stiffness factor (r.s.f.) of the two wires, using the same theoretical formula would be r.s.f. = 145. Thus, the rotation of the copper bob was almost identical to the rotation of the mirror.

As there was some difficulty in obtaining the exact length and diameter of the torsion fibre, a calibration of the torsion fibre was undertaken. To accomplish this, the natural period of the balance was utilized, that is;

$$t_1 = 2\pi \sqrt{(I_1/C)}^{1/2} \qquad (11)$$

where I_1 = moment of inertia of the balance. A simple shape (rectangle) was then very carefully measured, weighed, and added to the copper bob. A time t_2

was determined

$$t_2 = 2\pi \cdot (I_2/C)^{1/2}$$

where $I_2 = I_1 + \Delta I$, ΔI being the added moment of inertia. By simple manipulation, I_1 and C were found to be $I_1 = 1.2899$ gm-cm^2, (with the polycrystalline target mounted), $t_1 = 7.203$ sec/cycle, and C = 0.9815 dyne-cm/radian. The rectangular piece of metal used to change the moment of inertia, was a rectangle having a mass of 2.9455 gm, and having $\Delta I = 3.561$ gm-cm^2. It has been found [70,71] that this method is capable of giving accurate values of the torsion constant C of the wire.

3.6.3 Targets

There were two types of target, both tungsten. The first test target was a piece of polycrystalline tungsten, mass 0.14295 gm, diameter 6 mm., nominally 0.010" thick. The distance from the centre of the target to the axis of rotation was 0.968 cm. The second target, with which the majority of the work was done, was a piece of single crystal tungsten with the (100) face exposed to the beam. It weighed 0.13759 gm, and also (nominally) was 6 mm in diameter, 0.010" thick. The distance from the centre of this target to the axis of rotation was 0.947 cm.

When changing the angle of the target with respect to the incoming beam, it is important to note the direction of rotation of the torsion balance with respect to the beam as the copper bob had a finite size. At an angle of attack, the reflected beam bounced away from the copper bob; that is, the well collimated incoming beam passed close to the bob, the wider spread, outgoing beam away from the bob. Thus no interference was expected. However the copper bob limited the angle of attack. Theoretically, if the beam hit the centre of the target, then the angle of attack θ_i could be as large as 67° between beam direction and target normal before the beam would be expected to hit the copper bob.

The moment arm d was obtained by the use of a telescope. This telescope had its optical axis aligned to the molecular beam path; that is, the intersection of the cross hairs in this instrument would give the centre of the beam. It was possible to translate this entire telescope horizontally ($\perp$ to the beam) until the cross hairs came to a reference point on the balance (either the outer edge of target, or outer edge of the copper bob). The motion was monitored by a dial gauge. Thus the moment arm could be accurately determined. Also, if the projected diameter of the target was measured, the angle of attack of the target to the beam could be obtained.

3.6.4 Caging Fixture

The retarding field diode, damping plates, caging fixture, and the electron bombardment filament, were attached to a plate fixed to a rod. This rod passed through the vacuum wall. The vacuum seal was made by a bellows having a capability of a 2" motion. The motion was controlled by a fixture on top of the conflat flange. Under electron bombardment or operation of the retarding field diode, the balance was caged by a 3 point pick-up mechanism, which held the balance at the bottom of the copper bob, and the ends of a 0.010" wire that passed through the top of the copper bob. The 3 point structure provided the electrical connection to the target for both electron bombardment and retarding field diode operation. The whole torsion balance assembly could be lifted up further so that the molecular beam could pass under it into the mass

spectrometer stagnation volume. The whole support structure could also be lowered sufficiently so that there was no interference when the torsion balance was in use. At this point, all the support components were well away from the target so that there was no chance of the incoming or reflected beam being interfered with. Also,the electrostatic damping plates which were attached to the support plate, could be lowered such that the dummy plate on the torsion balance could be bracketed by the damping plates, and capactive damping of the torsion balance could be accomplished.

The electron bombardment filament used to heat the target,was simply a double spiral filament mounted about 2 mm from the back face of the target when the target was caged. The power supply was basically a "brute-force" D.C. power supply, capable of giving 300 m.a. continuous output, at up to 800 volts, and could supply 10 v., 4 amps to the electron-bombardment filament. The target (whole torsion balance assembly) was biased to the high positive voltage with the filament at ground, instead of using the simpler and safer method of biasing the filament negatively and leaving the target at ground. By biasing the target positively, the electrons were preferentially attracted to the target because of its closeness to the filament. The power needed to heat the target was minimal, and the ultra-high vacuum pressure dropped immediately after turning off the electron bombardment supply. With the latter method, the electrons were sprayed over the entire volume, the pressure rose to high values (much more than the other method), and the pressure fall in the ultra-high vacuum chamber was very slow. From theoretical considerations, it was calculated that approximately 90 watts was needed to heat the target to 2000°C. A typical power setting was 185 ma, 495 volts, or ~ 92 watts.

3.6.5 Target Temperature

The target temperature was monitored by an externally mounted Ircon model 300 Radiation Thermometer, capable of reading from 230° F to 5000°F, with a response of 0.1 sec to 95% of full scale. The instrument was responsive to radiation with wavelengths in the range 2.0 to 2.6 microns. With the short focal length lens, the spot size to which the instrument responded, was approximately 0.060". The instrument was calibrated to take into account the low emmissivity of tungsten, the change in emmissivity with temperature and with wavelength, and the loss of light at the ultra-high vacuum window. For this calibration, a polycrystalline tungsten plate was subject to almost the same polishing procedure as the other targets, and mounted in a test fixture in a vacuum chamber with a tungsten, tungsten-rhenium thermocouple spot-welded to the rear of the 0.010" test target. The results of the tests are shown in Fig. 26. The "dashed" curve was obtained by calculating the value of temperature that the radiation thermometer would read using values of the total emmissivity for tungsten obtained from Ref. 72, and plotting it against a true measured temperature. The experimental readings approached the dashed line with longer heating times at higher temperatures. It was postulated that over a period of time at high temperatures, the tungsten plate became cleaner and smoother as its surface reformed, and the emmissivity of the surface became lower, causing the experimental curves to shift towards the dashed line. For an example, it can be shown that oxidized and/or rough steel has a higher emmissivity than clean and/or polished steel.

The targets were flashed to a temperature ≈ 2000°C (or 2300°K) for a few seconds before each "clean surface" run. On turning off the electron bombardment power supply the background pressure dropped very quickly to the

pre-flash value, and the temperature of the target itself (as measured by the radiation thermometer) dropped to a level of 318° F in less than 100 seconds. The value of 318° F (152° C) was an upper limit as at this level, stray radiation from room sources and filaments in the UHV chamber contributed to the "temperature" reading. No special precautions had been taken to remove this source of error as it was not significant when the high temperature measurements were being obtained. It is also noted that the previously discussed temperature measurement represented the skin temperature of the front surface in the middle of the crystal, where the molecular beam impinged on the target.

3.6.6 Damping of the Torsion Balance

A series of damping experiments were carried out as the vibrational input to the torsion balance was quite severe. Electrostatic damping similar to that used in Ref. 68 was tried, but was not found to be adequate. The long support shaft, upon which the damping plates were mounted, was not securely supported, and could vibrate. Consequently, it could act as a source of vibrational excitation of the torsion balance. Electromagnetic eddy-current damping was attempted, where the electromagnets acted upon the copper bob. It was found that the damping was not sufficient, and furthermore, there was enough residual magnetism in the material of the torsion balance such that a permanent deflection of the torsion balance was obtained.

Another method of damping involved the use of gallium as a damping liquid, as it had a low vapour pressure. A small vane was attached to the bottom of the copper bob with an 0.010" wire, and the vane was fully immersed in a cup full of gallium, so that only the 0.010" support fibre passed through the gallium surface. This method worked well as long as the surface of the gallium was clean (no dust particle, or oxide on it). Great difficulty was experienced in attempting to assemble the entire system and insert it into the vacuum chamber such that the gallium surface remained clean. If it was not, the torsion balance would take a permanent set, remaining in an arbitrary fixed torsional position.

The last (and most successful) method involved the use of Santovac 6 diffusion pump oil as a damping fluid. Santovac 6 has a vapour pressure of 7×10^{-13} torr at room temperature, and a viscosity (at room temperature) of approximately 5000 c.s.

The mechanical construction of the damping assembly was unique in that the damping fluid was held in place by capillary action in an open-ended tube surrounding the 0.006" stainless steel fibre. This tube was mounted just below the mirror holder such that the stainless steel fibre passed down its axis. The tube was filled with oil so that the upper oil surface was flat, minimizing surface tension effects. The bow-string vibration of the fibre (at the mirror) was reduced to a negligible value, the pendulum motion of the single-ended balance could be damped, and the torsional vibrational mode was almost critically damped. As can be seen in section 3.7, the signal-to-noise ratio was quite acceptable.

3.7 Operation of Combined Optical Lever and Torsion Balance

A typical trace is shown in Fig. 27. The procedure to obtain a data point was to obtain a base line (beam off) for a period of 1-1/4 minutes, and then obtain the torsion balance deflection (beam on) for a period of 1-1/4

minutes. Four such deflections were obtained for each data point. Immediately after obtaining a momentum data point, a calibration trace was taken over the same deflection range as the "force" rotation in order to obtain accurate results. Figure 27 shows the result obtained for one data point for a pure argon beam at one of the lower force levels on a nitrogen covered tungsten surface at 0^{o} incidence (beam normal to target). The noise level can be encompassed by an equivalent "rotation" of 2.55×10^{-6} radians. The signal level is 4.37×10^{-5} radians, corresponding to a force of 4.31×10^{-5} dynes. Thus, the signal-to-noise level is approximately 17:1. As the "noise" is roughly sinusoidal, the base line level can be well established, in effect, increasing the signal-to-noise level.

The noise level of the torsion balance due to Brownian motion, θ_{rms}, must be considered.

$$\theta_{rms} = \left(\frac{kT}{C}\right)^{1/2} \approx 2.1 \times 10^{-7} \text{ radians.}$$

This value is under the above noise level by a factor of 10, and thus it is expected that the Brownian motion of the balance should not be a problem.

An interesting point is shown in Fig. 28. Time histories were taken of the data points obtained. While in the mid-point of a calibration for a data point on March 28, 1970, the optical lever output started to oscillate violently. The oscillations died down to a certain extent after a period of time, but the noise levels did not return to the original levels measured before the beginning of the oscillations. The next day, the performance of the balance seemed normal for a number of tests. It was noted that when the time differences were taken into account, the start of the oscillations corresponded to the violent earthquake which occurred in Turkey on that day. From the Seismology Division (Ottawa), Buchbinder[73] found that the beginning of the earthquake in Turkey was detected in Ottawa at 21:13:50 G.M.T. (16:13:50 E.S.T.) and the time of the arrival in Toronto should have been within a minute of this. Before the arrival of the event, Buchbinder stated that the background noise consisted of waves of 6 second period. After the event, surface waves started to arrive, having a period of about 15 seconds. From the data taken in Toronto the arrival of the major disturbance occurred at approximately 16:16:00. Furthermore, it was noted that the normal balance noise was 6.4 seconds/cycle before the arrival of the disturbance, and that the abnormal, relatively large amplitude, balance noise afterwards had a period of 13.9 sec/cycle, corresponding to the surface waves mentioned above.

3.8 The Bulk and Surface State of the Tungsten Targets

3.8.1 The Polycrystalline Target

For testing purposes, an arbitrary piece of 0.010" tungsten sheet was cut into a 6 mm diameter disc, and underwent a preparation similar to that expected for the single crystal tungsten target. The surface polishing procedure is outlined in Appendix G. A typical surface contour resulting from the polishing is shown in Fig. 29.[74]. A microphoto (at 500 x magnification) of the surface of the polycrystalline sample target after the polishing procedure, is shown in Fig. 30, an electron micrograph of the surface in Fig. 31, and an x-ray diffraction pattern due to the bulk of the tungsten in Fig. 32.

This same sample was annealed for a total time of 5 minutes at

2000°C in a vacuum. The Fig's. 33, 34 and 35 taken after annealing correspond to Fig's. 30, 31 and 32 taken before annealing. It can be seen that vacuum annealing reformed both the bulk and surface structure to a high degree. Large single grains were formed as evidenced by Fig's. 33 and 35, and the surface became much smoother, as seen by Fig. 34. A scan over the entire surface showed features quite similar to those found in Fig. 34.

3.8.2 The Single Crystal (100)Target

This target (and others used at UTIAS) were all cut by fine spark planing from the same high purity zone refined tungsten boule. The discs were cut to within $\pm$ 1/2° of the (100) orientation by Metals Research Ltd., (England). The targets were electropolished on one face by the manufacturer. A typical analysis of the tungsten rod gave the following level of impurities (in parts per million); C-9, O_2-4, N_2-4, H_2-0.4, Fe-5, Mo-10.

After the receipt of the tungsten single crystals, a decision was made to subject the surface to further polishing as there were pits in it (probably from the spark cutting). The crystals were polished in a manner similar to the polishing procedure employed for the polycrystalline sample. Microphotos taken of the polished single crystal were essentially featureless at 1000 x magnification. Thus, no photograph was included for this stage of inspection. The single crystal target was then put through an annealing process to reform the surface and sub-surface damage and work-hardening. An electron-micrograph of the annealed single crystal is shown in Fig. 36. The figure is an actual photograph of the single crystal used on the torsion balance. The entire surface of the crystal was scanned, and the only odd feature (probably a low angle grain boundary of the same crystal face).is shown in Fig. 36. The work-hardening of the surface of the crystal is illustrated by the comparatively large and diffuse spots in the Laue back-reflection x-ray photograph shown in Fig. 37,[74]. Figure 38 is a photograph taken after the crystal was annealed at 2000°C in a vacuum[74]. The discussions and results of Ref. 74 for the tungsten surface showed that the surface was formed of highly ordered, but stepped, flat, single crystal (100) planes, and concluded that the percentage of molecules hitting the steps would be quite low (~ 2%). Reflected high energy electron techniques (also from Ref. 74), indicated that a well-formed surface of the (100) orientation was formed after the annealing, even in the presence of hydrogen. Even under bombardment by argon and nitrogen beams, and under repeated flashing, the crystal retained its ordered structure and no microfaceting to orientations other than the (100) orientation were recorded. It was also found that there was an absence of carbon growth at the surface.

3.8.2.1 Surface Faceting

One of the reasons for the use of a W (100) surface was its stability under high temperature treatment. Using LEED techniques, Estrup, Anderson and Danforth[75], and Estrup and Anderson[76] have shown that on exposure to various substances such as thorium and hydrogen, the clean W (100) surface could be regenerated, that is, the surface returned to its original state with no reconstruction of the surface to other planes. Anderson and Danforth[77] have shown that a W (100) surface, on being heated in an environment of oxygen, exhibited the formation of (110)facets. However, high temperature flashing to 1850°K removed these facets. The work reported by O'Keefe[74] also showed the stability of the W(100) surface.

3.8.2.2 Carbon on Surface

The next problem to deal with is the surface state. Hagstrum and D'Amico[78] have shown in their article that an atomically clean tungsten surface can be obtained by flashing the target to a temperature > 2200°K for a few seconds in a vacuum, in the absence of contaminating impurities which are soluble in a tungsten lattice. Thus, the final concern with respect to cleaning the surface, is carbon on the surface and as an impurity in the bulk tungsten, as the carbon can diffuse from the bulk to the surface.

Becker, Becker and Brandeis[79] have investigated the problem of carbon impurities in and on the surface of a tungsten ribbon. They have shown that the ribbon could be made virtually carbon free by heating it at 2200°K in an 10^{-6} torr atmosphere of oxygen, and that carbon atoms could diffuse out of the bulk to the surface. For one of the ribbons, the carbon level was reduced from 1 carbon atom per every 10^2 tungsten atoms, to 1 carbon atom per every 10^6 tungsten atoms. However, it must be kept in mind that the vacuum system was pumped by an oil diffusion pump, and some of the background gases would have been carbon containing compounds. The pressures were on the order of 1×10^{-7} torr. Singleton[80] has also shown that the carbon in a tungsten polycrystalline ribbon could be reacted with oxygen at high temperatures to reduce the carbon content of a filament. From the residual gas analysis shown, it would seem that the vacuum system was also oil diffusion pumped. As a rough rule of thumb, it was stated in Ref. 79 that the carbon concentration was reduced by a factor of 10 for every seven hours of heating of the filament in an oxygen atmosphere. Singleton found that on heating his ribbon at 2200°K in 1.2×10^{-6} torr of oxygen, the carbon monoxide evolution went through a maximum and declined to a lower level during the first seven hours of heating, and stayed at this lower level until termination of the run 130 hours later. He ascribed the lower level of CO evolution to sources other than the tungsten ribbon. Using the rule of thumb proposed by Becker et al, the concentration of carbon in Singleton's tungsten ribbon was reduced by approximately a factor of 10. This final lower carbon content level, where Singleton found that the carbon monoxide evolution was constant, was approximately equal to the carbon levels expected in the W (100) tungsten target used in this report (9 ppm carbon).

Hopkins and Pender[81] quote a reference (Zingerman and Ishchuk) stating that flashing tungsten to 3000°K was sufficient for removal of carbon and carbon compounds. Hopkins and Pender seemed to confirm this result by noting that their work function measurements were the same for either condition of cleaning by high temperature flashing, or for the heating in an oxygen environment. Chen and Papageorgopoulos[82] stated that carbon layers could not be removed by heating alone, but that depletion of the carbon layer could be accomplished by heating in oxygen. However, it seemed that their tungsten material may have been highly contaminated with carbon, although no description was given of impurity levels.

Tamm and Schmidt[83] investigated the hydrogen adsorption on a W (100) crystal, which was similar to the crystal used for this thesis. They heated their disc to approximately 1800°K for several hours in oxygen at a partial pressure of 5×10^{-6} torr, with intermittent flashing to temperatures $\geq$ 2500°K in a mercury diffusion pumped system. They found that "although some investigators have found that this treatment was necessary to remove carbon, we find that flashing the crystal in vacuum to 2500° K results in flash desorption spectra for CO, N_2 and H_2 which are indistinguishable

from those after oxygen treatment".

Further information on cleaning procedures was reported by Wei[84], who was investigating adsorption of gases on W (100) by LEED methods. He tried to clean the sample by heating at 1500° K in oxygen at 10^{-6} torr, and then to 2300° K in high vacuum. He found that heating alone to 2300° K was sufficient for the cleaning of tungsten.

Also, referring back to Ref. 74, no carbon structures were found on the surface by RHEED.

In terms of concentrations of carbon on the surface, the only data found in the literature which may be applied, concerns data found on Ni (100), and semiconductor materials. First, Blakely, Kim and Potter[85] observed carbon segregation to the (100) surface of nickel, and showed that the segregation was reversible. For sufficiently small bulk carbon concentrations, they stated that precipitation at the surface should become reversible with temperature cycling. The other point to be mentioned concerns the work of Miller and Haneman[86]. Using electron paramagnetic resonance, they estimated that the coverage of carbon on the surface of a semiconductor material was on the order of 1% of a monolayer after heating. An important point concerned the fact that for his bulk concentration of carbon ($\approx 10^{17}$ atoms/cm^3 in silicon), and for a relatively pure metal, most of the carbon on the surface came from carbon containing residual gases in his vacuum chamber.

Upon review of the experimental apparatus used by the above authors, it appeared that carbon on the surface was not a problem if the vacuum chamber did not contain hydrocarbons (from the pumps), and the tungsten samples had a low initial impurity level. Thus it was concluded that carbon impurities would not affect the surface state to a measureable extent in this experiment.

3.8.2.3 Hydrogen on Surface

As stated previously, and as will be seen from retarding field diode results to be presented in section 3.9, it was expected that the tungsten surface was covered with a layer of adsorbed hydrogen. Muller[87] followed through an argument which showed that field emission studies indicated "adsorption of centers of positive charge deep in the space between the surface atoms" of the metal. Tamm and Schmidt[88] postulated that the hydrogen first absorbed as H atoms in the "valley" between 4 tungsten atoms such that every other "valley" was occupied. Then hydrogen adsorbed as molecules in the remaining "valleys" left. Also, from the experimental results of O'Keefe for argon scattering from a hydrogen covered W (100) target, the scattered flux distribution was more typical of gas scattering from a clean surface as opposed to a gas covered surface. Thus, it may be possible to say that the incoming gas molecules "see" or are affected only by the tungsten surface atoms.

3.9 Retarding Field Diode

The surface state of the target is of prime importance in the understanding of the momentum transfer results. In particular, information is required with respect to the gas adsorption on the tungsten (100) surface. A retarding field diode is capable of yielding this information, as it responds to work function changes due to adsorption of gases on a metal surface.

The method used for the diode was similar to that of Redhead[89].

The anode of the retarding field diode was of course, the tungsten target. The cathode of the diode was formed from a tungsten wire, 0.0029" in diameter, 4.6" in length. This wire passed over the target when the balance was caged, at a distance of 1.5 to 2 mm from the target. The section of the wire immediately over the target was thorium coated to enhance electron emission over the target area. The filament temperature was held constant by passing a constant current through it.

The diode current I_A in the retarding field region is given by

$$I_A = C\, T_e^{\,2} \exp\left[\frac{-e\,(\phi_A - V_A)}{k\,T_e}\right] \tag{12}$$

where C = a constant, T_e = cathode temperature, ϕ_A = the work function, and V_A = anode-cathode potential. The circuit was as shown in Fig. 39. As can be seen from it, the current (from Ohm's law) can be given by

$$I_A = \frac{V_B - V_A}{R_L} \tag{13}$$

where V_B = battery voltage. If the emitter is kept at a constant temperature then,

$$\frac{d\,V_A}{d\,\phi_A} = \left\{1 + \frac{k\,T_e}{e(V_B - V_A)}\right\}^{-1} \tag{14}$$

If $KT_e \ll e(V_B - V_A)$, then it is seen that the change in monitored anode voltage gives the change in work function of the anode. Thus, under the operating conditions mentioned above, it is possible to obtain an indication of surface contamination by monitoring the change in V_A, as surface contaminants change the work function. One method of monitoring the surface state by a retarding field diode, is to continually change V_A over a range and obtain curves as shown in Fig. 40, where a plot of V_A vs. I_A is obtained. However, this method consumed a large amount of time, and so the retarding field diode circuit was arranged to monitor the change in V_A at a constant current. Some problems were encountered because when the balance was in its caged position, the 0.010" tungsten pick-up wires merely rested in a v-groove, and so the electrical contact was of a poor quality. However, curves sensitive enough to show changes in anode potential as gas conditions were changed, were obtained, and some results (or indications) as to surface adsorption could be obtained. Results taken relatively soon after the UHV system was pumped down from atmospheric conditions, are shown in Fig. 41 (that is, the complete torsion balance assembly had been exposed to room conditions). Curve No.1 (not shown) was taken after a test flash of the surface (heating of the target) in order to check the operation of the equipment. Curve No. 2 was obtained after a hot, relatively long (10 second) heating of the button. The pressure P_{uhv} was 3.2×10^{-8} torr. Curve No. 3 was not shown as a malfunction occurred. After flashing the target again, curve No. 4 was taken for a P_{uhv} of 2.8×10^{-8} torr.

Curve No.5 was recorded after a higher target temperature was obtained ($> 2000^{\circ}$ C). With each successive flash, the lower area of the torsion balance was being cleaned (outgassed) and also the total pressure was falling. It seemed that the target needed to be flashed repetitively after being exposed to a room air environment, to obtain the normally observed anode potential variation. The residual gases in the UHV may also have contributed to the abnormal anode potential behaviour. The titanium sublimation pump was started and the pressure fell to 7.4×10^{-9} torr. After more cleaning, the target was again flashed and curve No.8 was obtained. This r.f.d. curve approached "normal"; that is, it varied in a manner similar to that observed from previous experience with the retarding field diodes. In the first 20 to 50 seconds on the plots, one can see a short term variation due to the effect of heating the target. This initial behaviour, of course, was ignored in the analysis of the r.f.d. curves.

It is also necessary to show the effects of different gases adsorbed on the tungsten (100) single crystal surface. The pure gases which should be investigated are H_2 (most important), N_2, CO, CO_2, Ar, NH_3, and O_2.

The simultaneous adsorption of H_2 along with the other gases should also be investigated.

Typical pressure levels in the vacuum system were obtained from the use of the mass spectrometer data shown in Fig. 19. Using the helium calibration for the mass spectrometer and assuming that the transmission for mass 2 was approximately the same as for mass 4,[90] then the partial pressure level for H_2 was approximately 1.5×10^{-8} torr, and the partial pressures of the other major gases were on the order of 1.2×10^{-9} torr for mass 28, and 2.3×10^{-9} torr for mass 18. These pressure levels were lower when all pumps were operating, such that the Bayard-Alpert gauge (B.A.G.) read 1×10^{-9} torr and lower; that is, the above levels should decrease by about 6/7 to partial pressures of approximately 2.1×10^{-9} torr for H_2, 1.7×10^{-10} torr for mass 28 (CO and N_2), and 3.3×10^{-10} torr for H_2O.

The ultra high vacuum system was left for a length of time, (on the order of weeks). After this period of time, it was felt that the background gas levels had stabilized completely, such that any retarding field diode results would be characteristic of normal operating conditions. Consequently, a grouping of retarding field diode results were obtained, and the data plotted in Fig. 42.

A time-condition history of this plot is as follows below. A "flash" refers to heating the target up to a temperature in the range of 2000° C for 5 to 10 seconds. "t" is elapsed time. "LN_2" refers to liquid nitrogen, and "T.S.P." is an abbreviated form for a titanium sublimation pump.

t = 4:45 Flash No.1 Puhv = 3×10^{-8} torr $1N_2$ in T.S.P. and cryopump.

t = 5:05 Flash No.2 Puhv = 1.8×10^{-8} torr $1N_2$ in T.S.P. and cryopump.

t = 5:40 Flash No.3 Puhv = 4.2×10^{-9} torr T.S.P. on

N_2 gas admitted to a level of 3.2×10^{-8} torr at 1440 sec.

N_2 gas shutoff, at 1520 sec.

Puhv = 6.6×10^{-9} torr at 1630 sec.

t = 8:54 Flash No.4 Puhv = 4.4×10^{-9} torr T.S.P. on.Curve No.4 shows evidence of some residual N_2(did not go as far -ve)

t = 9:15 Flash No. 5 Puhv = 4.5×10^{-9} torr T.S.P. on

Pure Ar beam bombarding target at 400 sec

Pure Ar beam off at 850 sec

N_2 gas admitted at 1300 sec. The pressure stabilized at ~ 7×10^{-6} torr.

t = 9:45 Flash No.6 Puhv = 7.7×10^{-6} torr of N_2 gas during flash.

N_2 flowing during flash

N_2 off at 330 sec.

4×10^{-7} torr after gas shutoff

Flash T.S.P. at 500 sec. Puhv fell to 2.8×10^{-8} torr

t = 10:13 Flash No.7 Puhv = 1.3×10^{-8} torr Curve No.7 shows effect of N_2 in background.

To enable an easier discussion of Fig. 42, a compilation of the results of various authors for the changes in surface potential, on adsorption of various gases on a tungsten surface, are tabulated in table 1. As can be seen, there are variations in the data. For most of the following discussion, the results of Estrup and Anderson will be quoted, as they have investigated a variety of gases on a W (100) surface.

From Fig. 42, curve No.3 , that a minimum in the surface potential occurred in the region of 500-600 seconds after flashing the target. Curve No.3 was taken with a partial pressure for hydrogen on the order of 9×10^{-9} torr. Using a value of 5×10^{-6} torr-sec[94] (from table 1) as the approximate time-pressure product required for formation of a monolayer of hydrogen, it was calculated that a monolayer of hydrogen should be formed by the time t = 555 sec. Thus, it was expected that the minimum in curve No.3 was representative of a hydrogen coverage of the W (100) surface.

It was also expected that the maximum in curve No.6 was representative of nitrogen coverage. The value of $|\Delta V|$ between curves No.3 and No.6 was 1.84 volts. Estrup and Anderson found a ΔV of -0.9 volts for H_2 on W(100),[76] and + 0.65 for N_2 on W(100),[95] giving a total change $|\Delta V| = 1.55$ volts, a value which is in rough agreement with the present work.

It was necessary to investigate the causes of the upward drift of the curves No.1 and No.3 in order to determine what happened to the layer of adsorbed hydrogen on the surface, keeping in mind that the obtaining of a data point (force transfer to a "clean" W (100) surface)was begun at about the 450-550 second level, and finished at the 1050 to 1150 second level. From curve No.3, it can be seen that basically the surface was hydrogen saturated and unchanging for the length of time required to obtain a data point,especially when it is remembered that curve No.3 was taken at a total pressure of 4.2×10^{-9} torr as measured by the B.A.G., whereas the experimental momentum accommodation data points were taken at or below 1×10^{-9} torr as measured by the B.A.G.

The gradual change in the surface potential can be explained by the adsorption of other gases. From Table 1, it can be seen that the ΔV's for N_2, CO, and H_2O are + .65, -.43 and -.20 respectively, (the H_2O value is for water on polycrystalline tungsten). If any of these gases were adsorbed in any vacant sites, or displaced the hydrogen, then the ΔV could be expected to rise (that is, ΔV would shift from the -0.9 v. level toward the positive direction). It is necessary to find what can replace the hydrogen on the surface. Waclawski and Hughey[104] postulate that the reaction of water with a clean (albeit polycrystalline) tungsten surface takes place in two steps.

$$H_2O + 2W \rightarrow WH + WOH$$

After this step has gone to completion, then the reaction

$$H_2O + WH \rightarrow WOH + H_2$$

takes place, liberating molecular hydrogen. If the surface is covered with chemisorbed hydrogen (WH), then the water could liberate adsorbed hydrogen, form a WOH complex on the surface and if carried to completion, the change in surface potential ΔV could shift from -0.9 to -0.20 v. However, this argument should have the reservation on it that the integrated values for the surface potential from the different planes of a specimen of polycrystalline tungsten can behave quite differently than the values for a specimen of single crystal tungsten.

The replacement phenomena of the gases hydrogen, carbon monoxide, and nitrogen will be considered using the results of Rigby[107,108] for a polycrystalline tungsten surface, and of Estrup and Anderson[76] on a W(100) surface.

Summarizing Rigby's results, nitrogen replaced hydrogen when the hydrogen was thermally desorbed, nitrogen replaced carbon monoxide when the weakly bound α phase of CO thermally desorbed, and CO replaced hydrogen by forcing out the hydrogen and causing it to desorb. However, Singleton[109] found no evidence of replacement of one gas by the other when he investigated hydrogen and nitrogen on polycrystalline tungsten.

A monolayer of pure CO on polycrystalline W amounts to 4.7×10^{14} particles/cm^2, and a monolayer of pure nitrogen amounts to 1.5×10^{14} particles/cm^2. Thus when a tungsten surface is covered by a monolayer of nitrogen, the surface can still adsorb CO as there are 3.2×10^{14} sites/cm^2 still available for the CO. Rigby also showed that the adsorption of nitrogen was not a reversible process with the background N_2 molecules. However, CO adsorption was reversible, that is, if the background pressure of CO was dropped, then the weakly bound α phase came off the surface, whereas the more strongly bound phase would come off, but not to a great extent.

Estrup and Anderson investigated the adsorption of the gases N_2 and CO on a W (100) surface. They did not find a weakly bound "α" phase of CO on the surface. Their work generally gave the same results as Rigby's. When the surface was covered with approximately 1/2 monolayer of CO, exposure to N_2 did not change ΔV. At approximately 1/4 of a monolayer of CO, some nitrogen was adsorbed. Pre-adsorption of nitrogen did not prevent subsequent adsorption of carbon monoxide, which filled the remaining sites.

From the above discussion, it is seen that a complex reaction can take

place at the surface of a clean crystal of tungsten when gases start to adsorb, or are already adsorbed on the surface. As an aid to the understanding of the adsorption processes involved on the specific crystal used in this thesis, a short study was done on the problems associated with admitting nitrogen into this particular UHV chamber. Nitrogen gas was chosen as it was a background contaminant gas, and it was also desired to deliberately coat the surface with a monolayer of nitrogen and study the momentum transfer under these conditions. First, it was necessary to investigate the background gases found on admission of N_2 into the UHV chamber. A mass spectrogram taken when N_2 was leaked into the UHV chamber with the triode ion pump operating is shown in Fig. 43. The partial pressure for hydrogen was $\approx$ 1.17 x 10^{-6} torr, and for N_2 was $\approx$ 4.43 x 10^{-6} torr. It was assumed that the mass 28 peak was mainly nitrogen due to the relative difference in heights of mass 14 and 12, the cracking fractions of CO (at 12) and N_2 (at 14) being almost equal percentages of the parent peak. $P_{He} \approx 1.20 \times 10^{-6}$. Thus, these three gases amount to a total pressure of 6.8 x 10^{-6} torr. The B.A.G. gave an average value = 5.5 x 10^{-6} torr, or corrected to N_2, read 7.0 x 10^{-6} torr. Thus, the sum of the partial pressures were consistent with the total pressure reading.

Nitrogen gas was admitted to the UHV chamber to approximately the same pressure level, and the changes in surface potential monitored.

From curve No.5 on Fig. 42, it can be seen that nitrogen rapidly took up the available sites if hydrogen was desorbed from the surface, and remained there. Thus it was concluded that as the hydrogen desorbed from the surface of the W (100) target, either N_2 or CO could fill the vacant site, and cause a change in surface potential.

In conclusion, the retarding field diode results demonstrated that the tungsten surface was probably covered with a hydrogen layer and remained that way throughout the experiment. Bombardment of the surface with a pure argon beam did not give any change in the surface potential. It was also shown that the surface could be covered with nitrogen, for momentum transfer measurements on a gas covered surface.

4. EXPERIMENTAL RESULTS

Two sets of results were taken, one with the target not flashed, ("dirty" surface results")and one set after the target had been flashed ("clean" surface results). For the dirty surface results, the target had been thoroughly cleaned in a normal room environment, put into the vacuum chamber, and left in that state without flashing to desorb surface gases. It should be noted here that the target had been annealed before the commencement of the dirty surface results. For the clean surface results, the tungsten target was flashed to a temperature in excess of 2000°C before every run (or data point). The time required to obtain each data point was approximately 17 to 20 minutes, the first 7-10 minutes consisting of the time involved in preparing the instrumentation for data gathering. The pressure in the ultra high vacuum system was typically between 5 x 10^{-10} to 1 x 10^{-9} torr, the bulk of this gas being hydrogen. The background pressure rose by $\Delta P = 6 \times 10^{-9}$ torr when the beam was admitted into the UHV chamber. As shown in the retarding field diode results discussed in the section concerning the surface state, the tungsten surface became saturated with hydrogen and remained that way throughout the length of time required to obtain a data point. Results obtained by O'Keefe[74] under almost identical experimental conditions, seemed to indicate that the

hydrogen did not affect the scattered flux distribution from the surface, presumably because the incoming argon atoms interacted predominately with the tungsten surface atoms.

Figures 44-49 give the value of the normal momentum transfer (per molecule) of the helium and argon gases to the tungsten (100) single crystal surface (a "clean" surface for this experiment being defined as a hydrogen covered surface). On all of these figures, the solid line through the origin represents momentum transfer for completely specular reflection of the gas atoms. The line intercepting the ordinate is the theoretical result for completely diffuse reflection of the gas atoms, with the gas accommodated to the surface which is at room temperature. Completely diffuse reflection is defined as the probability of a molecule leaving the surface at a particular angle being proportional to the cosine of that angle (measured from the normal to the surface). The absolute values for the momentum transfer were estimated to be correct within an error limit of 14%. This value was obtained by summing the possible errors from each step in the experimental procedure. The actual error would be expected to be less, as the probability that each possible error would accumulate in the same direction should be low.

4.1 "Dirty" Surface Results

"Dirty" surface results were obtained for the cases where $\theta_i = 0^\circ$ and 33°, where θ_i = angle of incidence, defined as the angle between the surface normal and the incoming beam. The theoretical calculation used for comparison with these "dirty" results assumed that not only must the reflected flux distribution obey a cosine law, but also the average velocity of the reflected particles in all directions must be of a uniform value, typical of a gas fully accommodated to the tungsten surface. If the simple theoretical model does not describe the situation, then it is necessary to show that either the reflected average velocity is not uniform in all direction, with a value equal to that of a gas at the temperature of the surface, or that the assumption of a cosine distribution for reflected flux distribution is not correct.

The first point to note from Fig's. 44 and 45 is that the experimental results are lower than the diffuse reflection model results at the lower velocities. While the cumulative errors could have accounted for the discrepancy between the experimental results and the simple model, the probability was not high. As it is doubtful that the reflecting gas was supercooled, then it is necessary to assume that the reflected flux distribution was non-cosine (flattened).

As an aid to the understanding of the dirty surface results shown in Fig's. 44 and 45, a discussion of experimental reflected velocity and flux distributions measured by other investigators, and of momentum accommodation coefficients on dirty surfaces for approximately the same beam energy range utilized for this thesis, follows below.

Abuaf and Marsden[32] examined the momentum accommodation of monoenergetic argon molecular beams on "engineering" contaminated surfaces. They found that σ' was on the order of 1.12 for smooth aluminum at 0.064 e.v.. For this experiment, assuming that the theoretical completely diffuse reflection value could be used for P_w, then σ' was equal to 1.21 at 0.064 e.v.

Yamamoto and Stickney[110] have investigated the scattering of rare

gases from the (110) face of a tungsten crystal. For argon at $E_i \approx 0.065$ e.v., and incoming angle $\theta_i = 60^o$, the angular distribution of mean velocities was uniform over the range $10^o \leq \theta_r \leq 80^o$ for a surface temperature $T_s = 340^oK$, where the surface was expected to be gas covered. This measured, uniform, average velocity was slightly above the theoretical value of $\bar{u}$ (mean speed) calculated for a gas accommodated to the surface temperature of 340^o K, but the discrepancy could be accounted for by experimental error. Reflected velocity results were presented for $T_s = 610^oK$, a temperature which would not desorb all adsorbed gases from the surface. Here, a deviation in the angular distribution of mean velocities from the uniform value was seen.

Yamamoto and Stickney also investigated the reflected density patterns for both helium and argon at $E_i \approx 0.065$ e.v., $\theta_i = 60$ degrees, and the target temperature was varied from 340^oK to 2100^oK. At a target temperature of 340^oK, the reflected pattern closely followed a cosine variation, but was slightly above it. After the target temperature was raised to 610^oK (for argon) or 750^oK (for helium), a definite variation from a cosine distribution was observed. Further heating to $T_s = 2100^oK$ caused a sharp lobular pattern to be seen for the reflected distribution, and the largest peak heights (at the maximum in the distribution) were measured at this temperature.

Jakus and Hurlbut[111] have investigated the reflection of helium and argon from (100) surfaces of single crystal silver and aluminum. The angular distribution of mean velocities for argon (0.065 e.v., incoming energy) reflecting from silver at a $T_s = 296^oK$, $\theta_i = 60^o$, was uniform for the range $-30^o \leq \theta_r \leq 55^o$, and then the velocity increased marginally at angles of reflection greater than 55^o. Under similar conditions except for a surface temperature $T_s = 473^oK$, there was a definite variation in the estimated temperature associated with the reflected beam velocity, increasing to a maximum at $\theta_r \approx 48^o$. For argon at incoming energies of 0.16 e.v., $\theta_i = 60^o$, $T_s = 473^oK$, there was a large variation in reflected beam velocity, even at this surface temperature where one would expect the surface to be gas covered. The results for helium at an incoming energy of 0.17 e.v. on a silver surface at $T_s = 296^o$ K, $\theta_i = 60^o$, showed an angular variation in reflected mean velocity.

Angular variations in flux, similar to that found by Yamamoto and Stickney, were also observed in the work of Jakus and Hurlbut as the surface temperature increased.

It should be noted that most of the above work concerned measurements in the principle plane, that is, the plane defined by the incoming beam and the normal to the surface of the target. An indication as to whether the cosine distribution law for reflection from a surface with specific gas-surface temperature combinations is valid, is to look at out-of-plane measurements. McGinn[112] obtained some out-of-plane measurements of flux of reflected particles. Lobular patterns were found in the principal plane, and these were sensitive to incident particle energy. Out-of-plane measurements showed change from nearly cosine to lobular shape with increasing beam energy. The flux distribution for normal incidence was almost a cosine distribution; that is, there was a suggestion that the "normal distribution may be somewhat flattened".

In summary, it appears that the type of reflected velocity and flux distribution that one obtains may depend not only on the surface, but on the

state of cleanliness, that is, whether it is gas covered by a monolayer, or heavily covered, and also the type of beam gas. From the above discussion, if the reflected flux distribution is non-cosine, and may be somewhat "flattened", then it would be possible for σ' to be greater than 1. Unless there was some systematic error present due to the experimental apparatus used for this thesis, then the force transfer results imply a flattened flux distribution, in agreement with the above results. The next points which should be considered with respect to the "dirty" surface results for this thesis, are that the results seem to form a straight line, and that the slope of the line through the results is greater than the theoretical value. The results of Jakus and Hurlbut show very clearly that as the incoming beam energy is increased, both the angular distribution for the mean velocity and reflected density distribution patterns become more lobular with the maximum occuring in the vicinity of the specular angle of reflection. The rebounding gas atoms are less accommodated to the surface, and this effect could cause the difference in slopes. No reason has been found to account for the linearity of the results.

After all the clean surface results were obtained, the tungsten target was deliberately contaminated with nitrogen (see retarding field diode results). The normal momentum transfer for argon at 0^{o} incidence for the nitrogen covered surface is given by the open circles on Fig. 44. It is noted that these points fell on the same line as the original dirty surface results, for which the surface was poorly characterized, and the adsorbed layer could have contained various gases. It is difficult to draw a conclusion from this coincidence, which suggests that either the gas on the surface from room exposure was mainly nitrogen, or that any monolayer of gas on the surface was capable of giving similar results.

4.2 Clean Surface Results

From Fig's. 44 and 45, it can be seen that there is a large momentum transfer difference between the clean surface and the dirty surface results, all other experimental conditions being constant.

At $\theta_i = 0^{o}$ incidence (as defined from the normal), the argon normal momentum transfer for the clean surface is further removed from the theoretical specular value than for the case of $\theta_i = 29^{o}$. This can be due to two effects. The reflected flux distribution has theoretically been shown to be broader at normal incidence than at $\theta_i = 29^{o}$, and the energy transfer coefficient is theoretically higher for the 0^{o} case[114]. With the effective $T_{gas_i} > T_s$, there should be a net transfer of energy to the surface, and thus the average value of the reflected velocity would be less than that of the incident velocity, and would be less for the case $\theta_i = 0^{o}$, than for the case of $\theta_i = 29^{o}$.

It can be seen that the normal momentum transfer results for argon on the clean surface, plotted against incoming velocity formed a straight line over almost a decade of incoming energy (from 0.064 e.v. to 0.53 e.v.).

At $\theta_i = 29^{o}$, the clean surface normal momentum transfer for argon on (100) tungsten was quite close to the specular value. As shown by O'Keefe[74], the peak in the argon flux distribution was slightly supraspecular, that is, closer to the surface tangent, as predicted by the hard and soft cube models[115]. Thus, to obtain the measured high values of momentum transfer to the surface, the energy transfer coefficient would have to be low, and the reflected flux

pattern would have to be quite narrow.

From Fig. 45, it was found that on doubling the velocity, the momentum transfer results increased by slightly over a factor of two. This suggested that the collisions of the argon atoms with the tungsten surface were tending towards events having a minimum loss of energy to the surface as the velocity increased.

The difficulty in drawing inferences from published data on reflected velocity or flux distributions, is that many of the surfaces were reported to be either polycrystalline, or not well defined. In some cases, the targets were heated. If so, the gas could pick up energy from the surface, and the peak in the reflected flux distribution pattern would be shifted towards the surface normal. However, use can be made of some of the reported data. For example, in Moran, Wachman and Trilling's report[116], the velocity $\bar{v}$ of the reflected beam was very close to the velocity of the incoming beam at an angle $\theta_r = \theta_i$, although the peak in the flux was at a value $\theta_r < \theta_i$. They investigated initially monoenergetic argon beams impinging on an uncharacterized platinum foil target held at 1000°C (1300°K). The measurements were made in the principal plane. Broad lobular reflected flux distributions were found.

Yamamoto and Stickney[110] investigated reflected velocity and flux distributions using incoming monoenergetic argon, helium, neon, and krypton gas beams and a W(100) crystal target. For clean surface runs, the target was held at 2100°K. It was shown that the peak in the argon flux distribution could be predicted by the soft cube model. The argon velocity profile showed that energy from the surface was transferred to the molecules. It was also shown that the assumption of the velocity behaviour for the cube models (i.e., $V_{tangential}$ = constant) was in error. As the normal momentum exchange depends on an integrated value of the flux distribution and the velocity distribution, it can be seen that the use of the cube model would not be correct.

The work of Jakus and Hurlbut[111] showed a definite peak in each reflected velocity distribution measured over a range of angles of reflection, θ_r, where the effective incoming gas "temperature" of the beam particles was greater than the surface temperature. These peaks in the angular distribution of the velocity, corresponded (approximately) to the peak in the flux distribution. At the peak the most probable speed value was between the value of incoming and a most probable speed corresponding to a gas at the temperature of the surface.

For the clean surface results of this experiment, the percent decrement of the experimental data as compared to the theoretical specular value decreased as the incoming beam velocity increased. Jakus and Hurlbut showed an increase in magnitude of reflected velocity as the incident velocity increased, and also an increase in reflected-to-incident beam density ratio at the peak in the distribution as incident velocity increased (for the same surface temperature). The work of O'Keefe for a monoenergetic beam of argon on a W(100) surface saturated with hydrogen at room temperature, showed quite clearly the increase in peak height, the decrease of the lobe half-width, and the approximately constant value of θ_r at maximum peak height for the reflected flux distribution of the argon gas as the incoming gas energy was increased.

To summarize, the normal momentum transfer values at $\theta_i = 29°$ for the clean surface are in agreement with the trends shown by published data on reflected flux and velocity measurements on clean surfaces, and that as the incident beam velocity increases, the normal momentum transfer results move

closer to the theoretical specular values due to the fact that the reflected velocity and flux distributions become narrower and less energy is exchanged with the surface.

Figure 46 shows the normal momentum transfer for argon on the "clean" W (100) surface for $\theta_i = 41^\circ$. It is necessary to explain the non-linearity of the results (when compared to the previous results) considering basically the parameters θ_i, θ_r, V_i and V_r. Again, using O'Keefe's results, a change of V_i does not drastically change the angular position θ_r of the flux maximum. An increase in V_i does narrow the flux distribution, but as seen from this experiment for the case of $\theta_i = 29^\circ$, there was not large variation or change in the momentum transfer. V_r at $\theta_i = 41^\circ$ should basically behave in the same manner as at $\theta_i = 29^\circ$; that is, the energy transfer coefficient should theoretically decrease as θ_i increases, and V_r should be of the same magnitude as V_i. The work of Yamamoto and Stickney showed that the reflected velocity V_r behaved in a regular manner for $\theta_i = 40^\circ$, 50° and 60° for the one incoming value of V_i. The divergence of θ_r from the specular value as θ_i increases from 29° to 41° should be less than 5° [117]. The magnitudes of the above theoretical and experimental considerations do not satisfactorily explain the observed change in the transfer of momentum at 41°. Thus, one can postulate that there may be a certain amount of trapping of argon at the surface. Trapping has been predicted,[118,119,120] and one would expect that at some low enough incoming energy, the particle would not have enough energy after the initial collision with the surface to escape the field of the surface.

The energy range corresponding to the incoming normal velocity range for $\theta_i = 41^\circ$ varied from 0.036 e.v. to 0.30 e.v., and the break-point in the experimental results where the momentum transfer results started to change from diffuse reflection, occurred at about the 0.12 e.v. value. Below this value, the majority of the argon atoms appeared to be trapped. Lorenzen and Raff[121] reported a heat of adsorption of 0.0819 e.v. for argon on tungsten. This value for the heat of adsorption should approximately be equal in magnitude to the depth of the potential well above the surface. Engel and Gomer[105] from their FEM work for argon on a W(100) surface, found a binding energy of 1.9 kcal/mole. This value is equivalent to 0.082 e.v.

4.2.1 Trapping

Goodman[118] theoretically investigated the interaction of He, Ne, Ar, Kr and Xe on W in his report. The assumptions made were as follows; 1) a clean solid surface, 2) 3-D semi-infinite lattice 3) lattice temperature = 0°K, 4) 1-D Maxwellian beam (that is, an incoming gas particle strikes and leaves in the perpendicular direction) 5) head-on collision, 6) classical mechanics, and 7) a Morse potential for the gas-surface atom interaction. Using these assumptions, he found that the percentage of total energy transfer due to trapped atoms for Ar on W were 25% for a gas temperature $T = 100^\circ$ K, 12% for $T = 200^\circ$ K, and 7.1% for $T = 300^\circ$ K. The values for He on W were 0.012, 0.0022 and 0.00075 for the respective gas temperatures. Thus, the amount of trapping decreased as the incoming beam temperature increased, and there was a small trapping fraction for He on W as compared to Ar on W. The theoretical plot of sticking coefficient S(T), defined as the fraction of atoms which had more than one collision with the solid surface, was also given. S(T) for He was equal to 0 for any T beam greater than 0.16°K.

S(T) for argon on W was S(T) ≈ 0.46 at T_{beam} = 100°K, S(T) ≈ 0.27 at T = 200°K, S(T) ≈ 0.17 at T = 400°K, and slowly decreased as the beam temperature increased.

As can be seen from the Ar-W(100) results of Fig. 46, the effect of multiple collisions (or temporary adsorption) decreased as the incoming gas energy increased. This trend is in agreement with the above theoretical results.

Jackson[120,122] has investigated high energy scattering of inert gases from a W(100) surface, using classical mechanics, the surface atoms having no initial velocity. The incoming gas atom experienced a smooth attractive field and then interacted with the surface atom in a hard sphere collision. Using the experimental values listed for E_t in Jackson's paper, where E_t = energy due to the attractive field of the surface, E_o^* for this experiment (for argon) varied from 0.756 to 6.6, where $E_o^* = E_{incoming}/E_t$. For the above values of E_o^*, Jackson calculated that the absolute trapping of argon on a tungsten surface varied from approximately 1 down to 0. (i.e., the probability of trapping was 1 at E_o^* = 0.6, and was zero at E_o^* = 6).

Oman[119] showed the fraction trapped for inert gases on a silver (111) surface at 130° incidence (40° to the normal). For argon on silver, the trapping fraction decreased from 1 to zero over the equivalent source temperature range of approximately 2,000°K to approximately 20,000°K. At an incoming angle of approximately 40°, it was found in the work of this report that the fraction trapped seemed to have dropped to a low value (close to zero) at an effective source temperature of 2,500°K, a point where Oman predicts a trapping fraction of slightly under 1. The results for the trapping fraction of argon on a nickel (100) surface were also calculated to be 1 up to an incident energy of 1 e.v.[123].

Thus, it has been shown theoretically that trapping of argon (or multiple collisions with the surface) can occur for a significant portion of the incoming argon atoms at energies approximately in the range of those investigated in this thesis. As stated before, for θ_i = 41°, the incoming normal velocity range for the argon atoms corresponded to energies from 0.036 e.v. to 0.30 e.v., with the change from diffuse reflection of the argon atom occurring at approximately 0.12 e.v.

4.3 Helium Results

Figures 47 to 49 show the integrated normal momentum transfer for the helium gas - (100) tungsten surface. It is dangerous to speculate on the closeness of the clean and dirty surface results at θ_i = 0°, due to the lack of experimental data on the reflected density pattern and the reflected velocity at this angle. One might infer from reference 114 that significant broadening of the reflected pattern at θ_i = 0° may occur even on a clean metal, so that background gas adsorption on the surface would not dramatically change the momentum transfer. Also, the work of Jakus and Hurlbut on the reflection of helium from a room temperature (gas covered) silver surface showed a departure from density distribution typical of a perfectly diffuse reflection of the particles. The angular distribution of the reflected gas "temperature" corresponding to the reflected velocity, showed a variation, increasing as the specular angle was approached. This would indicate that the dirty surface momentum transfer results should be somewhat above the theoretical values obtained by use of the cosine distribution for particles completely accommodated to the surface. More work is required at this angle of attack.

However, for $\theta_i = 30^\circ$ there was a large separation of the clean and dirty surface results. From Yamamoto and Stickney's paper, $\theta_r = \theta_i$ for helium on a (100) tungsten surface at 2100°K. Smith, Saltsburg and Palmer[124] have examined the reflected distribution for helium beams on Ni (111), and compared the results to helium beams on Ag (111) and Au (111). They have found that for helium, the scattered beam was always specularly directed. Their targets were maintained at a temperature necessary for the growth of a (111) single crystals. The clean surface results of this experiment seem to be consistent with the finding of $\theta_r = \theta_i$, as the clean surface momentum transfer results were close to the theoretically derived specular results.

The momentum transfer results at $\theta_i \approx 30^\circ$ for helium on the tungsten surface can be interpreted in a manner which can show the quality of the surface. In his report, Smith [117] has shown that He scattering from a Au vapour deposited surface was very nearly cosine for a rough polycrystalline film. When the substrate was held at 560° K and a (111) plane of Au was grown epitaxially, a sharp, specularly directed, scattering distribution was observed. Furthermore, it was shown that a contaminated surface markedly increased the dispersion of the scattered helium, but there was still some evidence of specularly directed scattering. As the momentum transfer results for the "clean" case were close to the theoretical specular value, then it was concluded that the W (100) target surface was smooth, and the adsorbed hydrogen was tightly bound to the surface and did not markedly affect the results. The observed difference between the "clean" and "dirty" surface momentum transfer results are also in agreement with the results shown by Smith.

Some important insights into the simultaneous behaviour in the angular variation of flux and velocity for 0.065 e.v. monoenergetic helium atoms reflecting from an Ag (111) surface are given in the work of Fisher and Pjura[125]. The simultaneous measurement of these two parameters is, of course, important for momentum transfer results. One of the first facts that they noticed was that the maximum value of the flux distribution (at the specular reflection angle) was less for a rougher surface which was caused by deposition of Ag on a substrate which was not at the correct temperature necessary for epitaxial growth of a single crystal. For a well-ordered, clean Ag (111) surface at $\theta_i = 50^\circ$, they found that the mean reflected velocity of the helium for all measured angles of reflection, was essentially equal to the mean incoming velocity. It was found that the speed distribution at each angle did increase, but it was still well below that for a gas fully accommodated to the surface. Furthermore, a minimum value of the speed distribution (less accommodation to the surface) was found at the specular angle of reflection. For $\theta_i = 50^\circ$, they also took out-of-plane sections at $\theta_r = 40^\circ$, 50° and 60°. The lobe of the scattered flux distribution was elliptical in shape, with its principal axis coincident with the plane formed by the incident beam and the normal to the surface. The mean reflected velocity for the out-of-plane results was also found to be approximately equal to the mean incident velocity, the slight deviation being toward the fully accommodated value. From the above discussion, it would appear that for a clean surface, the momentum transfer between the helium gas-Ag surface atom should approach the theoretical specular value as calculated for the figures of this thesis.

4.4 Normal Momentum Accommodation

To facilitate comparison with other published data, the data from

this experiment was reduced to give momentum transfer values in other forms, as shown in Fig's, 50, 51 and 52, and with some modifying assumptions, these and other author's results were plotted in one form (Fig's. 53 and 54). Normal momentum transfer results are usually presented by use of the normal momentum accommodation coefficient σ', where

$$\sigma' = \frac{P_i - P_r}{P_i - P_w}$$

P_i is equal to the incident normal momentum in the beam, P_r equals the normal momentum of the reflected gas molecules, and P_w equals the average normal momentum carried away by a gas particle assuming that the gas molecules leave the surface in a diffuse cosine pattern, with a velocity distribution characteristic of a gas completely accommodated to the temperature of the surface.

The complete results of σ' for all conditions of this experiment are given in Fig. 50 which is a plot of σ' versus incoming beam velocity for argon gas on a W (100) surface at the given angles and surface conditions. The direct force measurement gave the combined value $(P_i + P_r)$ per particle. From the incoming velocity, P_i could be obtained. The value P_w was calculated assuming the reflected gas particles were completely accommodated to the surface which was at room temperature. Simple manipulation then gave σ'. The values for $(P_i + P_r)/_{\text{incoming atom}}$ used for these calculations, were values obtained from the smoothed curves of Fig's. 44 to 49.

The work of McGinn[30,31] for monoenergetic argon beams on non-ordered gold deposited surfaces was plotted in his report as a force ratio value in the direction of the beam, against the temperature of the source. The force ratio was determined by measuring the force due to the beam striking a target surface at some angle, and the force exerted by the same beam on a "virtual surface" having the property of complete thermal accommodation with diffuse reflection. The target temperature and cavity were maintained at 240° K by a projection lamp. For comparison purposes with the results of this thesis, the argon molecules in McGinn's experiment were assumed to reach a velocity (expansion to $M = \infty$) characteristic of the given source temperatures. For ease of comparison of results, the data chosen was the data taken at the angle of incidence $\theta_i = 0^{\circ}$. These results were then plotted on Fig. 51.

The results of this paper (argon on clean W (100)) at $\theta_i = 0^{\circ}$ were also plotted on Fig. 51. In order to obtain the force ratio, the value of $(P_i + P_r)$ measured by the torsion balance, was non-dimensionalized by the value of P_i obtained from the measured values of velocity, and of P_w calculated for a room temperature surface.

The results of Doughty and Schaetzle[29] for argon and nitrogen (N_2) on gas covered engineering grades of aluminum at $\theta_i = 0^{\circ}$ were included in the same figure. They plotted σ' using the relationship (for normal incidence) $\sigma' = 2 - \beta_{\text{normal}}/\beta_{\text{cavity}}$ against incoming energy of the beam. β was a measure of the fibre twist of their torsion balance. The force ratios $\beta_{\text{normal}}/\beta_{\text{cavity}}$ were then obtained by taking values for σ' from their plots and subtracting them

from 2. It can clearly be seen that there is a large difference in the force ratios measured on the different surfaces.

P_r/P_i against incoming molecular energy at $\theta_i = 0^o$ was plotted in Fig. 52, so that the results of this experiment could be compared with the reported results of Boring and Humphris[25,26] and Mair, Viney and Colligon[28]. Again, this experiment measured $(P_i + P_r)$. The value of P_i was obtained by using measured values of the incoming velocity and thus P_r could be obtained. The work of Boring and Humphris gave the force ratio P_r/P_i for charge-exchanged N_2 molecules on a mica or gold surface, both of which were gas covered, rough and uncharacterized. For a comparison, the work of Mair, Viney and Colligon for N_2^+ ions on a copper target used in the "as is" condition was also included. It can be seen very clearly that there is a large difference in the clean and dirty surfaces results, where for clean surfaces, the value of P_r approaches P_i especially at the higher energies.

Using the appropriate relationships and any required assumptions (where necessary) to reduce the data further, results of normal momentum accommodation coefficients versus incoming molecular energy for a number of authors were plotted in Fig. 53 for $\theta_i = 0^o$. As can be seen, the results for various gas-surface combinations where one suspects a surface which is either gas covered or rough (or both) are quite close. However, clean surface results (Ar - W (100)) are seen to show lower values of σ'. The same effect for σ' is shown in Fig. 54 for the angle $\theta_i = 30^o$.

4.5 Comparison with Theoretically Calculated Normal Momentum Accommodation Coefficients

The work of Jackson[120] yielded a coefficient α_n defined as $\alpha_n = 1 - P_r/P_i$. For a comparison, a value of P_r/P_i was taken from the theoretically derived value α_n for the case of Ar on tungsten, $\phi_i = 0^o$, $\theta_i = 30^o$ at an E_o^* greater than that for which trapping occurred. (i.e., $E_o^* > 6$). The values for P_r/P_i were approximately equal to 0.47 for $E_o^* = 9.5$, and increased slowly to 0.55 for $E_o^* \to \infty$. For the clean surface Ar - W(100) results at $\theta_i = 29^o$ where there did not appear to be any trapping, the experimental values were $0.78 \leq P_r/P_i \leq 0.91$. Thus, it seems that Jackson's results underestimated the value of P_r. This could be due to the fact that Jackson assumed no thermal motion of the target lattice atoms.

Oman[119] calculated values for a normal momentum coefficient, defined as

$$\bar{\sigma}_2 = 1 - \frac{\overline{v \cos\theta}}{v_i \cos\theta_i} \equiv 1 + \frac{|P_r|}{P_i}$$

This was done by a numerical experiment for the rare gases He, Ne, and Ar on an Ag single crystal surfaces. He considered the thermal motion of the surface, the effects of restraining forces in the lattice, used a Lennard-Jones 6-12 potential force law for the interaction and assumed that the surface atoms were independent oscillators. In the momentum coefficients quoted by Oman, the

portion of the molecules trapped have been excluded, so that the value of $\bar{\sigma}_z$ shown in Oman's report deals only with the particles that are not trapped. However, it is possible to look at the values where trapping ceases (i.e., at a high enough incoming energy). At an equivalent source temperature > 10,000°K, where trapping ceases, the value of the moment coefficient $\bar{\sigma}_z$ is $\bar{\sigma}_z = 1.375$ at $\theta_i = 40^\circ$. This means that $P_r/P_i \approx 0.375$. $\bar{\sigma}_z$ appears to slowly increase from the value 1.375 for higher energies. This again, compared to results at $\theta_i = 29^\circ$ for the Ar - W(100) system, seems to be quite low, although it is necessary to qualify this statement by recalling that the value of $\bar{\sigma}_z$ was obtained for momentum transfer for a silver surface. The comparison of the experimental value at $\theta_i = 29^\circ$, with the theoretical value at $\theta_i = 40^\circ$, is justified by noting that Jackson showed that P_r/P_i should increase as θ_i increases. P_r/P_i also increases for increasing incoming energy.

5. CONCLUSIONS

The experimental values for normal momentum transfer between incident argon or helium gas atoms, and the (100) face of a W single crystal, have been presented for a hydrogen covered surface, ("clean" conditions), a surface covered by an unspecified gas ("dirty" conditions), and a nitrogen covered surface for incident energies (for the argon gas) between 0.065 to 0.53 e.v.

The "clean" surface data were actually obtained with a monolayer of hydrogen covering the surface. It has been shown by other authors that rough surfaces or gas covered surfaces markedly affected helium reflection, such that the reflected beam flux variation approached a cosine distribution. Thus the helium atomic beam can be used as a probe of the surface state. The results obtained indicated that the "clean" surface was smooth on an atomic scale, with the interaction of the incident gas atoms occurring predominantly with the tungsten atoms.

There was a large difference in momentum transfer results between the "clean" and "dirty" surface. For $\theta_i = 0^\circ$ or 29° for the "clean" surface conditions, doubling the incoming gas velocity more than doubled the momentum transfer. As the momentum transfer results corresponded closely to theoretical specular reflection values, it could be postulated that there was a low energy transfer to the surface, and this transfer became lower for an increase in the incoming energy.

Under some conditions (lower incident velocities, $\theta_i = 41^\circ$) it was observed that the normal momentum transfer became characteristic of trapping of the gas particles, with subsequent re-emission from the surface. More investigation of this phenomenon at higher angles of attack might prove to be illuminating.

The momentum transfer results for a contaminated surface corresponded closely to completely diffuse reflection, fully accommodated to the temperature of the surface at the lower incident energies. As the incoming gas energy increased, the momentum transfer results suggested a decreasing accommodation.

If the "dirty" surface results of this thesis were extrapolated to higher incident velocities, it would appear that the momentum transfer results would give values similar to those found by other authors which were obtained

for various gas-surface combinations, having mass ratios varying from 0.203 (Ar/Au) to 1.48 (Ar/Al). The data included diatomic molecular results. It thus appears that the gas contaminating layer on the surface and possibly the surface roughness (in some cases) dominated the momentum transfer process.

As suggested earlier, part of the aim of this work was to obtain an understanding of the values of drag coefficients of satellites. The drag coefficient is of importance in several respects, for example, an uncertainty in the drag coefficient produces an equal uncertainty in the calculated atmospheric density derived from orbital perturbation. While satellites do not fly in helium and argon mixtures and are not composed of monocrystalline tungsten, nevertheless, the results suggest some interesting implications. Particularly, while there is little knowledge at present of the gas adsorption-desorption equilibrium of surfaces in orbit, these results suggest that a marked variation in aerodynamic force is possible between gas-free and gas covered surfaces, so that in future it may be possible to control momentum transfer within limits by proper selection of surface materials and geometry.

Finally, it is hoped that the results of this thesis will aid in the establishment of a sound theoretical basis for the interaction of particles with surfaces at higher-than-thermal energies, and serve as a step toward surface interaction studies involving the diatomic or dissociated atoms typically found in the earth's upper atmosphere.

REFERENCES

1. Su, C. L. Willis, D. R. — The Effectiveness of Two Dimensional Momentum Traps. University of California Report No. AS-66-8 (1966)

2. Smith, M. C. — Computer Study of Gas Molecule Reflections from Rough Surfaces. Proc. 6th Int. Rare. Gas Dyn. Conf. 1217 (1969)

3. Alcalay, J. A. Knuth, E. L. — Experimental Study of Scattering in Particle-Surface Collisions with Particle Energies of the Order of 1 e.v. Proc. 5th Int. Rare. Gas Dyn. Conf. 253 (1967)

4. Devienne, F. M. Roustan, J. C. Clapier, R. — Speed Distribution of Scattered Molecules after the Impact of a High Velocity Molecular Beam on a Solid Surface. Proc. 5th Int. Rare. Gas. Dyn. Conf. 269 (1967)

5. Devienne, F. M. Souquet, J. Roustan, J. C. — Study of the Scattering of High Energy Molecules by Various Surfaces. Proc. 4th Int. Rare. Gas Dyn. Conf. 584 (1966)

6. French, J. B. — Molecular Beams for Rarefied Gas Dynamics Research Advisory Group for Aerospace Research and Development. Agardograph 112 (1966) North Atlantic Treaty Organization.

7. French, J. B. Prince, R. H. — Testing of a Mass Spectrometer for Project Viking Martian Entry using Molecular Beam Simulation. Aerocol Report 70-7 (1970) for Martin Marietta Corporation.

8. Locke, J. W. — A Critical Evaluation of the Metastable Time-of-Flight Technique for Obtaining Molecular Velocity Distributions. Institute for Aerospace Studies, University of Toronto, UTIAS Report No. 143.

9. Prince, R.H. — The Interaction of Low Energy Atmospheric Ions with Controlled Surfaces. Inst. for Aerospace Studies, University of Toronto, UTIAS Report No.133.

10. Utterback, N. G. Miller, G. H. — Fast Molecular Nitrogen Beam. Review Sci. Instr. 32, 1101 (1961)

11. Massey, H. S. W. Burhop, E. H. S. — Electronic and Ionic Impact Phenomena. Oxford University Press (1952).

12. McDaniel, E. W. — Collision Phenomena in Ionized Gases. John Wiley and Sons (1964).

13. Gould, R. F. (editor) — Ion-Molecule Reactions in the Gas Phase. Advances in Chemistry Series 58, American Chemical Society Publications(1966).

14. Smith, D. P. — Scattering of Low-Energy Noble Gas Ions from Metal Surfaces. J. Appl.Phys. 38, 340 (1967).

15. Hayden, H. C. Utterback, N. G. — Ionization of Helium, Neon, and Nitrogen by Helium Atoms. Phys. Rev. 135, A 1575 (1964).

16. Haugsjaa, P. O. McIlwain, J. F. Amme, R. C. — Secondary Electron Emission by Argon Atoms and Ions from a Gas-Covered Surface. J. Chem. Phys. 48, 527, (1968).

17. Redhead, P. A. Hobson, J. P. Kornelsen, E. V. — The Physical Basis of Ultrahigh Vacuum.Chapman and Hall Ltd. (1968).

18. Kaminsky, M. — Atomic and Ionic Impact Phenomena on Metal Surfaces. Academic Press Inc. (1965)

19. Koedam, M. — Sputtering of a Polycrystalline Silver Surface Bombarded with Monoenergetic Argon Ions of Low Energy (40-240 e.v.) Physica 24 692 (1958).

20. Koedam, M. — Sputtering of Copper Single Crystals Bombarded with Monoenergetic Ions of Low Energy (50-350 e.v.) Physica 25 742 (1959).

21. Stuart, R. V. Wehner, G. K. — Sputtering Yields at Very Low Bombarding Ion Energies. J. Appl. Phys. 33, 2345 (1962)

22. Wehner, G. K. — Sputtering Yields for Normally Incident Hg^+ - Ion Bombardment at Low Ion Energy. Phy. Rev. 108, 35 (1957)

23. Stuart, R. V. Wehner, G. K. — Energy Distribution of Sputtered Cu Atoms. J. Appl. Phys. 35 1819 (1964).

24. Millikan, R. A. — Coefficients of Slip in Gases and the Law of Reflection of Molecules from the Surfaces of Solids and Liquids. Phys. Rev. 21 217 (1923)

25. Boring, J.W. Humphris, R. R. — Momentum Transfer to Solid Surfaces by N_2 Molecules in the Energy Range 7-200 e.v. Proc. 6th Int. Rare. Gas Dyn.Conf.1303(1969)

26. Boring, J. W. Humphris, R. R. — Drag Coefficients for Free Molecule Flow in the Velocity Range 7-37 Km/sec. AIAA Journal 1658 (1970)

27. Knechtel, E. D. Pitts, W. C. — Experimental Momentum Accommodation on Metal Surfaces of Ions Near and Above Earth-Satellite Speeds. Proc. 6th Int.Rare. Gas Dyn. Conf. 1257 (1969)

28. Mair, W. N. Viney, B. W. Colligon, J.S. — Experiments on the Accommodation of Normal Momentum Proc. 5th Int. Rare. Gas Dyn. Conf. 187 (1967)

29. Doughty, R. O.
Schaetzle, W. J.
Experimental Determination of Momentum Accommodation Coefficients at Velocities up to and Exceeding Earth Escape Velocity. Proc. 6th. Int. Rare. Gas Dyn. Conf. 1035 (1969).

30. McGinn, J. H.
Molecular Beam Apparatus for the Determination of Momentum Accommodation Coefficients for Neutral Particle Surface Interactions. Proc. 5th Int. Rare. Gas Dyn. Conf. 1455 (1967).

31. McGinn, J. H.
Molecular Beam Surface Interaction. Final Report for Contract NASw-1588. General Electric Space Sciences Laboratory.

32. Abuaf, N.
Marsden, D. G. H.
Momentum Accommodation of Argon in the 0.06 to 5 e.v. Range. Proc. 5th Int. Rare. Gas Dyn. Conf. 199 (1967)

33. Stickney, R. E.
An Experimental Investigation of Free Molecule Momentum Transfer Between Gases and Metallic Surfaces. University of California, Tech. Rept. HE-150-182.

34. Savage, H. F.
Bader, M.
Momentum Accommodation of N^+, N_2^+, and A^+ Incident on Copper and Aluminum from 0.5 to 4 K.E.V. NASA Tech. Note Nasa TN D-1976, (1963).

35. Bossell, U.
Investigation of Skimmer Interaction Influences on the Production of Aerodynamically Intensified Molecular Beams. University of California, Berkeley. Report No. As-68-6 (1968).

36. Govers, T. R.
LeRoy, R. L.
Deckers, J. M.
The Concurrent Effects of Skimmer Interactions and Background Scattering on the Intensity of a Supersonic Molecular Beam. Rarefied Gas Dynamics, 6th. Int. Conf. 985 (1969).

37. Vick, A. R.
Andrews, E. H. Jr.,
Dennard, J. S.
Craidon, C. B.
Comparisons of Experimental Free-Jet Boundaries with Theoretical Results Obtained with the Method of Characteristics. NASA TN D-2327 (1964)

38. Ashkenas, H.
Sherman, F. S.
The Structure and Utilization of Supersonic Free Jets in Low Density Wind Tunnels. Rarefied Gas Dynamics. 4th Int. Conf. 84 (1966).

39. Bier, K.
Hagena, O.
Influence of Shock Waves on the Generation of High-Intensity Molecular Beams by Nozzles. Rarefied Gas Dynamics. 3rd Int. Conf. 478 (1963).

40. Ishii, H.
Nakayama, K.
A Serious Error Caused by Mercury Vapour Stream in the Measurement with a McLeod Gauge in the Cold Trap System (Effect of the Diffusion of Nitrogen in the Mercury Vapour Stream). Trans. 8th National Vacuum Symposium. Vol. 1, 519 (1961)

41. Utterback, N. G.
Griffith, T. Jr.,
Reliable Submicron Pressure Readings with Capacitance Manometer. Rev. Sci. Inst. 37, 866 (1966).

42. Lafferty, J. M.
Davis, W. D.
Favreau, L. J.
Study of Hot-Cathode Magnetron Ion Gauge. NASA Contractor Report NASA CR 701 (1967). Prepared by General Electric Company.

43. Valleau, J. P.
Deckers, J. M.
Supersonic Molecular Beams II. Theory of the Formation of Supersonic Molecular Beams. Can. J. Chem. 43 6 (1965).

44. Anderson, J. B.
Fenn, J. B.
Velocity Distributions in Molecular Beams from Nozzle Sources. Phys. Fluids 8 780 (1965).

45. Fenn, J. B.
Anderson, J. B.
Background and Sampling Effects in Free Jet Studies by Molecular Beam Measurements. Rarefied Gas Dynamics. 4th Inst. Symposium 311 (1965).

46. Schugerl, K.
Investigations and Applications of Supersonic Molecular Beams. Rarefied Gas Dynamics 6th. Int. Symposium. 909 (1969).

47. LeRoy, R. L.
Govers, T. R.
Deckers, J. M.
Supersonic Molecular Beam Intensities. Can. J. Chem. 48, 927 (1970).

48. Milne, T. A.
Greene, F. T.
Mass Spectrometric Observations of Argon Clusters in Nozzle Beams. I. General Behaviour and Equilibrium Dimer Concentrations. J. Chem. Phys. 47 4095 (1967).

49. Bier, K.
Hagena, O.
Optimum Conditions for Generating Supersonic Molecular Beams. Rarefied Gas Dynamics 4th. Int. Symp. 260 (1966).

50. Hagena, O.
Comments to "Background Gas Scattering and Skimmer Interaction Studies Using a Cryogenically Pumped Molecular Beam Generator". R.G.D. 5th Int. Symp. 1425 (1967).

51. Obert, W.
Einfluss Der Gasart und des Stromungsbedingungen in der Duse auf die Eigneschaften Kondensierter Molekularstrahlen. Doctorate Thesis. Fakultat fur Maschinenbau der Universitat Karlsruhe, July (1970).

52. Wang, J. C. F.
Bauer, P. H.
Measurements of Spatial Distribution of Species in Helium Argon Gas Mixtures Expanding in Supersonic Jets. R.G.D. 6th Int. Symp. 1009 (1969).

53. Miller, D. R.
Andres, R. P.
Translational Relaxation in Low Density Supersonic Jets. R.G.D. 6th Int. Symp. 1385 (1969).

54. Abuaf, N.
Anderson, J. B.
Andres, R. P.
Fenn, J. B.
Miller, D. R.
Studies of Low Density Supersonic Jets. R.G.D. 5th Int. Symp. 1317 (1967).

55. Scott, J. E. Jr., Phipps, J. A. — Translational Freezing in Freely Expanding Jets. R.G.D. 5th Int. Symp. 1337 (1967).

56. Armstrong, D. E. Blais, N. — Large Rotary Vacuum Seal. Rev. Sci. Inst. 34, 440 (1963)

57. Findlay, P.A.R. — Private Communication. Sales Development Engineer Consolidated Mining and Smelting Co. of Canada.

58. Nottingham, W. B. — Design Parameters' Influence on M.I.T. Bayard-Alpert Gauge Sensitivity. Transactions of the 8th Vacuum Symposium, A.V.S. 494 (1961).

59. Dushman, S. — Scientific Foundation of Vacuum Technique, J. M Lafferty, editor, 4th printing, Second edition, pg. 334 (1966).

60. Owens, C. L. — Ionization Gauge Calibration System Using a Porous Plug and Orifice. J. Vac. Sci. and Tech. 2 104 (1965).

61. Davis, W. D. — Gauge Calibration in the Ultra-High Vacuum Range. Transactions of the 10th National Vacuum Symposium. A.V.S. 253 (1963).

62. Paul, M. C. — Mass Filter Studies of Gases in a 90 Litre Getter-Ion Vacuum System. Vacuum 15 239 (1965).

63. Rozgonyi, G. A. — Increase of Residual Background Gases During Ultra-High Vacuum Mass Spectroscopic Analysis. J. Vac. Sci. and Tech. 3 187 (1966).

64. Moskal, E. J. — The Design, Construction and Calibration of the UTIAS Optical Lever. Institute for Aerospace Studies, U. of T. M.A.Sc. Thesis (1965).

65. Jones, R. V, — Some Developments and Application of the Optical Lever. J. Sci. Instr. 38 37 (1961)

66. Jones, R. V. — Some Points in the Design of Optical Levers and Amplifiers. Proc. Phys. Soc. (London) B64 469 (1951).

67. Jones, R. V. Richards, J. C. — Recording Optical Lever. J. Sci. Instr. 36 90 (1959).

68. Pearson, S. Wadsworth, N. J. — The Development of a Microbalance to Detect a Force of 2 x 10^{-8} Dyne. Royal Aircraft Est. Tech. Note CPM 12 (1963).

69. — Metal Finishing Guidebook (1956 edition). Finishing Publications Inc. (Publisher).

70. Saxl, E. J. Allen, M. — Period of a Torsion Pendulum as Affected by Adding Weights. J. Appl. Phys., 40= 2499 (1969).

71. Freeman, R. D.
Gwinup, P. D.
Calibration of Torsion Wires and Spurious Forces in Torsion Knudsen Effusion Recoil Experiments. Rev. Sci. Instr. 37 773 (1966).

72.
Handbook of Chemistry and Physics, Chemical Rubber Publishing Co., Pg. 2691, 36th Edition 1954-55.

73. Buchbinder, G.G.R.
(Private Communication) Seismology Division, Earth Physics Branch, Ottawa, Ontario. Canada.

74. O'Keefe, D. R.
The Scattering of High Energy Argon Atoms from a Well Characterized (100) Tungsten Surface. Institute for Aerospace Studies, University of Toronto, UTIAS Report No. 132 (1968).

75. Estrup, P. J.
Anderson, J.
Danforth, W. E.
LEED Studies of Thorium Adsorption on Tungsten. Surface Sci. 4 286 (1966)

76. Estrup, P. J.
Anderson, J.
Chemisorption of Hydrogen on Tungsten (100). J. Chem. Phys. 45 2254 (1966).

77. Anderson, J.
Danforth, W. E.
Low Energy Electron Diffraction Study of the Adsorption of Oxygen on a (100) Tungsten Surface. J. Franklin Inst. 279 160 (1965).

78. Hagstrum, H. D.
D'Amico, C.
Production and Demonstration of Atomically Clean Metal Surfaces. J. Appl. Phys. 31 715 (1960).

79. Becker, J. A.
Becker, E. J.
Brandeis, R. G.
Reactions of Oxygen with Pure Tungsten and Tungsten Containing Carbon. J. Appl. Phys. 32 411 (1961)

80. Singleton, J. H.
Interaction of Oxygen with Hot Tungsten. J. Chem. Phys. 45 2819 (1966).

81. Hopkins, B. J.
Pender, K. R.
Comments on "The Adsorption of Hydrogen on (100) Tungsten Single Crystal Surfaces". by R. A. Armstrong. Surf. Sci. 6 479 (1967).

82. Chen, J.
Papageorgopoulos, C. A.
Ditungsten Carbide Overlayer on W (112). Surf. Sci. 20 195 (1970.)

83. Tamm, P. W.
Schmidt, L. D.
Interaction of H_2 with (100) W: I: Binding States J. Chem. Phys. 51 5352 (1969).

84. Wei, P. S. P.
Low Energy Electron Diffraction Study of Tungsten (100) Surface, J. Chem. Phys. 53 2939 (1970).

85. Blakely, J. M.
Kim, J. S.
Potter, H. C.
Segregation of Carbon to the (100) Surface of Nickel. J. Appl. Phys. 41 2693 (1970).

86. Miller, D. J.
Haneman, D.
Evidence for Carbon Contamination on Vacuum Heated Surfaces by Electron Paramagnetic Resonance. Surface Sci. 19 45 (1970).

87. Muller, E. W. — Hydrogen Promotion of Field Ionization and Rearrangement of Surface Charge. Surface Sci. 7 462 (1967).

88. Tamm, P. W. Schmidt, L. D. — Interaction of H_2 with (100) W: II: Condensation J. Chem. Phys. 52 1150 (1970).

89. Redhead, P. A. — Chemisorption on Metals under Ultra-High Vacuum Conditions. Symposium on Electron and Vacuum Physics, Balatonfoldvar, Hungary. (1962).

90. Karasek, F. W. — Relativity of Mass Spectra. Research/Development November, 55 (1970).

91. Hopkins, B. J. Pender, K. R. — The Adsorption of Hydrogen on (100), (110), (111) and (113) Orientated Tungsten Single Crystal Surfaces. Surface Sci. 5 316 (1966).

92. Collins, R. A. Blott, B. H. — Hydrogen Adsorption of the (110), (112), (100) and (111) Tungsten Single-Crystal Faces. J. Appl. Phys. 40 5390 (1969).

93. Abey, A. E. — The Change in Work Function of the (100) Surface of Tungsten as O_2, N_2, CO_2 and H_2 are Adsorbed. J. Appl. Phys. 40 284 (1969).

94. Armstrong, R. A. — The Reflection of Slow Electrons by Hydrogen-Covered Single Crystals of Tungsten. Can. J. Phys. 44 1753 (1966).

95. Estrup, P. J. Anderson, J. — LEED Studies of the Adsorption Systems W (100) + N_2 and W(100) + N_2 + CO. J. Chem. Phys. 46 567 (1967).

96. Van Oostrom, A. — Adsorption of Nitrogen on Single-Crystal Faces of Tungsten. J. Chem. Phys. 47 761 (1967)

97. Delchar, T. A. Ehrlich, G. — Chemisorption on Single-Crystal Planes: Nitrogen on Tungsten. J. Chem. Phys. 42 2686 (1965).

98. Anderson, J. Estrup, P. J. — Adsorption of CO on a Tungsten (100) Surface. J. Chem. Phys. 46 563 (1967).

99. Armstrong, R. A. — The Surface Potential of Carbon Monoxide Adsorbed on a Tungsten (211) Crystal. Proc. 25th Phys. Electronics Conf. M.I.T. Cambridge, Mass. 209 (1965).

100. Hopkins, B. J. Pender, K. R. — The Adsorption of Oxygen on the Surface of (110) and (100) Oriented Tungsten Single Crystals. Surface Sci. 5 155 (1966).

101. Bell, A. E. Swanson, L. W. Crouser, L. C. — A Field Emission Study of Oxygen Adsorption on the (110), (211), (111) and (100) Planes of Tungsten. Surface Sci. 10 254 (1968).

102. Engel, T.
Gomer, R.
Adsorption of Oxygen on Tungsten: Field Emission from Single Planes. J. Chem. Phys. 52 1832 (1970).

103. Estrup, P. J.
Anderson, J.
Adsorption and Decomposition of Ammonia on a Single-Crystal Tungsten (100) Surface. J. Chem. Phys. 49 523 (1968).

104. Waclawski, B. J.
Hughey, L. E.
Adsorption of Water Vapour on Polycrystalline Tungsten. Surface Sci. 19 464 (1970).

105. Engel, T.
Gomer, R.
Adsorption of Inert Gases on Tungsten: Measurements on Single Crystal Planes. J. Chem. Phys. 52 5572 (1970)

106. Muller, E. W.
McLane, S. B.
Panitz, J. A.
Field Adsorption and Desorption of Helium and Neon. Surface Sci. 17 430 (1969).

107. Rigby, L. J.
The Adsorption and Replacement of Hydrogen on Polycrystalline Tungsten. Can. J. Phys. 43 1020 (1965)

108. Rigby, L. J.
The Interactions of Nitrogen and Carbon Monoxide on Polycrystalline Tungsten. Can. J. Phys. 42 1256 (1964)

109. Singleton, J. H.
Simultaneous Adsorption of Hydrogen and Nitrogen on Tungsten at 300°K. J. Vac. Sci. and Tech. 5 109 (1968).

110. Yamamoto, S.
Stickney, R. E.
Molecular Beam Study of the Scattering of Rare Gases from the (100) Face of a Tungsten Crystal. J. Chem. Phys. 53 1594 (1970).

111. Jakus, K.
Hurlbut, F. C.
Gas-Surface Scattering Studies Using Nozzle Beams and Time-of-Flight Techniques. R.G.D. 6th Int. Conf. 1171 (1969).

112. McGinn, J. H.
Molecular Beam Surface Interaction. Quarterly Progress Report. April-July, 1969. Space Sciences Laboratory. General Electric Co.

113. Raff, L. M.
Lorenzen, J.
McCoy, B. C.
Theoretical Investigations of Gas-Solid Interaction Phenomena. I. J. Chem. Phys. 46 4265, (1967).

114. Lorenzen, J.
Raff, L. M.
Theoretical Investigations of Gas-Solid Interaction Phenomena II. Three-Dimensional Treatment. J. Chem. Phys. 49 1165 (1968).

115. Logan, R. M.
Keck, J. C.
Stickney, R. E.
Simple Classical Model for the Scattering of Gas Atoms from a Solid Surface: Additional Analyses and Comparisons. R.G.D. Proc. 5th Int. Conf. 49 (1967).

116. Moran, J. P.
Wachman, H. Y.
Trilling, L.
Scattering of Monoenergetic Argon Beams From Heated Platinum: Planar Time-of-Flight Measurements Phys. of Fluids. 12 987 (1969).

117. Smith, J. N. Jr.,
Atom Interactions with Solid Surfaces. FOM-Institute for Atomic and Molecular Physics, Amsterdam (1970).

118. Goodman, F. O.
On the Theory of Accommodation Coefficients. V. Classical Theory of Thermal Accommodation and Trapping. R.G.D. Proc. 4th Int. Conf. 366 (1966).

119. Oman, R. A.
Research on Gas-Surface Interactions 1966-67. Part II. Numerical Experiments on Scattering of Noble Gases from Single Crystal Silver. Grumman Research Report RE-306 (1967).

120. Jackson, D. P.
A Theory of Gas-Surface Interactions at Satellite Velocities. Institute for Aerospace Studies. U. of T. Report No. 134 (1968).

121. Lorenzen, J.
Raff, L.M.
A Quantitative Comparison of Gas-Surface Theory with Molecular Beam Data. J. Chem. Phys. 54 674 (1971).

122. Jackson, D. P.
French, J. B.
High Energy Scattering of Inert Gases from Well-Characterized Surfaces-II Theoretical. R.G.D. Proc. 6th Int. Conf. 1119 (1969).

123. Oman, R. A.
Bogan, A.
Li, C. H.
Theoretical Prediction of Momentum and Energy Accommodation for Hypervelocity Gas Particles on an Ideal Crystal Surface. R.G.D. Proc. 4th. Int. Conf. 396 (1966).

124. Smith, J. N. Jr.,
Saltsburg, H.
Palmer, R. L.
The Scattering of He, Ne, Ar, and Xe from the (111) Plane of Ni; Comparison with Ag(111) and Au (111) R.G.D. Proc. 6th Int. Conf. 1141 (1969).

125. Fisher, S. S.
Pjura, G. A. Jr.,
Intensity and Velocity Distributions of 300°K He and Ar Aerodynamic Beams Scattered from a Vapour-Deposited Ag(111) Surface. R.G.D. Proc. 7th. Int. Conf. 1971 (to be published)

APPENDIX A: BEAM GENERATING SYSTEMS

SUPERSONIC BEAM SYSTEMS

The generation and use of supersonic expansions as beam generators has been discussed by several authors. A review of beam generating systems may be found in the AGARDograph by French[6]. Basically, the supersonic beam generating system components are shown in Fig. 1. The source, which can be heated, contains a gas at a high pressure, from several torr to several atmospheres. The gas achieves highly ordered motion by expansion into a volume having a pressure on the order of 10^{-3} to 10^{-4} torr. A virtually undisturbed beam of gas molecules is extracted from the core of the expansion by a skimmer, and this beam passes into a region at a pressure on the order of 10^{-6} to 10^{-7} torr. Background gas effects are minimized atthis pressure level. A final collimator can then be used to further define a beam, which can be used for an experiment in another chamber having an even lower pressure.

There are several advantages for this type of beam. It can have a larger beam intensity than beams formed by effusive sources or ion sources. The gas molecules have a very narrow velocity spread (almost monoenergetic). The value of the flux over the beam diameter is virtually constant, even over a beam diameter of one inch[7]. The gas molecules are not dissociated, electronically excited or ionized, but may be vibrationally excited. Due to the fact that the gas molecules expand radially (intensity α $1/r^2$), that the beam paths are long, and the defining orifices small, the divergence of the beam is usually small after it has passed the last collimator.

To obtain higher energies for the heavier particles, it is necessary to use a seeded beam technique, where a low mole fraction of a heavy gas is mixed with a light gas, and the mixture is expanded. A velocity analysis of the resultant beams should be obtained. The velocity calculated from the measured temperature (assuming complete conversion of heat to directed energy) is not always equivalent to the actual velocities. First of all, difficulty has been found by some experimenters in relating measured oven temperatures to the actual gas temperatures. Secondly, at low source pressures, the gas does not expand to a high Mach No. equal to ∞. This possible source of error can be reduced by the use of empirical formulae. However, it would be difficult to apply the above correction to seeded beams. Under certain operating conditions, it has been noted that for seeded beam systems, there can be a velocity slip between the heavy and light gas species. This seeding technique to obtain high velocities is limited, as for example, it is found that for a 1% N_2, 99% H_2 mixture, velocities with normal tungsten tube, resistance heated sources, are approximately 8.7 Km/sec[7]. Greater velocities could be achieved with R. F. heated sources for example, but beam particle characterization would become difficult. Another problem concerns the effect of two gases in the beam. There is a concentration of the heavy gas species on the centre line (and thus in the beam), but it is still necessary to consider whether the light gas component in the beam would be a problem.

ION BEAM SYSTEMS

It is possible to obtain both ion and neutral beams of molecules or atoms by use of an ion beam generation system. These beams are useful in the range of energies starting at approximately 10 e.v., the lower value of energy being determined by the fact that space change effects limit beam density to levels where experimental results are difficult to obtain.

It is noted that the following discussion deals with problems that are found only under specific apparatus conditions, and many of these difficulties can be removed or reduced to acceptable levels by good design and construction. Some problems mentioned, however, are applicable to all ion beam systems.

PURITY OF THE BEAM

If the path between the target area and the ion source is a line-of-sight path, then the beam of particles striking the target can contain many different types of particles. First of all, the neutrals (of the gas one wishes to ionize) can form an effusive Maxwellian beam from the relatively high pressure area in the source, and have a fairly high flux. Secondly, metastable atoms or molecules can be formed and bombard the target (Ref. 8 contains a compilation of various metastable states of common gases). Thirdly, vacuum chamber background gases in the ionization region can be ionized and accelerated to the target[9]. Doubly ionized species are normally not likely to cause problems due to the greater energy necessary for ionization of the second electron. However, singly charged, dissociated particles can definitely be a problem. Prince[9] mentions that the N^+ ion densities are only a few % of the number of N_2^+ ions for 30 e.v. ionizing electrons. Utterback and Miller[10] analyzed the nitrogen beam formed by a similar apparatus, and found that 99% of the ions were N_2^+ with only a trace of N^+ for ionizing electrons below the threshold for formation of N^+ ions. They found that it was possible to obtain an appreciable amount of N^+ by "increasing the energy of the impacting electrons above the 24 e.v. threshold for N^+ production". To obtain a pure ion beam, some experimenters have used a mass spectrometer[9] where only particles with a specific e/m value could be focussed on a final collimator.

BEAM ENERGY

(a) Ion Beams:

Utterback and Miller[10] used a stopping potential method to obtain average particle energies and energy spreads. For an ion source-to-neutralization region potential difference of 35 volts, the average energy of the particles was one volt less. Prince[9] discussed the possible effects which would given an average energy deviation and contribute to the energy spread. The deviations in energy could be caused by thermal effects in the source gas, space charge effects in the source (either by ionizing electrons or the ions formed), and by the fringing fields due to the applied extraction voltage. He found an energy defect of 0.75 e.v.. Prince took great care to minimize the energy broadening effects. For an experimental energy distribution, he found a width at half maximum of 0.4 e.v., with 50% of all ions within an 0.5 e.v. range, and 90% within a 2 e.v. range of the mean energy. The distribution was independent of the particular nominal energy. An energy spread of 0.5 e.v. at half-maximum for an average N_2^+ energy of 34 e.v. was reported by Utterback and Miller[10].

One must be careful in specifying the incident ion energy for an ion on a metallic target. Due to the image potential induced in the metal target, the ion can be accelerated into the target, giving an additional energy to the particle on the order of 2 e.v. For low nominal incoming energies of ions, this value could introduce a large percentage error in the reported mean velocity.

(b) Neutral Beam by Charge Exchange with Parent Neutral Gas:

The charge transfer for the majority of ions with the parent neutral gas involves little momentum transfer[11,12,13] and experimenters assume that the resulting neutral beam energy is the same as the ion beam energy, and the direction is unchanged. Also, it is noted that the weak impulse due to the electron transfer is approximately perpendicular to the direction of the primary beam [12].

Considering then conservation of momentum, the direction and momentum of most ions after becoming neutrals, are virtually unchanged. However, there is still a measurable number of collisions that produce large deflections where the incoming ions pass close to the target particle. These of course, can be removed simply by placing a collimating orifice beyond the neutral gas cell. Thus, the neutral gas velocity distribution should be obtainable by investigation of the ion velocity distribution. However, Utterback and Miller [10] bring up an interesting point to consider for neutral beams. Suppose a final collimating grid is used to decelerate or accelerate the ions. The last focussing lens located upstream of the above grid, sends the ions through the final collimating grid, through the gas cell to the target (with no more deviations). After this final focussing operation, the N_2^+ molecules (for example) can go through a charge exchange with the background gas in the vacuum chamber, or with neutral gas effusing in a Maxwellian beam from the charge exchange cell. These fast neutral molecules are not retarded by last grid, nor are they deflected by the potential which deflects ions which have passed through the charge exchange area. For a line-of-sight system, ions which are on or close to the axis, can experience a resonant charge exchange process at any point in the system, including the gas cloud formed by the effusion from the ionizing area, and strike the target with a high energy. Thus especially for the requirement of incident particles on a target for low energies, it is possible to have a small class of molecules with a high energy, and the remaining portion of the molecules with a lower energy. Then for a given experimental system the problem reduces to the relative energies, and the relative amounts of particles one expects from the charge exchange process in both areas, as the cross-section for resonant charge exchange is lower for higher velocities. The lower pressure area (longer length) is on order of 10^{-6} to 10^{-5} torr, whereas the charge exchange gas cell can have pressures in the range of 10^{-4}torr [9,10]. The charge transfer cross-section does peak at lower energies[10,12] but does not fall too drastically as the ion beam energy increases to larger values.

ION BEAM INTENSITIES

Some experimenters use the current collected at a target upon which the ion beam is incident, to measure the flux to the target. This can be in error. It is necessary to consider the possibility of ions reflected as ions, ions sputtering positively charged particles, and secondary electron emission. Smith[14] has investigated the flux distribution for both the scattered primary ions and the sputtered target ions for the system of He+, Ne+ and Ar+ ions in the energy range 0.5 to 3.0 K.e.V., on polycrystalline Mo and Ni. Typical maximum counting rates for the reflected distribution on the order of 10^3 ions/sec. were found, for incident flux rates on the order of 10^{13} particles/cm^2 sec.. Thus it is possible (for total momentum experiments) to neglect this effect.

However, secondary electron yields can be of a sufficiently high value to be a problem. Utterback and Miller looked at $\gamma+$ and γ^o for N_2^+

molecules on a gold surface, gas covered from background contamination. γ^+ is defined as the secondary electron yield per incident ion, and γ^o pertains to the yield per incident electrically neutral particle. For energies $\leq$ 100 e.v., γ^+ was < 1%. For energies on the order of 200 e.v., γ^+ was approximately 10%. They also showed that for these measurements, $\gamma^o \approx \gamma^+$ to within 20%. Hayden and Utterback[15] investigated helium on a contaminated gold surface for energies from 30 e.v. to 1000 e.v., γ^+ for He+ started at approximately 0.2 at 30 e.v. and increased to ~ 1 at 1000 e.v.. γ^o for He was $\approx$ 0.01 at 50 e.v., $\gamma^o \approx$ 0.06 at 100 e.v. and was approximately 0.2 at 200 e.v. and followed the values for γ^+ fairly closely from there to higher energies. Prince[9] found the electron yield γ^+ for N_2^+ ions on a clean and H_2 covered W (100) surface. γ^+ was ~ .04 to .05 for clean surfaces for N_2^+ energies of 15 to 30 e.v., and was ~.02 to .03 for H_2 covered surfaces for the same range of 15 to 30 e.v. γ^+ for N_2^+ on contaminated Mo varied from 0.14 to 0.009 for the range 19 - 30 e.v. In general, the peak in the kinetic energy distributions of the secondary electrons were found to be in the 1-2 e.v. range. Haugsjaa et al[16] gave the results for γ^o and γ^+ for an argon beam on a gold foil surface in a vacuum of 10^{-6} torr. γ of ~ 0.1 was not reached until approximately 300 e.v. for incoming argon atoms. Depending on the experimental conditions, the reported values for γ either remain constant as incoming ion energy increases, or increases with incoming ion energy.

In conclusion, the phenomenon of secondary electron emission occurs for incident ions on a metallic surface. A means of obtaining the incident flux of ions on a metal surface is to measure the current to this surface. If this current is not corrected for secondary electron emission, then the deduced ion flux is high. A significant error can thus be made in calculating the net momentum transfer per ion.

APPENDIX B: ON SPUTTERING AND PENETRATION

Physical sputtering (as opposed to chemical sputtering where a product is formed by gas-surface atoms), is defined as the ejection of atoms from a solid when its surface is bombarded by high energy particles (atoms or ions). In measuring momentum transfer from a gas to a surface, sputtering can influence the results. One must consider the amount (and the mass) of the sputtered atoms, the velocity, and the angular distribution of the sputtered atoms. From Ref's. 17 and 18, it is possible to see that the sputtering ratio (sputtered atoms per incident ion) can be appreciable at 50 e.v. of incident ion energy, and the ratio can be approximately 1, even in the energy range 150 - 200 e.v.. For example, on a silver target, 200 e.v. Ar^+ ions give a sputtering yield of approximately 1.2 atoms/ion and 50 e.v. Ar^+ ions give a yield of approximately 0.15 atoms/ion [19,20]. For a tungsten target, 200 e.v. Ar^+ ions give a yield of approximately 0.4 atoms/ion, and the yield falls off to a negligible value at 50 e.v.[21]. In terms of yields, Wehner[22] investigated the system of 30 - 400 e.v. Hg^+ ions bombarding 26 different metals. He found the highest yields of sputtered atoms per incident ion were for the metals Cu, Ag, and Au, targets which are commonly used for momentum transfer and surface studies. Total yields can increase as the incident beam goes from normal incidence to some angle of attack. From single crystal targets, it has been found that sputtered atoms are preferentially ejected along close packed directions of the crystal. At the lower energies for normal incidence beams, the sputtered atom are scattered in a "below -cosine" distribution; that is, relative to a cosine distribution more particles are scattered nearer the surface plane. This is due to the fact that directions requiring minimum momentum change lie near the surface. At higher energies, directions nearer the surface normal predominate, and the distribution becomes "above cosine". However these incident energies where the distribution is "above cosine", are well above those that this thesis is concerned with.

As an example of the energy of the sputtered atoms, Stuart and Wehner[23] have examined the system of Kr^+ ions normally incident on a copper surface. The ions, having an energy range of 100 e.v. to 1000 e.v., sputtered Cu atoms with an average ejection energy in the range of 2 to 14 e.v..

The above results can be changed by contamination effects. Redhead et al[17] discuss the effect of a contamination layer on the yield of sputtered atoms.

They conclude that the sputtering yield for a surface covered with an adsorbed gas would be of the same numerical magnitude as the clean surface sputtering yield.

The effects on a surface of energetic ions bombarding the surface are reported in Ref. 18. The surface can be severely etched, resulting in a rough surface which could cause difficulties in correlating experimental momentum transfer results to theoretical expressions.

The process of entrapment or penetration into the lattice of the solid is not a great consideration in momentum transfer results for the lower energies about which this thesis is concerned. Even for 100 e.v. Ar^+ ions on a tungsten surface, the fraction of ions entrapped and desorbed by heating to 2400°K is a very small percentage of the number of incident ions[17]. Thus, the phenomenon of entrapment (by penetration) was expected to have a negligible effect on the momentum transfer results reported in this thesis.

APPENDIX C: POSSIBLE CAUSES OF BEAM FLUX VARIATION

There are a number of mechanisms which could be used to explain the flux variations. First, as Govers, LeRoy and Deckers pointed out[36], the discharge coefficient could change as the source temperature increased.

Another point concerns the fact that as the source temperature increased, λ_{source} increased. Thus, using the formula derived by Anderson and Fenn,[44] where

$$M_f = 1.17 \left(\frac{\lambda}{d^*} \right)^{-0.4} \tag{6}$$

the freezing Mach number M_f decreased. Thus the beam gas had a higher transverse temperature (and velocity). The beam flux should decrease due to this effect for both gases.

As the x/d_* value was relatively large, it was necessary to investigate background penetration of the free jet. An indication as to the importance of this effect could be obtained from the work of Fenn and Anderson[45]. The distance downstream (L/d_*) for which background penetration exists, is given by:

$$\text{Log}_{10} \left(\frac{L}{d_*} + \frac{33}{Kn_o(P_o/P_1)} \right) = 1.07 \log_{10} \left[\frac{10^3 \, Kn_o}{\gamma} \right]^{2\left(\frac{\gamma-1}{\gamma}\right)} + 1.26 \tag{7}$$

For the case of argon at P_o = 160 torr, L/d_* was calculated to be 99.4 nozzle diameters. From the previous discussion on the free jet shape, this value of L/d_* would be expected to be greater for the particular nozzle used for this experiment. If there is appreciable background penetration, then one would expect only Ar - Ar and He - He collisions for the pure gas cases. With the long beam paths involved and the number of small diameter collimating orifices, one would expect that any "beam" molecules undergoing a strong collision with background molecules would be automatically deflected out of the beam and not be observed by the target, mass spectrometer, or velocity analyzer. The pressure levels (P_1) in the first chamber were typically on the order of 2×10^{-4} torr. Schugerl[46] investigated background effects and found that the background gas in the expansion chamber could be neglected only if $P_1 < 5 \times 10^{-5}$ torr. However, Govers, LeRoy and Deckers[36] have shown that intensity changes were small for variations in background pressures in the 10^{-4} torr region, and the intensity degradation was low as x/d_* increased. It was also experimentally shown during test runs on the beam for this work, that as the x/d_* was increased from 122 to 149, the intensity dropped by an insignificant amount. Thus, it was assumed that background effects were unimportant.

Another point considered was the effect of source heating on the flux variation. As the velocity of beam atoms increased the collision cross-section for the interaction between the beam atoms and the background atoms decreased (with higher velocities). Thus, the flux should have increased for both gases due to this effect.

For the mixed beam case, two other factors may enter into the problem. The position of the source tube was adjusted (with respect to the skimmer orifice) for a beam maximum; that is, when operating under mixed gas conditions, the position of the source tube was adjusted for a maximum argon signal reading (maximum flux), as measured by a mass spectrometer mounted on the beam stagnation chamber. It was found that a small movement of the orifice perpendicular to the beam direction, would cause a large variation in the argon beam signal. Upon heating of the source tube, some misalignment (shift of the mechanical components) may occur. As the components had been aligned for maximum beam signal, any shift would cause the argon beam signal to decrease. However, it increased, and so the above effect can be discounted. One must also consider the fact that at higher velocities (source temperatures), there may be a greater slippage of He to Ar. Thus the argon velocity would not increase as rapidly as the helium velocity.

Both the flux from the expansion chamber and the collimation chamber must be considered, where the combination of the background gas at P_1 or P_2 and the skimmer or the collimating orifice form effusive molecular sources. First of all, these molecules would not contribute to the intensity variation, as the background pressure levels remain constant. Secondly, it is necessary to look at the overall contribution of these sources and compare them to the total number flux measured, to see if any corrections are necessary. From Ref. 6,

$$N_C = \frac{n_o c_{m_o} A_s A_c}{2\pi^{3/2} L^2} \qquad (8)$$

where N_C is the number of molecules hitting an area of A_c coming from an area A_s. A_{c_1} was taken as the area of the final collimating orifice for the molecules from chamber No.1, and A_{c_2} as the area of the target for the case of molecules from chamber No.2. $N_{c_1} \approx 5 \times 10^6$ molec/sec from the first chamber, and from chamber No.2 (collimation chamber), $N_{c_2} \approx 1.5 \times 10^7$ molecules/sec. These values are much less than the number entering the stagnation chamber due to the molecular beam (on the order of 10^{12} molecules/sec). Thus, it is possible to neglect the "beams" formed by these background molecules.

LeRoy, Govers, and Deckers[47], using a nozzle expansion, a constant mass flow, and a beam derived from a free jet expansion, investigated the flux variation of an argon beam for various source temperatures. To account for beam degradation, they postulated the mechanism of self-scattering of beam atoms between the "quitting surface" and the skimmer. The results were extrapolated to a background pressure = 0. Their results gave 1.30×10^{18} molecules/ster-sec. at 295° K, and 2.50×10^{18} molecules/ster-sec. at 780°K. This was approximately a 100% increase in argon flux over almost the same temperature range where the argon flux in Fig. 9 increased by 60%.

It is necessary to observe the conditions under which condensation occurs, and to discuss the effects of condensation on the beam. Clusters of molecules could increase the scattering cross-section for beam-beam collisions. Also, it would be necessary to consider the amount of energy of condensation carried off by a third body, and whether conservation of momentum would cause the third body and the dimer to obtain enough radial velocity to

be deflected out of the beam and not go through the collimating orifices.

Milne and Greene[48] investigated nucleation phenomena of argon nozzle beams by mass spectrometer methods. The nozzle was formed by putting a hole in a very thin plate. Other than the nozzle, the experimental conditions were similar to the experimental conditions of this thesis. For an argon beam at 300°K, $d_* = 0.004"$, $P_o = 2$ psig ≈ 860 torr, Milne and Greene found that the mole fraction of Ar_2 was approximately 0.001. At the lower pressures, the increase in Ar_2 was not a sensitive function of d_* and P_o; that is, extrapolating the results to $d_* = 0.0058"$, for $P_o = 2$ psig, the mole fraction of Ar_2 would be approximately 0.0015, and for $P_o = 2$ atmospheres, the mole fraction of Ar_2 would be about 0.0037. In terms of the flux measurement for this experiment, the cluster should be broken up on impact in the stagnation chamber, and the correct number flux on the target measured. Milne and Greene also mention that in no case did the velocity of the cluster lag that of the argon by more than 10%.

Bier and Hagena[49] investigated condensation effects in a free jet expansion for various gases, using beam parameters similar to those of this experiment. They obtained beam intensities and beam speed ratios as a function of stagnation pressure for Ar, He, and N_2, at a constant source temperature. An upper limit on P_o, d_* of 85 torr - mm for argon was suggested to avoid condensation effects. The P_o d_* for the room temperature argon runs for this experiment was 24 torr - mm., and thus it was initially believed that there was no condensation. However, Hagena[50] mentioned that characteristic conditions for the onset of condensation could be seen when the maximum beam intensity did not increase by increasing P_o. From Fig. 11, according to the definition of Hagena, it seemed that condensation effects appeared at a lower P_o d_* for a converging-diverging nozzle.

Obert[51] investigated condensation effects for various gases in converging, and converging-diverging nozzles. For a constant value of $(N/z)^+ = 500$, where N/z represents the number of molecules in the cluster, divided by the charge on the cluster, it was found that these clusters were formed at significantly lower stagnation pressures for a conical convergent-divergent nozzle, as compared to a convergent nozzle, for the same stagnation temperatures. It was also observed (for a constant diameter orifice) that the cluster size went down rapidly as the stagnation temperature was increased.

Bier and Hagena also looked for condensation effects in helium. Up to the values of P_o $d_* = 10^3$ (the limit of their experimental apparatus), they could find no condensation in helium.

In summary, after applying Hagena's definition of condensation to Fig. 11, it is believed that condensation of argon occurred for a P_o d_* of 24 torr - mm for the nozzle used in this experiment. The increase in argon flux as the source temperature T_o was increased, can be explained by this condensation phenomenon. As mentioned above, it is very difficult to condense helium. Thus, any variations in the pure helium beam flux as the temperature T_o increased, would be due to effects other than condensation. As can be seen from Fig. 10, the flux dropped by 7%. If no condensation were present, the argon flux should vary in a similar manner. However, the argon flux increased

by a large amount (61%) as the stagnation temperature was increased. On considering the formation of dimers, a three body collision must occur, where two of the atoms form the dimer, and the third atom takes away the heat of condensation. From conservation of momentum considerations, the particles would fly apart, in effect, widening the beam. Due to the narrow acceptance angle formed by the collimators, the majority of these collision partners would not be present in the beam which finally strikes the tungsten target. As the entire gas discharge was confined in a nozzle during a significant portion of the expansion, then one would expect the gas number density to be high, and the probability of three body collisions to be higher than that for a free jet expansion. The measured value of T_{11} for the beam molecules was lower (for $T_o = 298^o$ K) than the values found by other authors. This low temperature would also promote condensation at low values of $P_o d_*$. As shown by Obert, condensation effects decrease as the source temperature is increased. As will be shown from the beam velocity results in the Section 3.3, T_{11} for the expanded beam atoms was higher for higher stagnation temperatures. Thus, the atoms would be "hotter", and would not be so readily condensed.

APPENDIX D: UHV ROTATABLE SEAL

To minimize problems of positioning, focusing, and calibration of the optical lever, it is preferable to have the torsion balance and the optical lever move as a unit. Because of outgassing and the necessity of frequent optical adjustments, it was not possible to put the optical lever into the ultra-high vacuum volume. As one of the experimental parameters to be varied was the angle of attack of the target, it was necessary to rotate the torsion balance, and the optical lever with it. For these reasons, the design and construction of a large ultra-high vacuum rotating seal was initiated.

Detailed drawings of the construction are given in Fig's. 14 and 15, and photographs of the actual mechanism are shown in Fig's. 16 and 17. The description of the seal will start from the outer perimeter. The dimensional tolerance (both axially and radially) between the upper rotator and the lower stator, was maintained by ball bearings in a v-groove ball race, which was cut in the upper and lower plates. A medium vacuum was maintained against atmosphere by a rubber loaded teflon u-ring[56], with the rubber O-ring portion facing atmospheric pressure. A design value of 10% compression was used for the sealing ring. Teflon was used because of the low coefficient of friction, and thus a lubricant was not necessary. The rubber O-ring maintained a compressive force on the teflon, taking up any permanent set which could appear. Under high temperatures, the teflon and rubber were cooled by the three water channels shown in the figures. An inner, UHV seal is formed by an indium sealing process, where the indium must be melted before rotation of the top can be accomplished. The medium vacuum chamber was pumped by a small mechanical pump, and reached the base pressure of the pump (approximately 0.4 microns). This volume was pumped down to reduce the pressure differential across the indium (when molten) to a low value so that there was a negligible difference in the heights of the molten indium across the seal. Also, if there were any leak through the indium seal when the metal had solidified, then the leak rate would be very small if the pressure ratio across the leak in the seal was also small. The ultra-high vacuum seal was made by a thin metal ring which extended down into the indium in the indium reservoir, and the metal ring was placed close to the UHV side so that only a small area of indium was exposed to the UHV chamber, reducing the amount evaporated. A linear heater was bent into a coil around the indium reservoir to melt the indium when required. In case of a blow-out, the molten indium would be caught in an overflow reservoir instead of proceeding into the UHV main chamber where it would do much harm. The torturous path was provided so that any indium which evaporated would tend to plate out on the walls, and prevent the vapour from reaching the main chamber.

Indium was chosen as the UHV sealant material for a number of reasons. The actual material supplied was a mixture of 90% indium, 10% silver (standard grade) from Consolidated Mining and Smelting Co. The foremost consideration was its low vapour pressure which was less than that of pure indium[57] which must be heated to approximately 640°K before its vapour pressure would reach 10^{-11} torr. Another consideration was its low melting point. The alloy began to smelt at 141°C. The freezing point of the alloy was 235°C. The alloy would "wet" stainless steel type 304, but some difficulty was experienced before satisfactory wetting (or adhesion) of the indium alloy to the stainless steel was accomplished.

The rotor had a half-turret mounted on it. The top conflat flange was used as a mounting platform for the complete torsion balance and its supporting network, and was mated to the upper conflat flange on the turret. The centre

line of rotation of the rotor was 1/4" back fron the front wall of the turret. The torsion balance fibre was placed in this plane 1/4" back from the turret wall. Directly attached to the turret was the optical lever vacuum chamber. The optical lever was placed in this chamber where the pressure could be lowered to minimize noise caused by convection currents. A 2" diameter, ultra-high vacuum sapphire window was put in the turret wall so that the lever could illuminate the torsion balance mirror in the UHV chamber. The window and its mounting flange had a low overall thickness, to minimize that the distance between the optical lever and the balance mirror, as a larger distance would blow up filament ima ge on the mirror, cause loss of light, and also loss of image quality. The sapphire was of superior internal quality, both surfaces flat, with a good surface finish. A 180^{o} sector of a ring gear and a worm gear were used to rotate the system while under vacuum.

In melting the indium alloy, the heater expanded and moved away from the wall. The Chromalox 2500 watt heater was pinned against the wall in two diametrically opposite positions. The indium would first melt near these positions, and then heat conduction would melt the remaining (major) portion of the indium. The result was that it would take a long time to melt the indium seal, and that the upper part of the tank would become warm, resulting in outgassing. A redesign and installation of the heater would be a major problem, and so it was left. The indium melted in approximately 3-1/2 hours. Basically, due to outgassing, the pressure rose from the upper 10^{-9} torr base value, to a value of approximately 1×10^{-7} torr. Temperatures of the indium and of the heater coil were monitored by two iron-constantan thermocouples. When the indium seal was molten, very little force was required to turn the whole seal. When the indium solidified (by letting it cool down slowly over about 4 to 5 hours), a good vacuum seal was formed. The indium was cooled slowly as a porous solid was formed under rapid cooling. To test for any leak, the medium vacuum chamber was let up to atmospheric pressure. If the proper procedures had been followed, the UHV pressure level would not change.

The torsion balance was supposed to be positioned such that the torsion fibre and mirror and target were all in a plane 1/4" away from the front wall of the turret. Furthermore, the target was to be positioned such that the centre-line of rotation of the rotor assembly passed through the plane of the surface and coincided with a major diameter of the circular target. This would mean that on rotation of the rotor to change the angle of attack of the target, the beam would still strike the projected area of the target in the centre. This operation was checked by looking at the value of d_o, the measured distance from the axis of rotation of the balance, to the centre of the area which the molecular beam covered on the surface. This value should remain constant. The values of d_o at 0^{o}, 29^{o} and 41^{o} 15' angle of incidence of target normal to beam direction were 0.995 cm, 0.971 cm. and 1.031 cm. This amounts to a maximum variation of 0.06 cm., or 0.024". If the target plane were in front of (or behind) the centre-line of rotation this variation would be systematic in one direction only. This observed variation, however, can be explained by error in the instrument reading (of the moment arm), inaccuracies in the ball race, or most probably wobble (tilt) of the rotor. For example, a tilt of $\sim 3.6 \times 10^{-3}$ radians would induce a 0.010" displacement in the target. This wobble is certainly a possibility, as construction of the stainless steel rotor and stator was difficult, and warpage occurred on welding of components.

In conclusion, the overall performance of the rotatable seal was satisfactory. Redesign of the heater would lower the time required to change the

angle of attack, and outgassing would be reduced. The moment arm for the force measurements varied by only 6% on rotation of the UHV seal, but this was unimportant as the moment arm could be accurately determined by external means.

APPENDIX E: THE OPTICAL LEVER

The optical lever was built by Moskal[64] in a manner similar to that of Jones et al[65,66,67] and Pearson and Wadsworth[68]. A schematic of the lever is shown in Fig. 21 and a photograph of it in Fig. 22. The optical lever description is as follows: An image of the source S is focussed by the condensor lens L_1 on the mirror M. The light reflected from M is focussed by the lens L_2 (identical to L_1) on the surface of the double photocell. The elements G_1, G_2, P_1, P_2 and L_3 are placed in the optical path between L_1 and L_2. The grid G_1 is illuminated by the light coming from L_1, and is situated such that the light diverging from any point on G_1 is made parallel by lens L_3. This parallel light is reflected by the mirror M as a parallel beam which passes through L_3 again. If grid G_2 (a replica of G_1) is placed the same distance from L_3 as G_1, then light from a point on G_1 is focussed on a corresponding point of G_2. Thus an image of G_1 appears on grid G_2. This image is the standard auto-collimated image which has unit magnification.

The glass plate P_1 is split in the centre, and one-half of the plate is placed on each side of the optical axis. One part of P_1 is rotated so that one-half of the image of G_1 on G_2 is displaced by the width of an opaque spacing of the grid. Thus if the left half of G_2 passes light which has passed through G_1, then the right half of G_2 stops light from G_1. Upon rotation of the mirror, the light coming through each side of G_2 undergoes a periodic variation, with the variation of the light from one side 180° out of phase with the other.

A split photocell is placed behind lens L_2 such that each half is illuminated by light which has come from only one side of P_1. The lever is operated in the balanced condition where an equal amount of illumination falls on each half of the photocell. This balancing is accomplished by the rotation of the plate P_2. This plate shifts the whole image of G_1, thus varying the amount of illumination reaching the photocells. To achieve a lower change in sensitivity of the photocells with change in surrounding temperature at very low light levels, the split photocells were replaced by two Texas Instrument LS 400 silicon photo devices.

The sensitivity, range of operation, and other details of the performance of the optical lever are embodied in the main portion of the thesis.

APPENDIX F: METHOD OF WIRE ATTACHMENT FOR THE TORSION BALANCE

A number of connections between a wire (torsion fibre, stiff fibre, etc.,), and a cylinder (mirror holder, copper bob), had to be accomplished. Each wire-to-cylinder joint for the components of the torsion balance was made by the following methods. At the end of each cylinder was a converging hole. A slightly undersized split cone was manufactured to fit this converging hole. A wire identical to that which was to pass through the cones was placed over the axis of the flat part of the one half of the cone, the other half put on, and then the assembly was placed in a master jig and pushed in, compressing the softer copper parts of the cone almost together over the harder wire (for example, the 0.010" W wire). This in effect, "drilled" an undersized small diameter hole down the center of the cone. The two pieces of the split cone were then forced back out of the jig, and the proper wire placed in the cone. Then the assembly was put in the proper converging receptacle on the copper bob, or the mirror mount, with sufficient force to hold everything together. Because of its physical size and difficulty in handling, the 0.001" diameter tungsten wire had to be treated slightly differently. It was necessary to manufacture a jig to stretch out and hold the tungsten wire over a half of the split cone. The two were moved about until the wire stretched down the axis of the cone. This procedure was checked microscopically. Then, without disturbing the positioning, the wire was attached to the half of the cone by a copper electro-deposition process. The length where the tungsten wire was to be attached to the copper cone was first cleaned cathodically in a solution, rinsed, activated in a dilute acid, rinsed and coated with a layer of nickel. Then, the copper was deposited over the wire and cone by a standard method[69]. The matching half of the split cone could then be mated with the cone-half having the attached wire and the assembly could be forced into the converging receptacle. The torsion wire would automatically be centered. The above method of wire attachment was cycled in a test to 400° C with a 58 gram weight hanging from the end of the test apparatus. The test wire was not electro-deposited onto the cone. No slippage occurred.

APPENDIX G: PREPARATION OF THE TUNGSTEN TARGETS

The polishing procedure involved the following steps. The metal target was potted in a hard plastic, which helped prevent rounding of the target edges due to the polishing process. The surface to be polished was flush with the front surface of the potting compound. The target was then subject to a series of mechanical grinding processes, each of which left a smoother, less damaged surface. Carborundum papers lubricated with flowing distilled water were used in the first, coarse grinding stage. The target was first polished in one direction on one paper. Following this, the sample was washed throughly with water and alcohol, and then dried with a blower. The sample was then polished on a finer grade of paper with the polishing motion 90° to the former polishing direction. Polishing continued until the surface was uniformly scratched in this direction, and all evidence of previous polishing (coarser) scratches had disappeared, as checked by observation under a low power microscope.

After finishing with the 4/0 grade of paper, the target polishing was continued on a nylon cloth mounted on a flat rotating disc, using 6 micron diamond paste and a varsol lubricant. The next polishing step was 1 micron diamond paste on microcloth, and the final step involved the use of 0.05 micron aluminum oxide power mixed with a distilled water solution. The resulting target was highly reflective, optically flat over most of the surface (rounded at the edges), and only very small scratches could be seen under an optical microscope at 1000 x magnification.

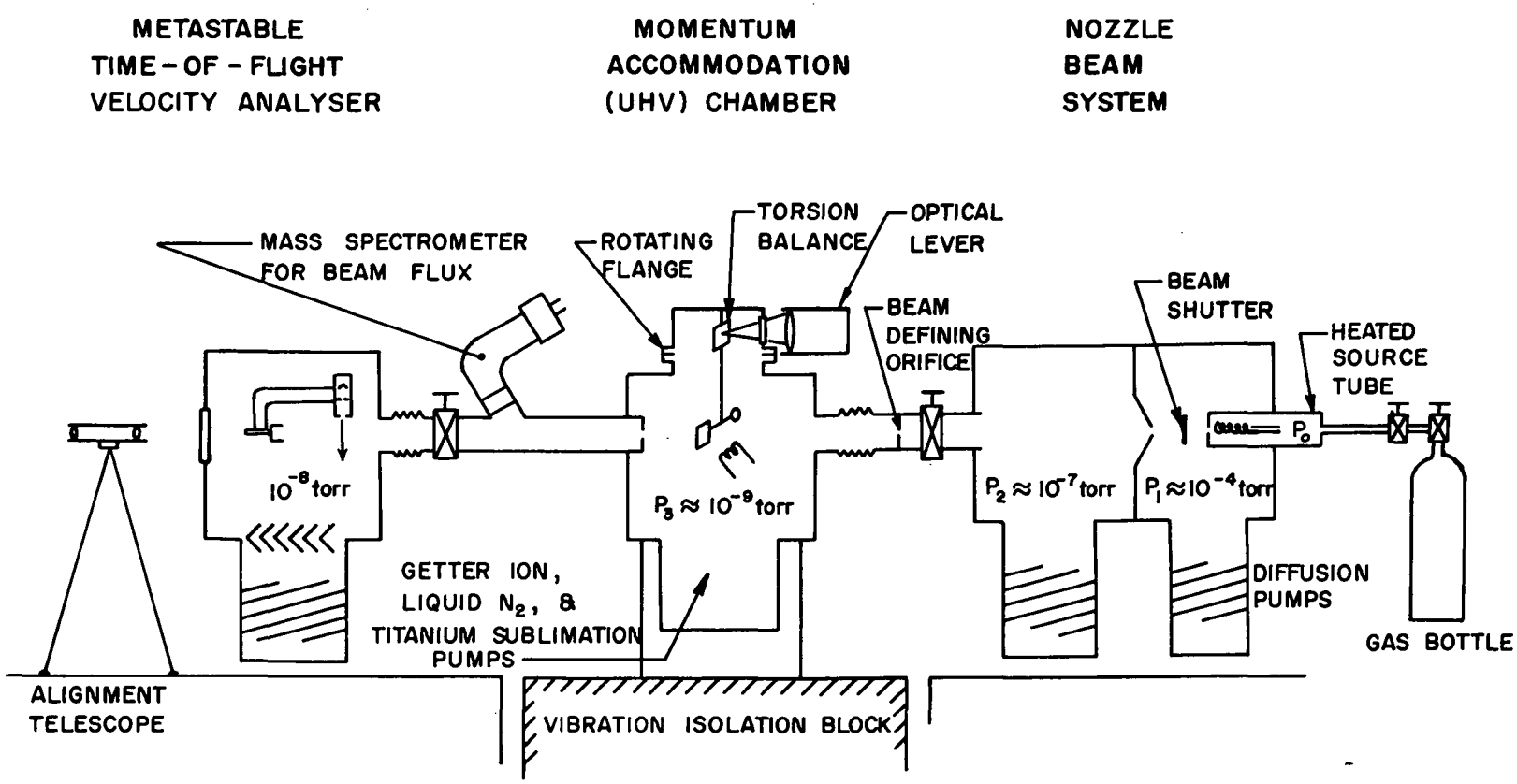

FIG. I SCHEMATIC OF ACCOMMODATION COEFFICIENT APPARATUS

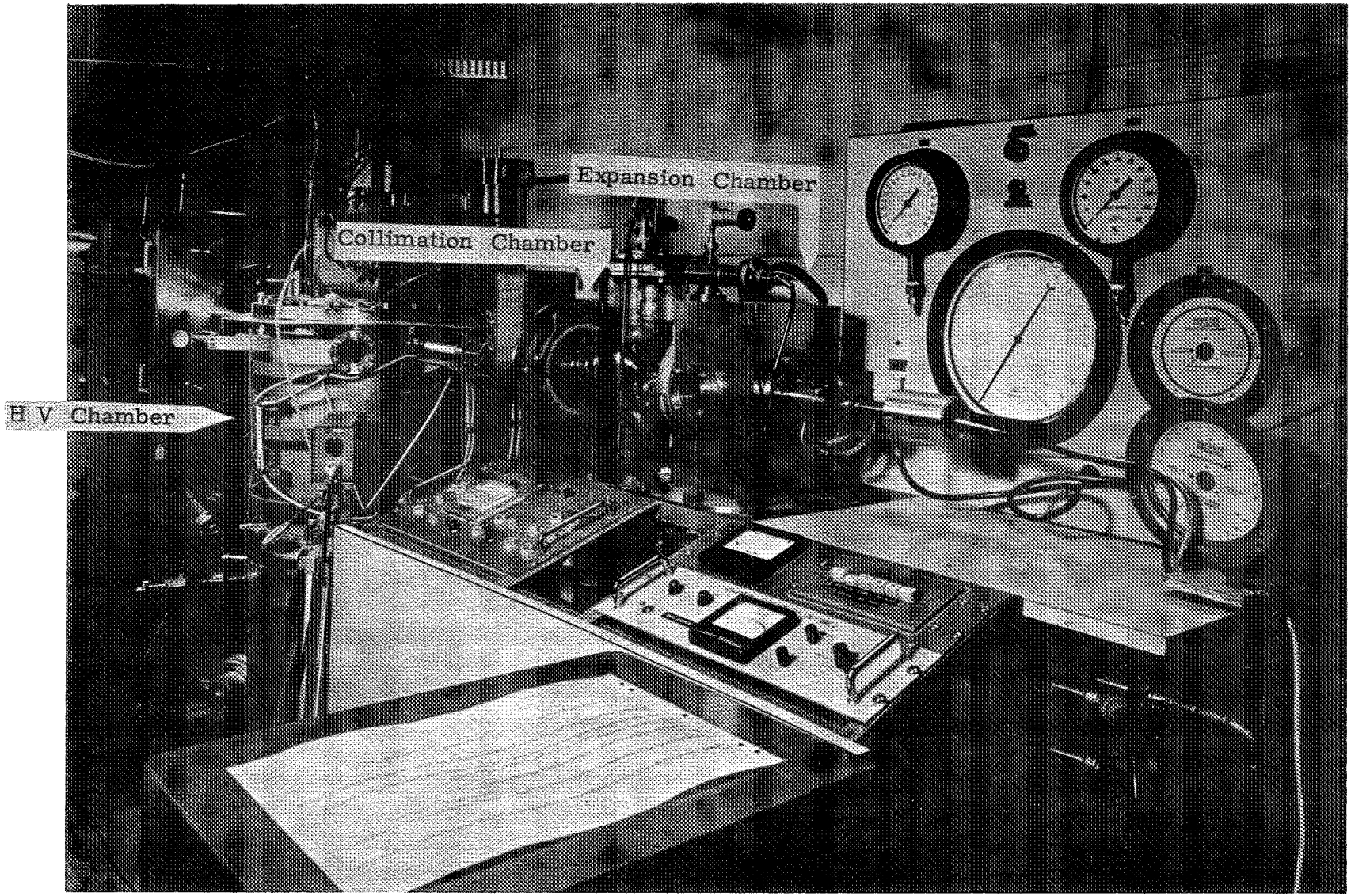

FIG. 2 VIEW OF NOZZLE BEAM SYSTEM AND FRONT OF UHV CHAMBER

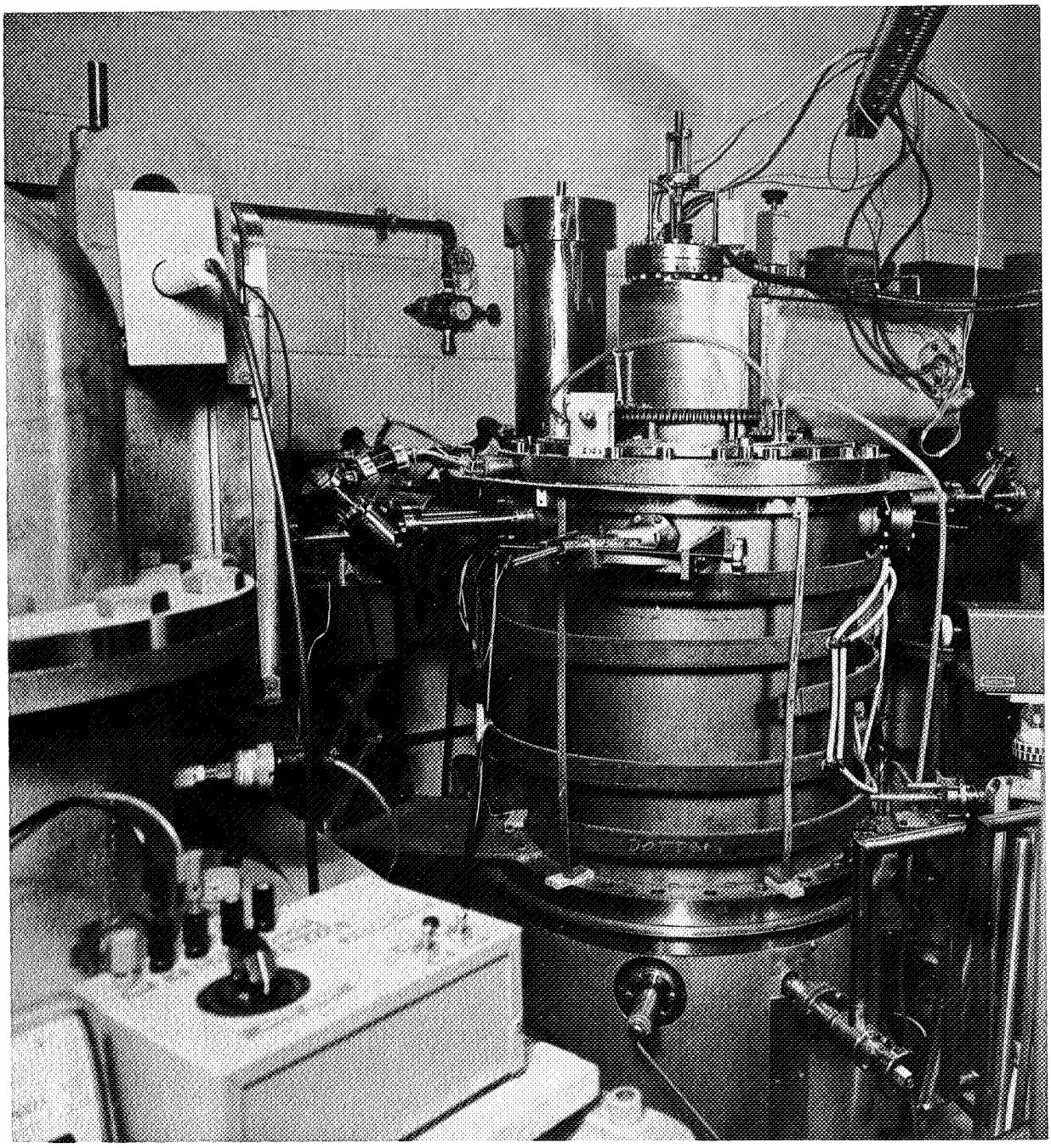

FIG. 3 REAR VIEW OF UHV CHAMBER

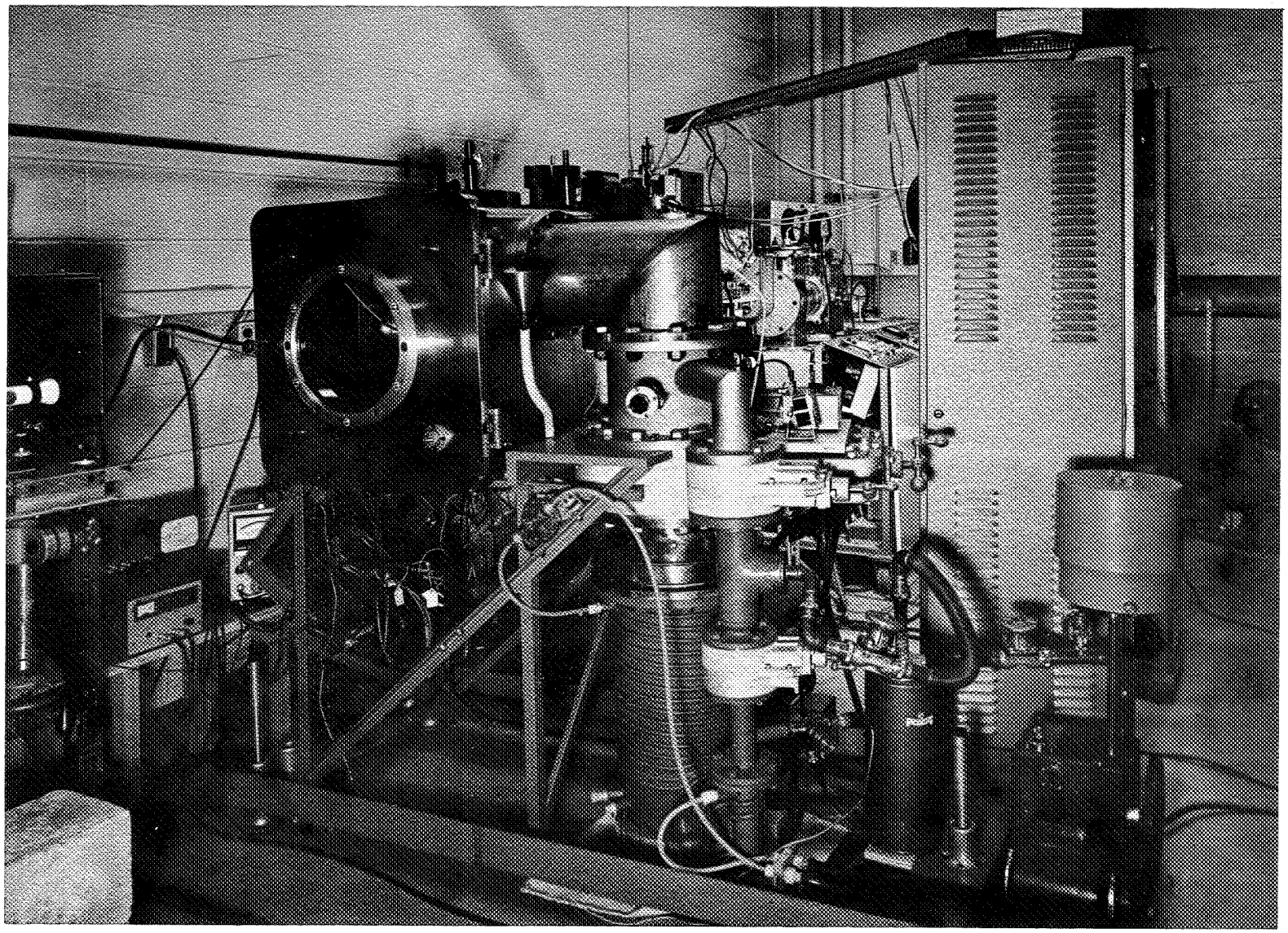

FIG. 4 VIEW OF METASTABLE TIME-OF-FLIGHT VELOCITY ANALYZER CHAMBER

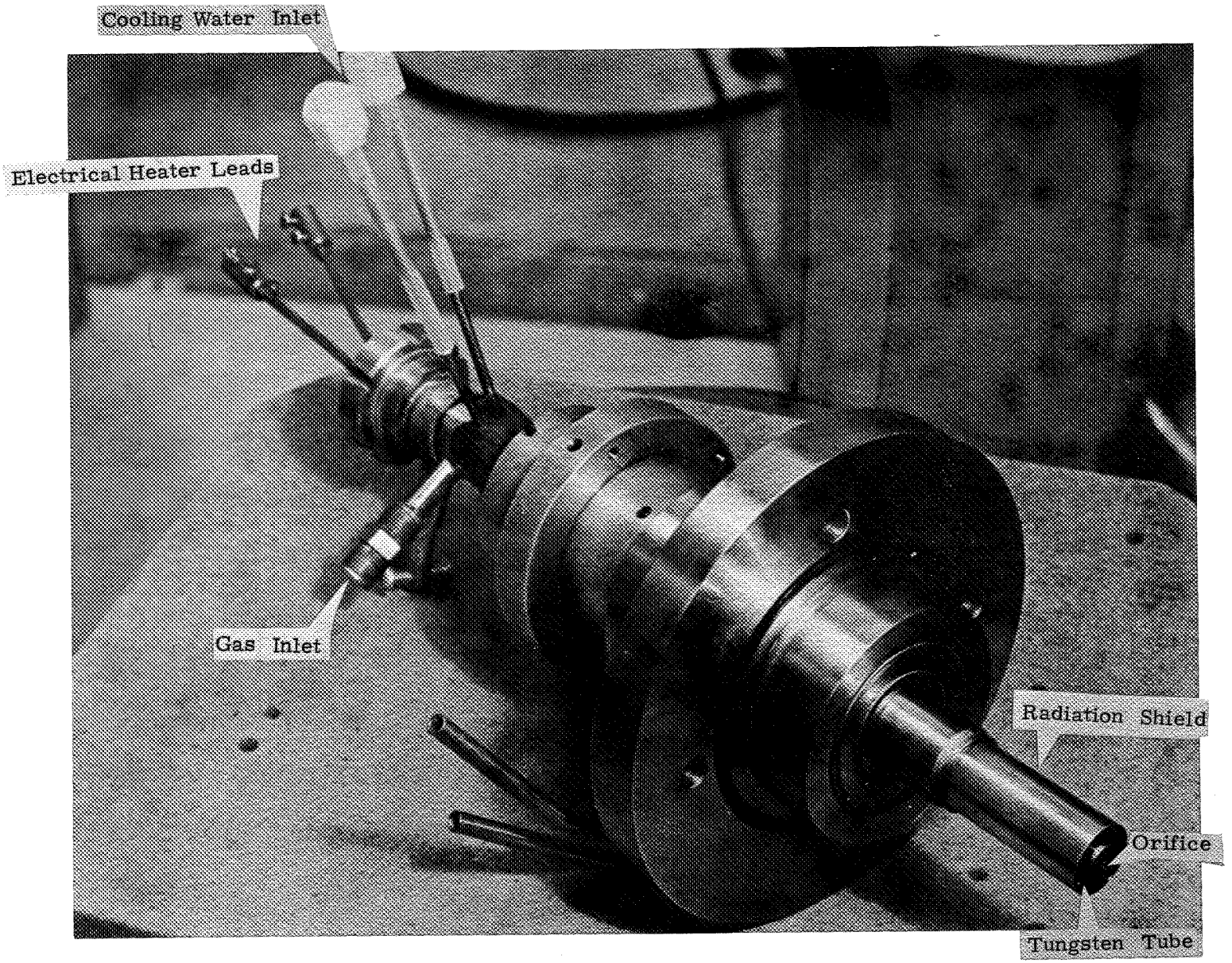

FIG. 5 PHOTOGRAPH OF SOURCE TUBE AND HOLDER

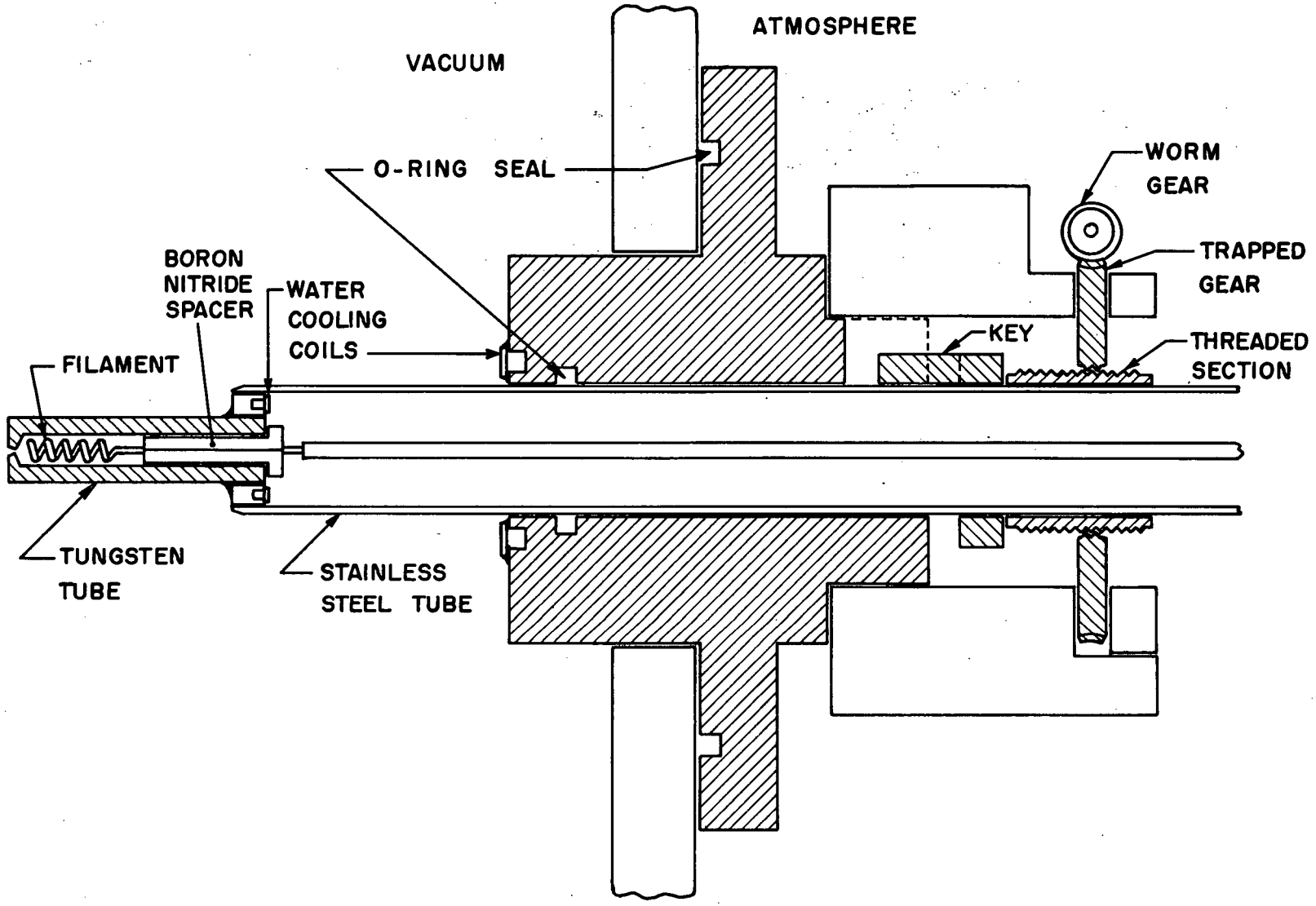

FIG. 6 CROSS SECTION OF SOURCE TUBE, HOLDER & MOTION DEVICE

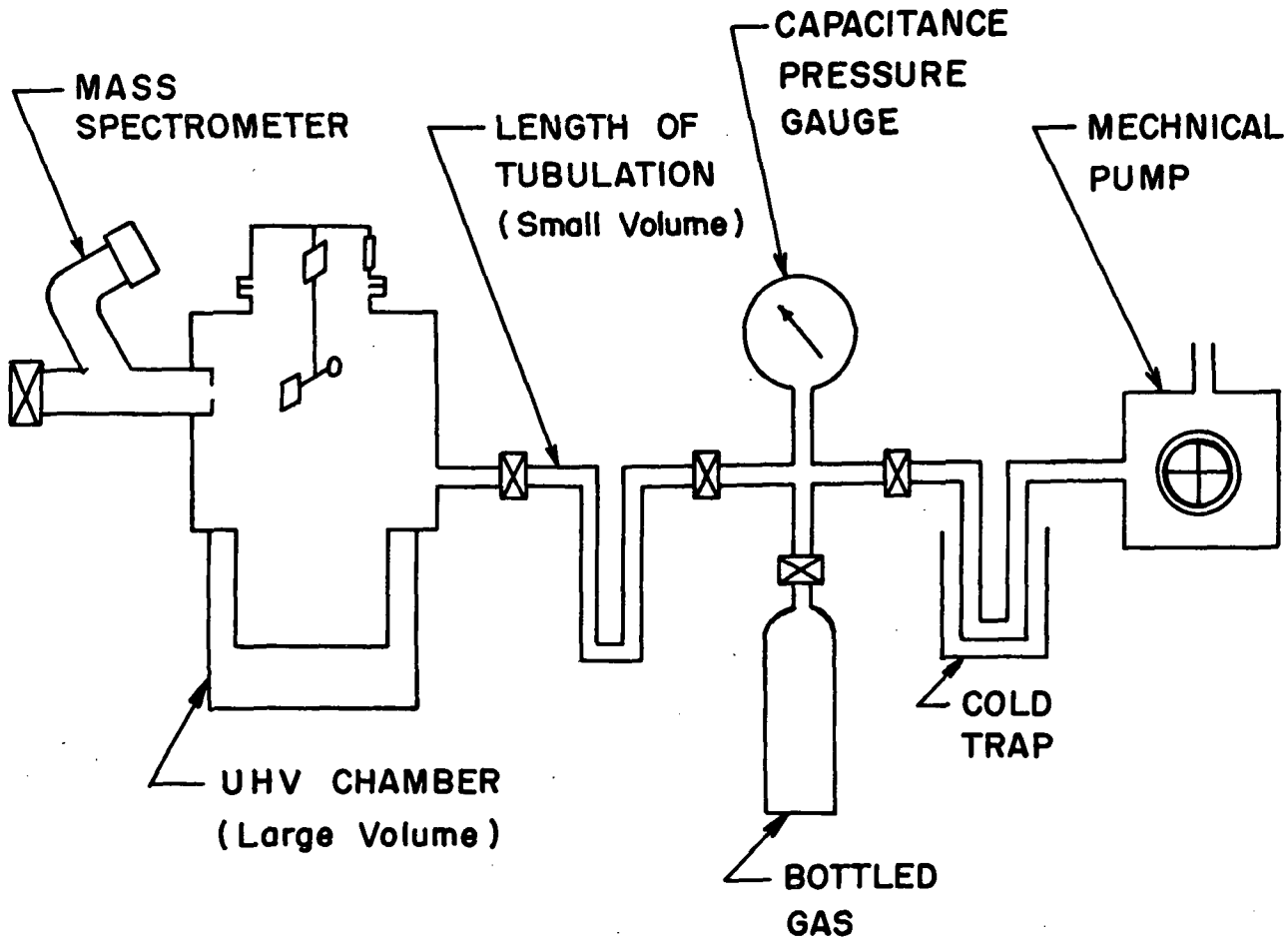

FIG. 7 MASS SPECTROMETER CALIBRATION SYSTEM

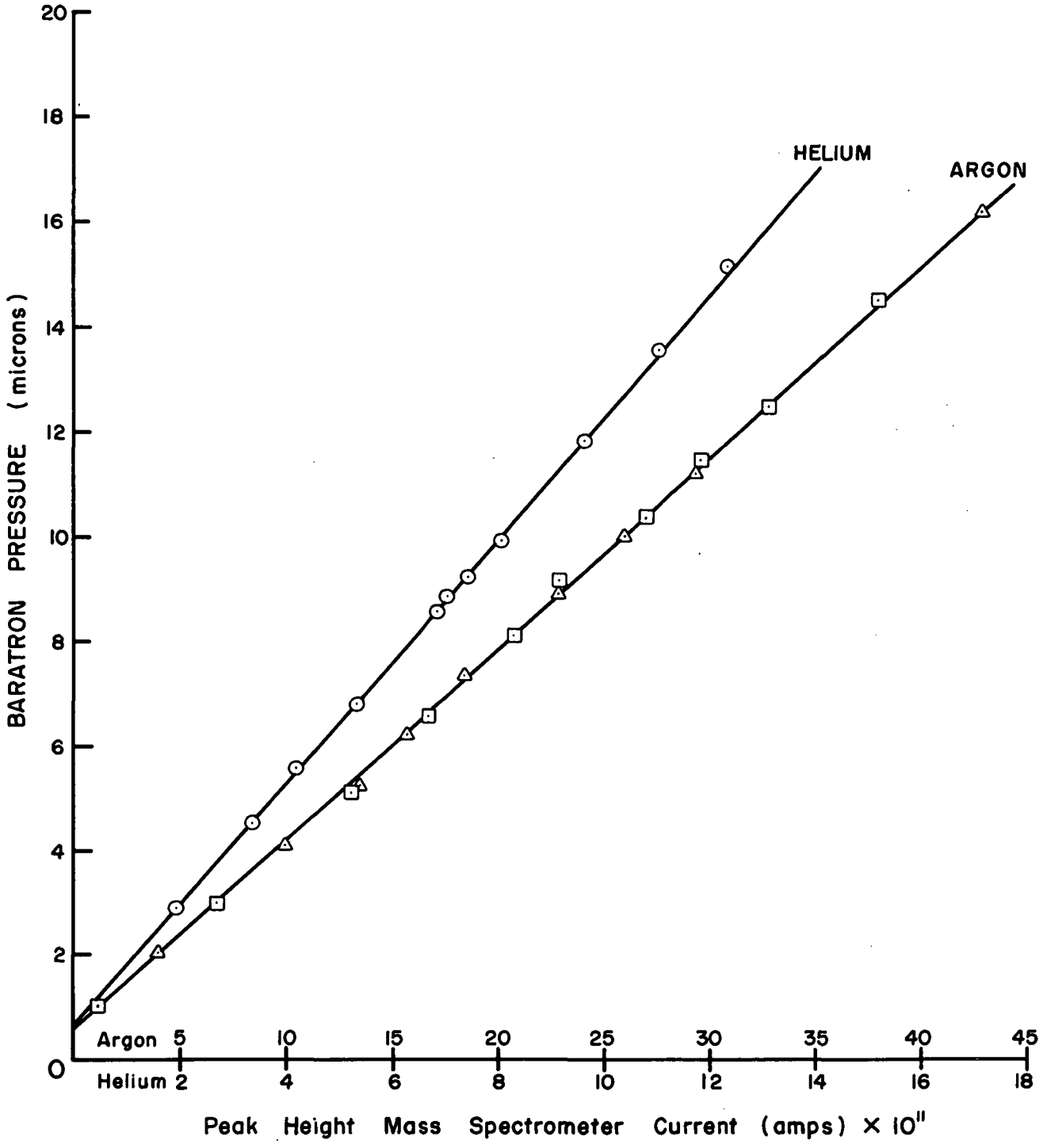

FIG. 8 RESULTS FOR MASS SPECTROMETER CALIBRATION

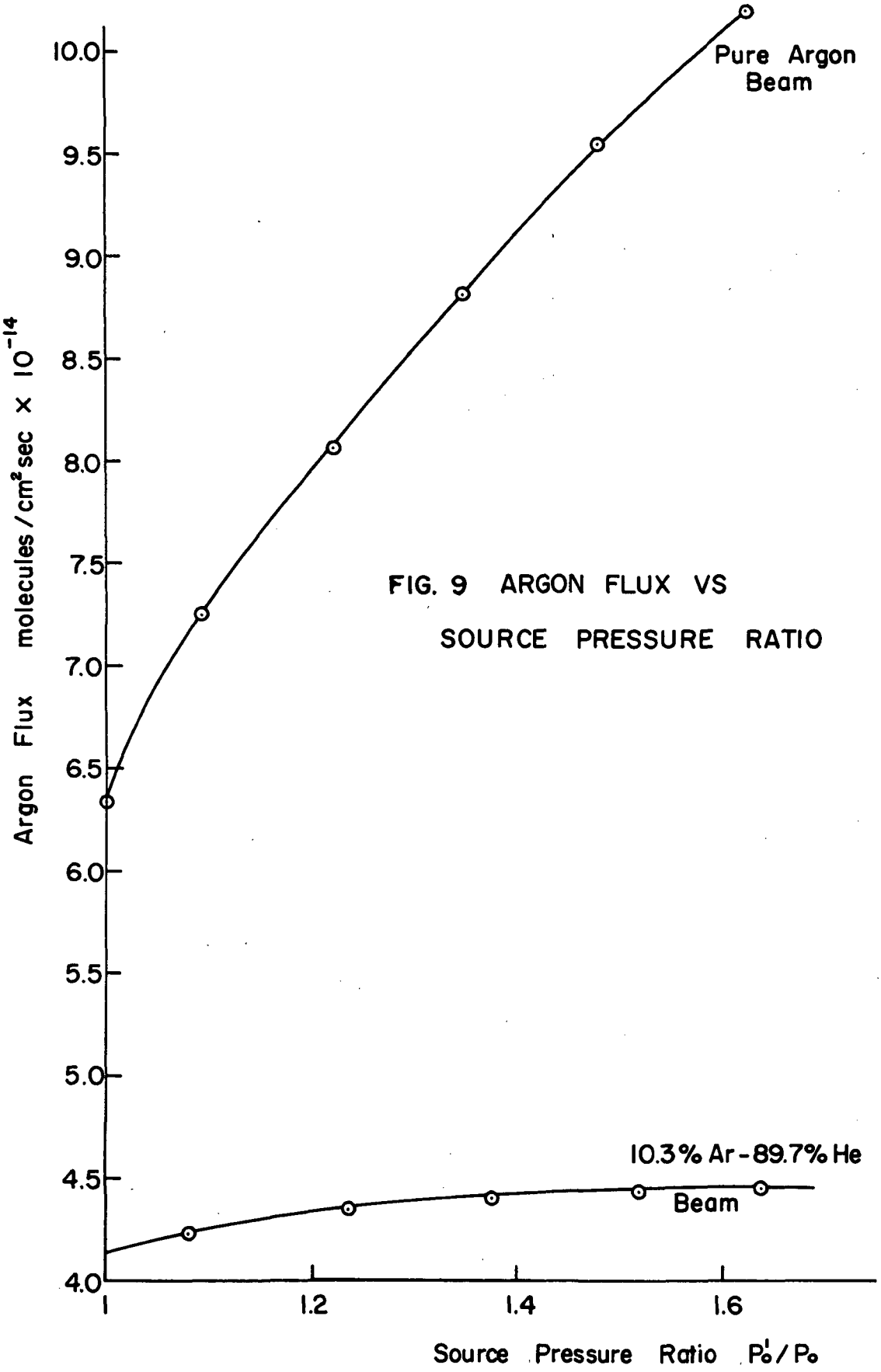

FIG. 9 ARGON FLUX VS SOURCE PRESSURE RATIO

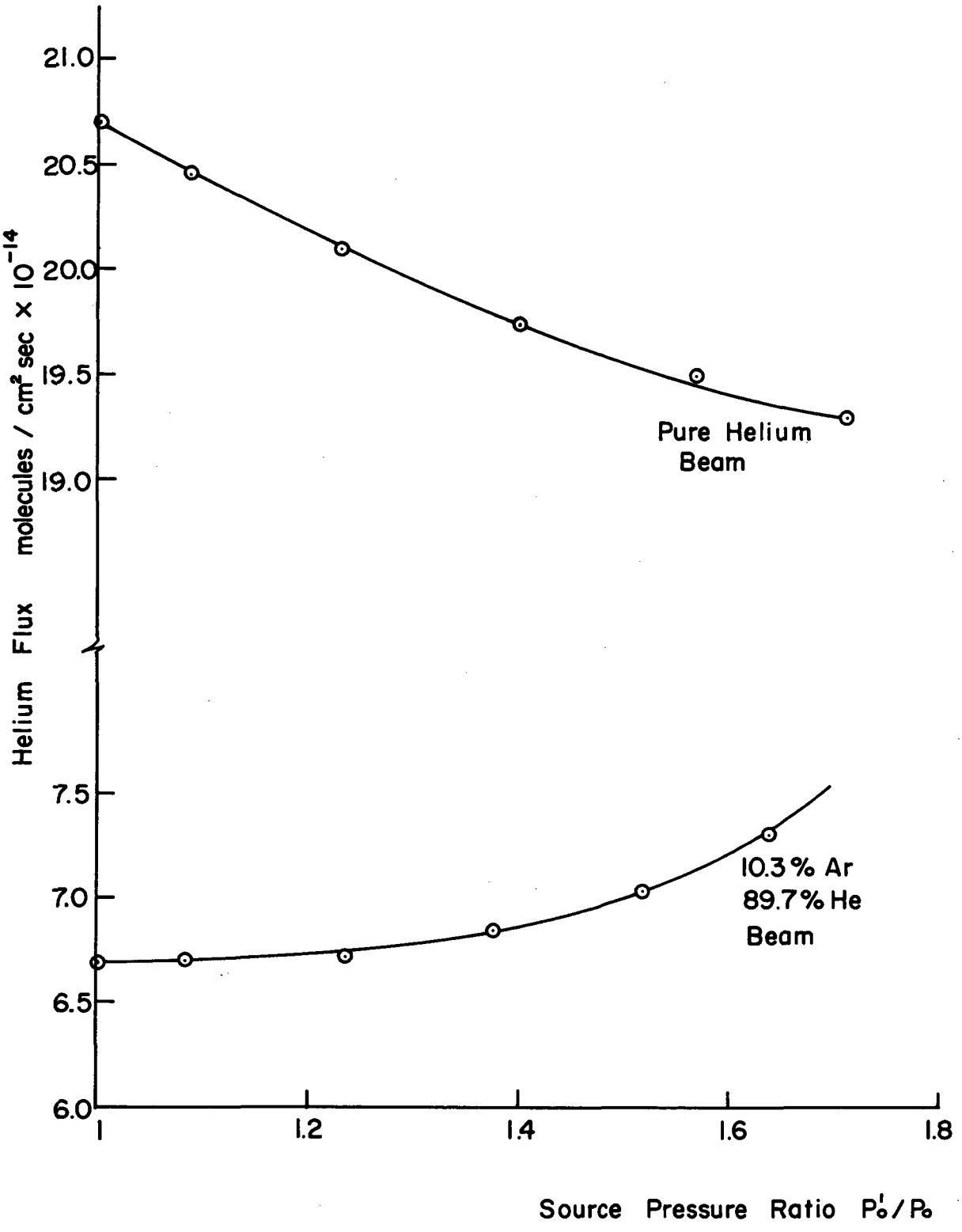

FIG. 10 HELIUM FLUX VS SOURCE PRESSURE RATIO

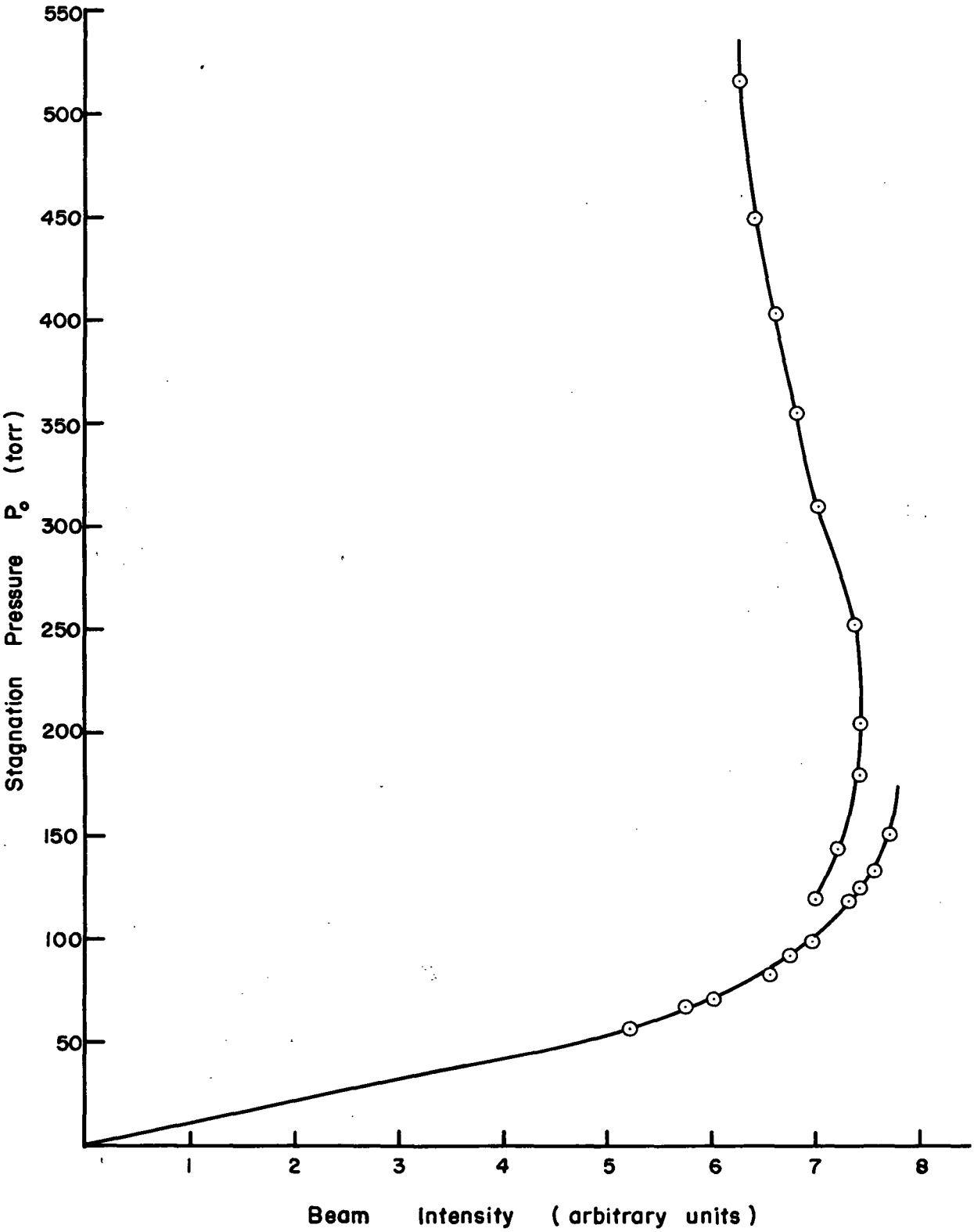

FIG. 11 GENERAL BEHAVIOUR OF $\mathcal{C}_L$ BEAM INTENSITY WITH STAGNATION PRESSURE AT ROOM TEMPERATURE FOR A CONVERGING — DIVERGING NOZZLE

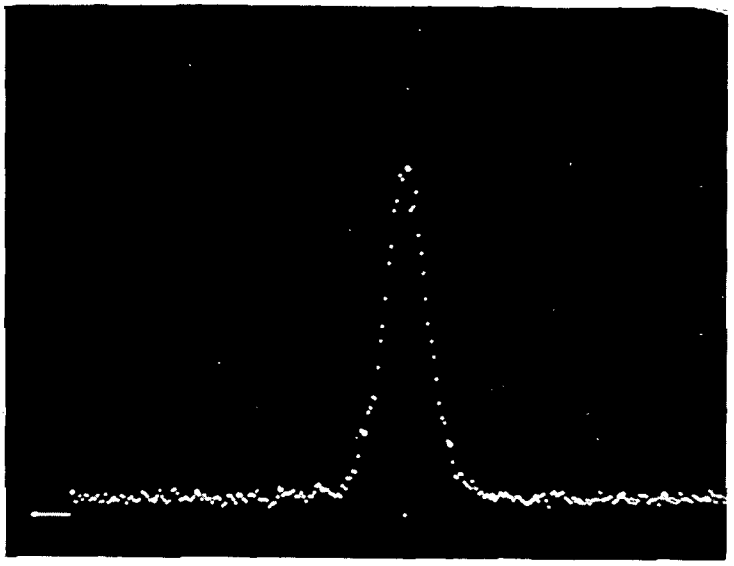

FIG. 12A TIME-OF-FLIGHT DISTRIBUTION FOR A ROOM TEMPERATURE PURE ARGON BEAM. THE PEAK CORRESPONDS TO A VELOCITY OF 555 M/SEC.

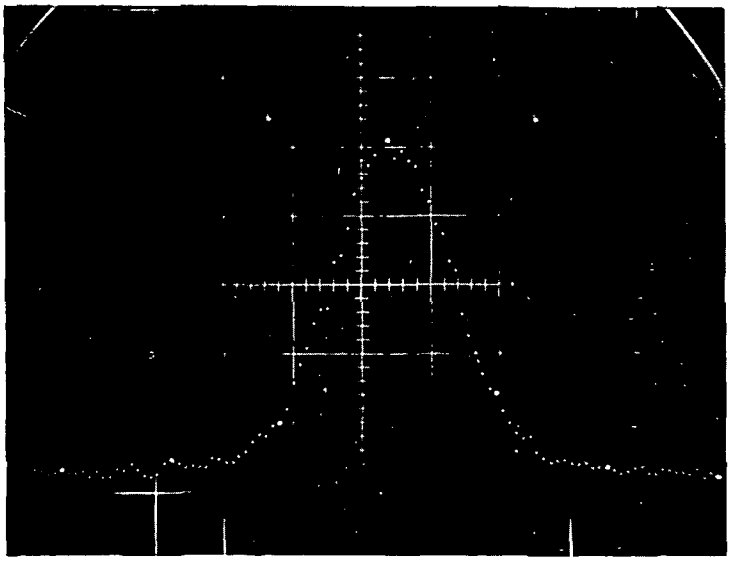

FIG. 12B TIME-OF-FLIGHT DISTRIBUTION FOR A HEATED PURE ARGON BEAM. THE PEAK CORRESPONDS TO A VELOCITY OF 830 M/SEC. NOTE THE EXPANDED TIME SCALE.

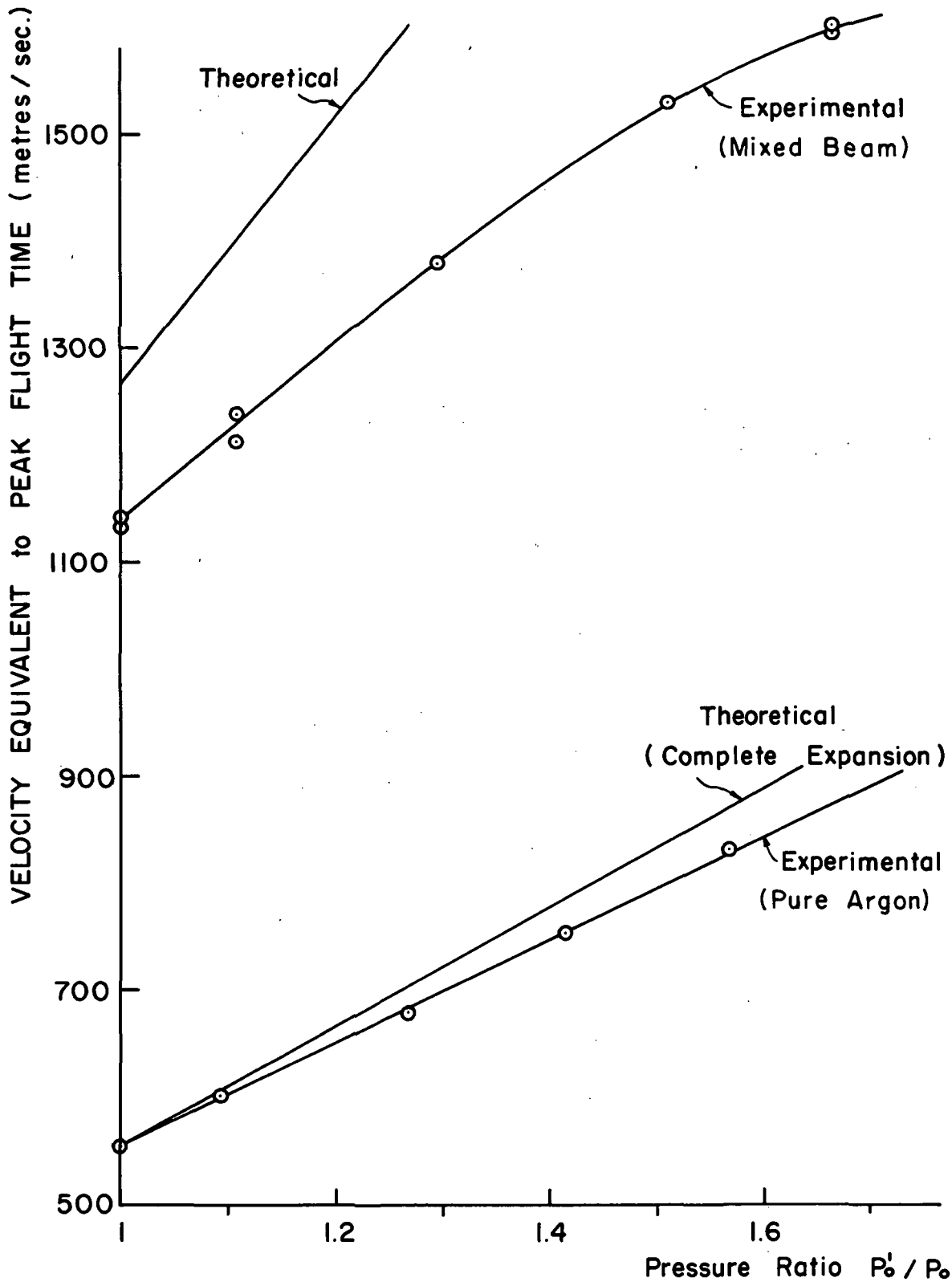

FIG. 13. BEAM VELOCITY VS SOURCE PRESSURE RATIO

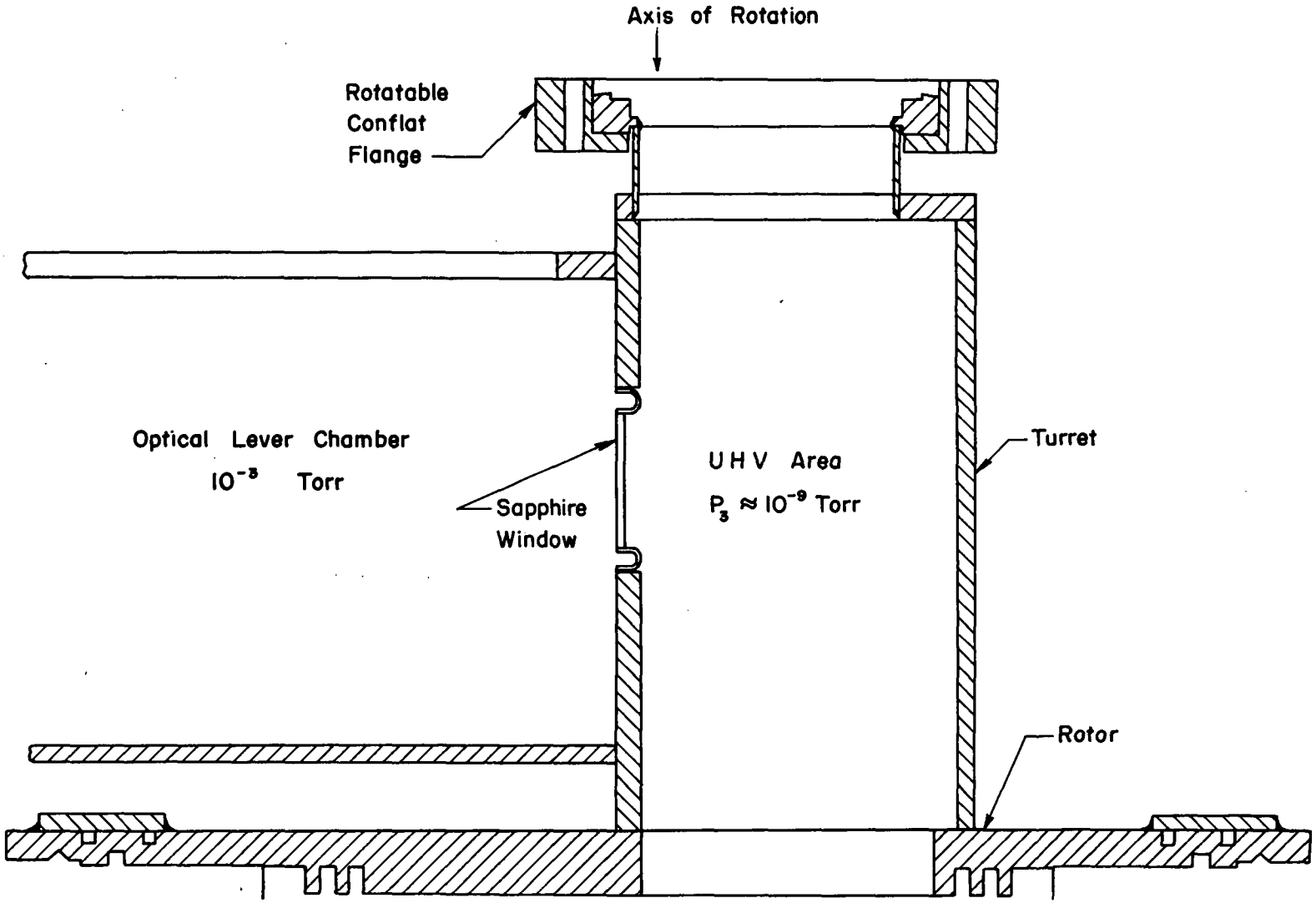

FIG. 14 CROSS SECTION OF UPPER PORTION OF U H V ROTATABLE FLANGE

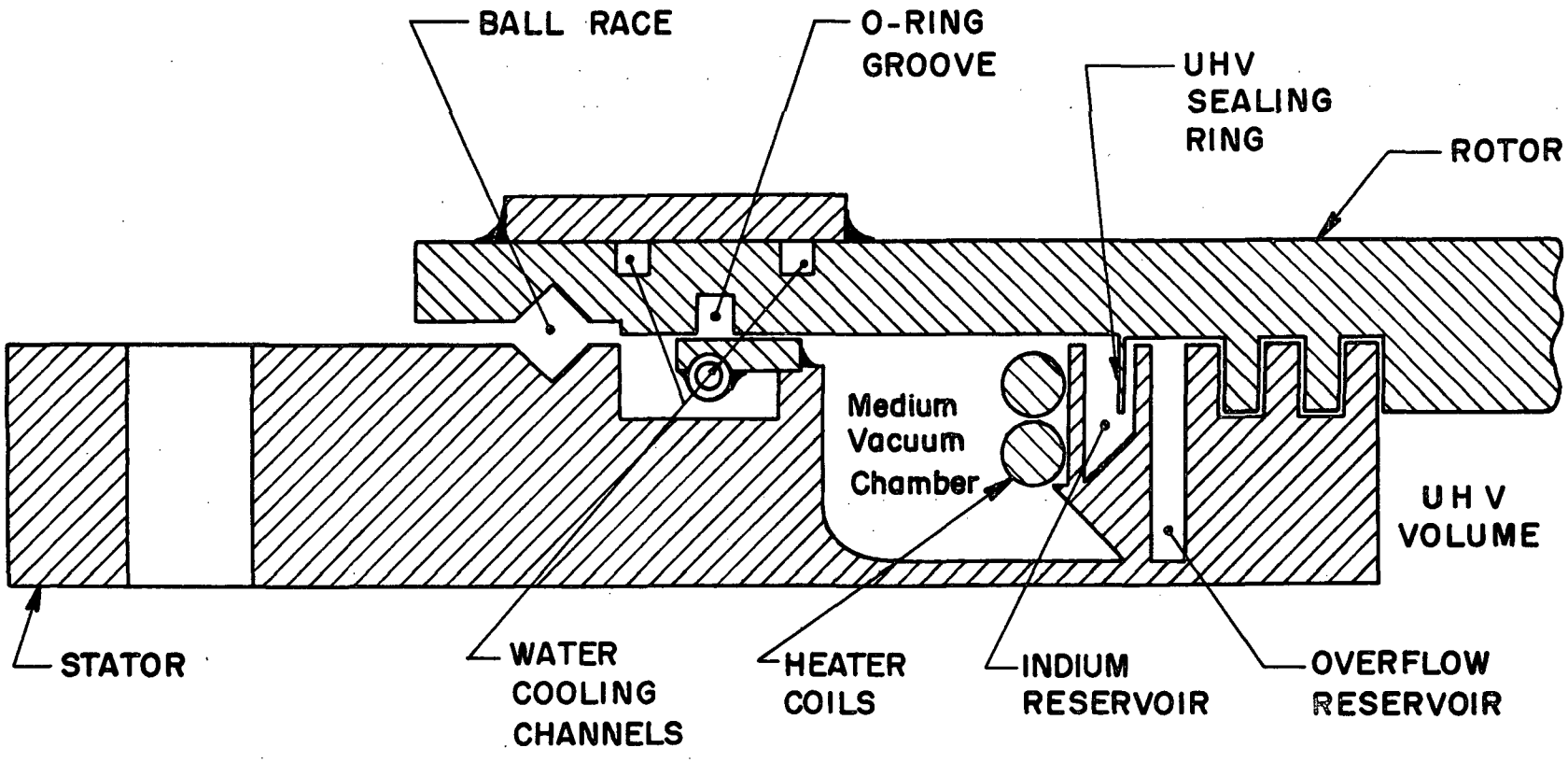

FIG. 15 DETAILED VIEW OF THE VACUUM SEALS OF THE UHV ROTATABLE FLANGE

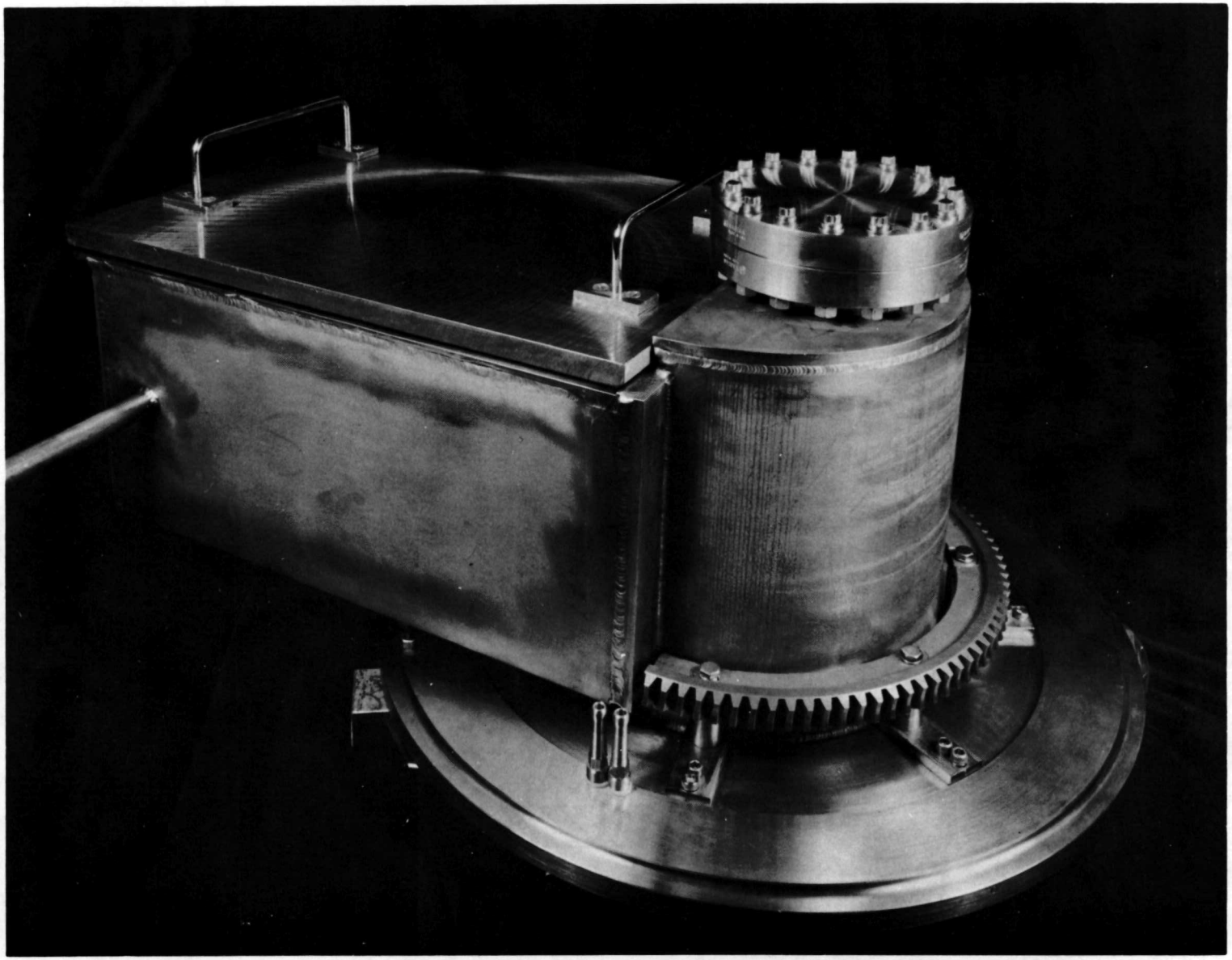

FIG. 16 PHOTOGRAPH OF THE ROTOR OF UHV ROTATABLE FLANGE

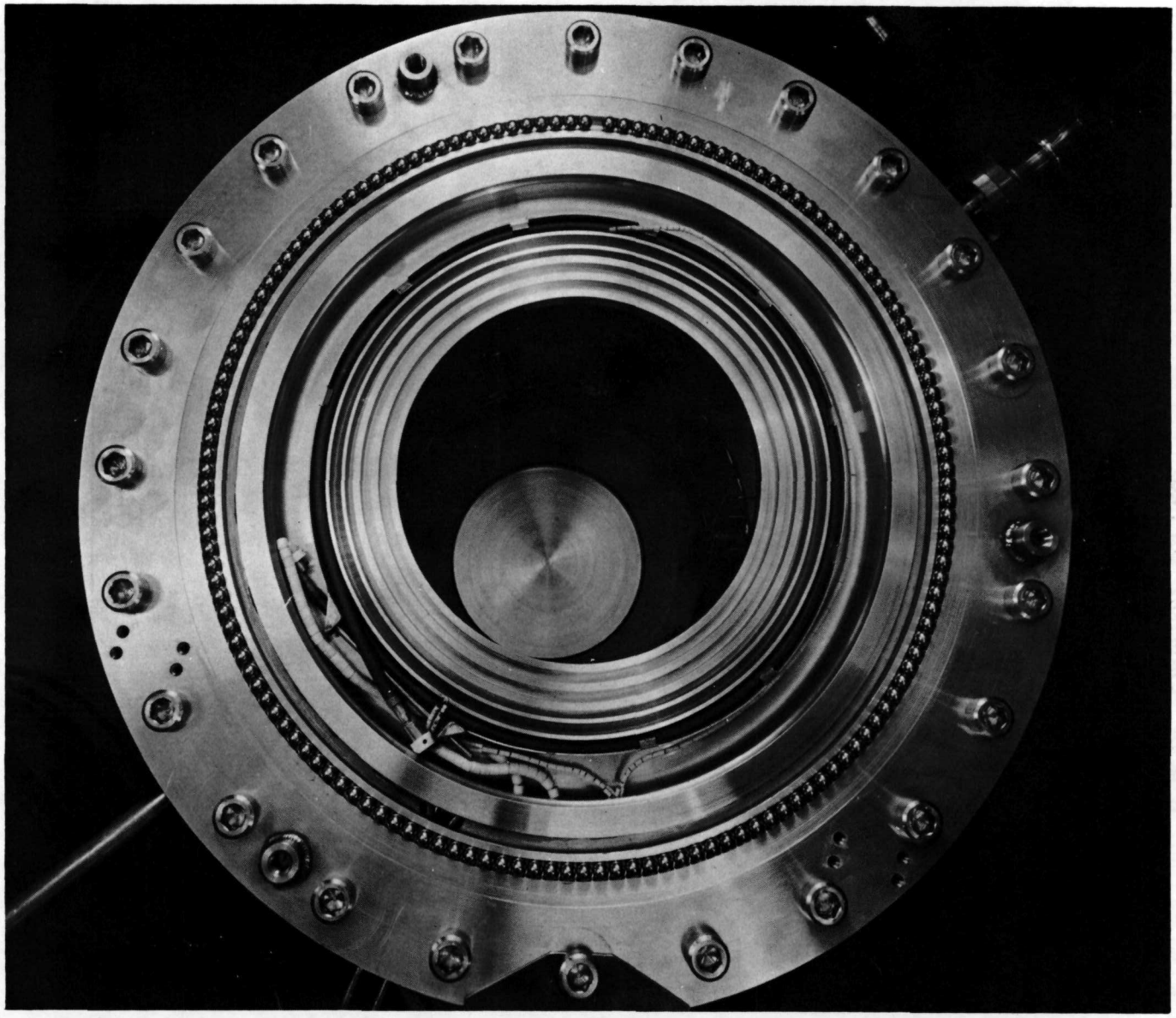

FIG. 17 PHOTOGRAPH OF THE STATOR OF UHV ROTATABLE FLANGE

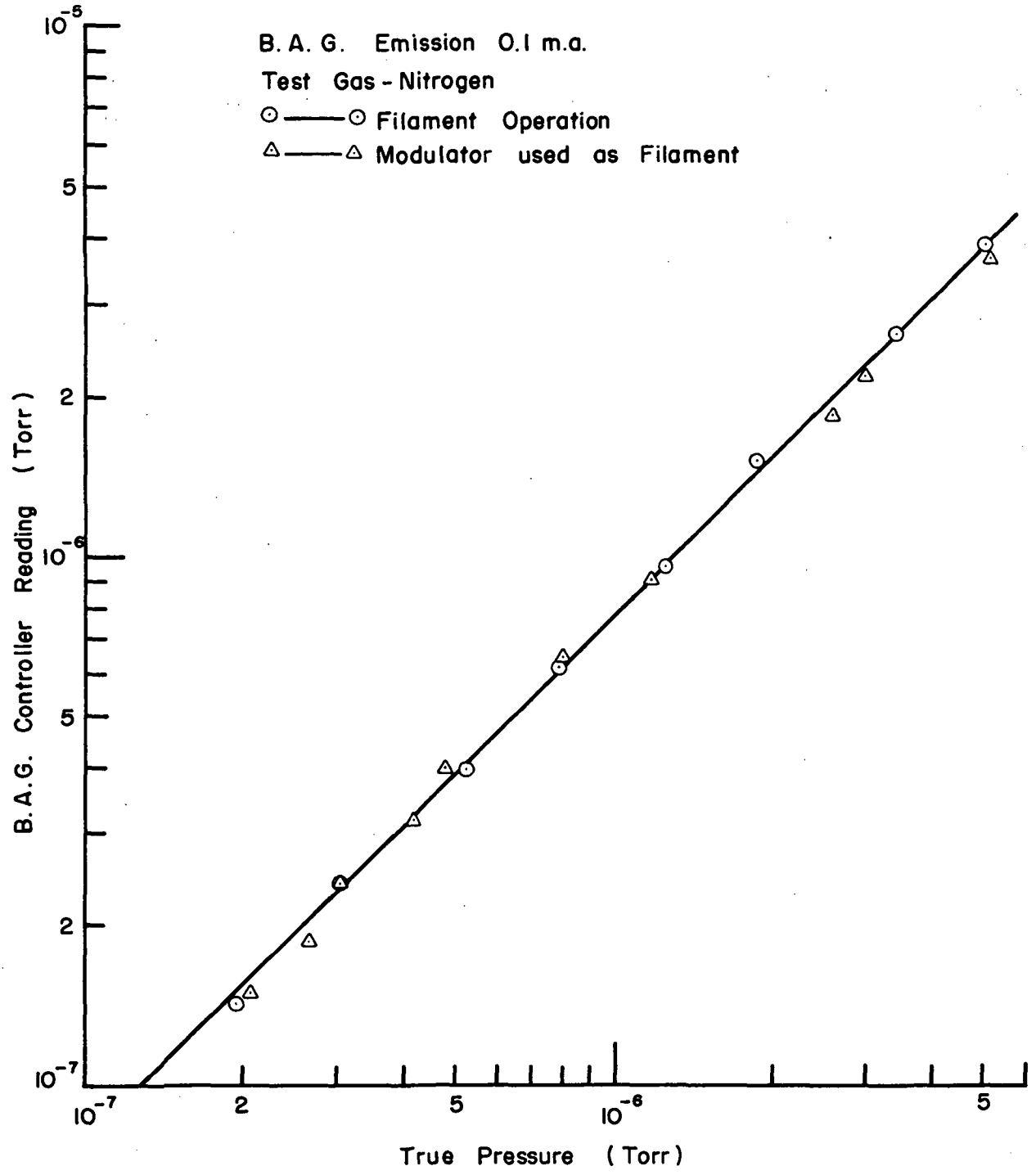

FIG. 18 CALIBRATION OF THE BAYARD-ALPERT GAUGE IN THE FLOW-THROUGH SYSTEM

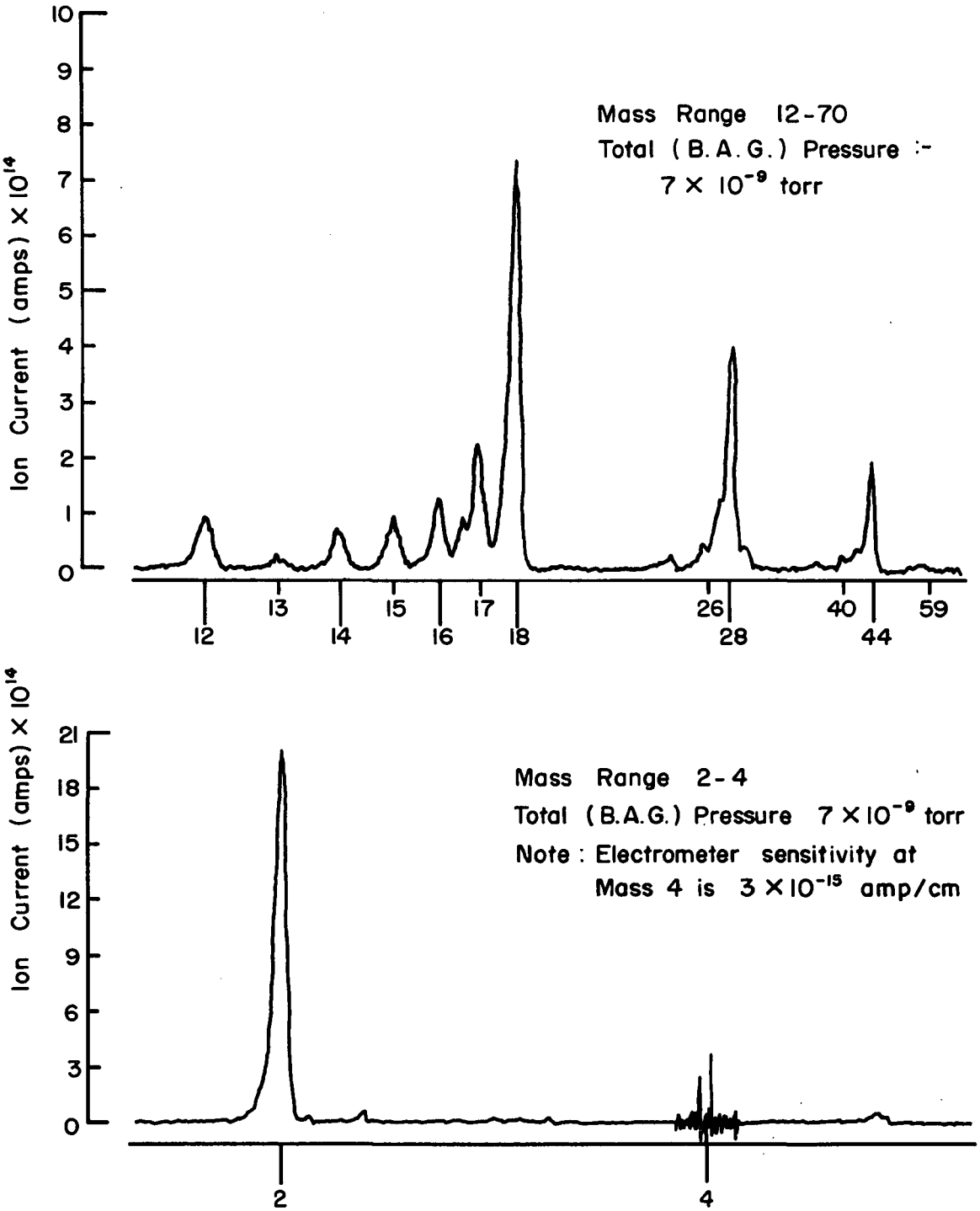

FIG. 19 MASS SPECTROMETER READING OF BACKGROUND GASES IN THE UHV CHAMBER

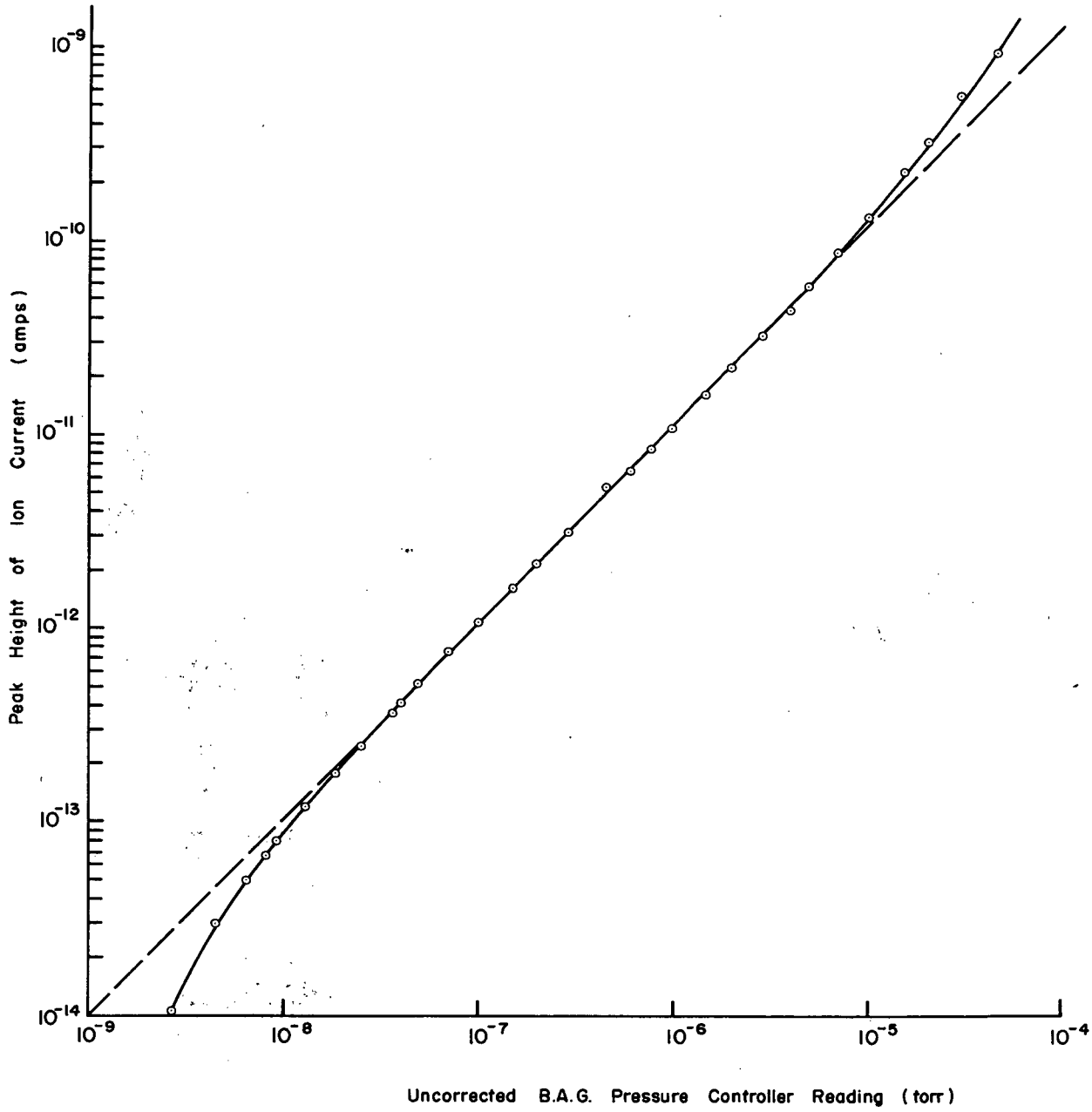

FIG. 20 CORRELATION of MASS SPECTROMETER & BAYARD-ALPERT GAUGE READINGS FOR THE GAS ARGON

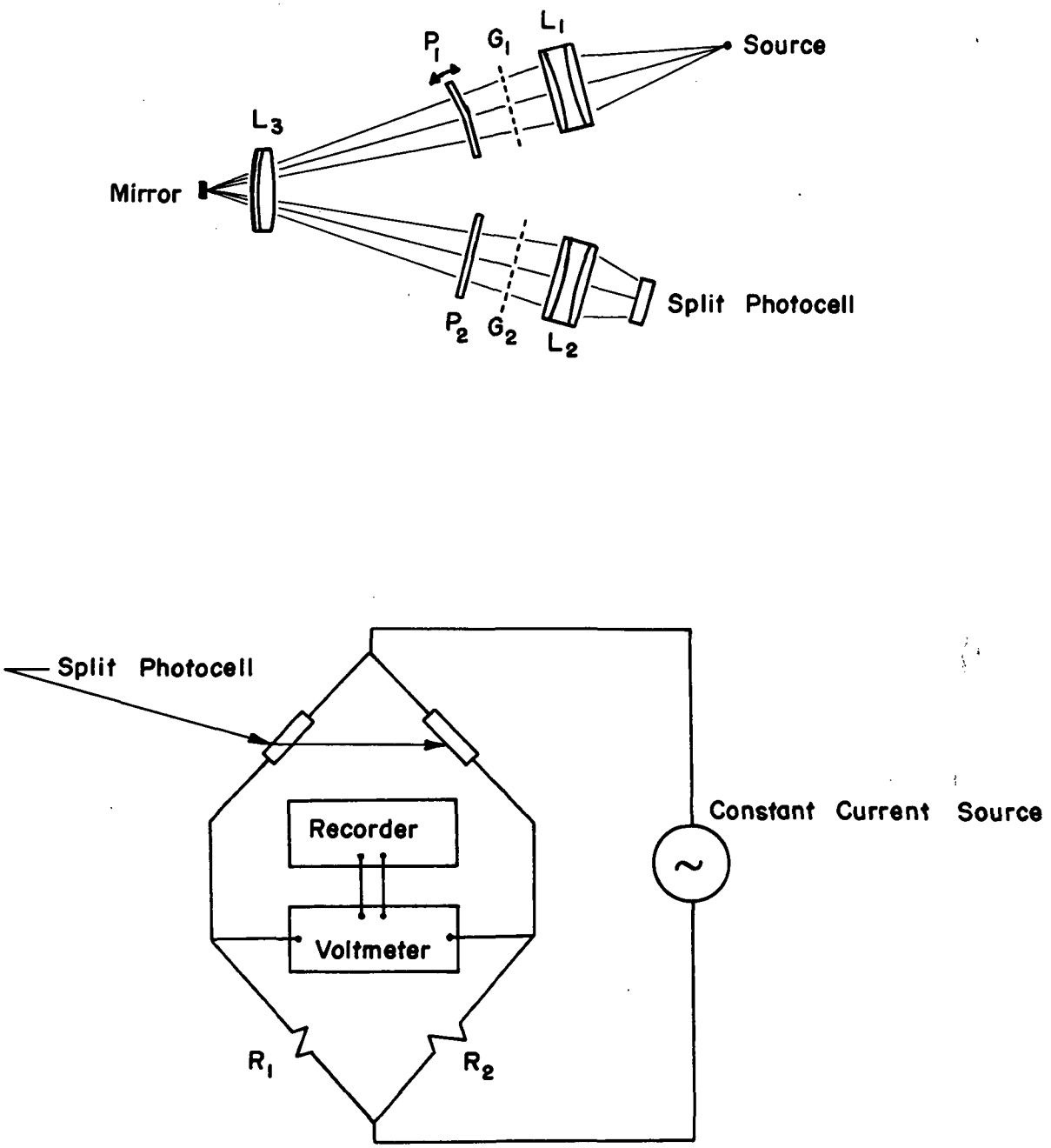

FIG. 21 SCHEMATIC DIAGRAM OF THE OPTICAL LEVER & OUTPUT RECORDING SYSTEM

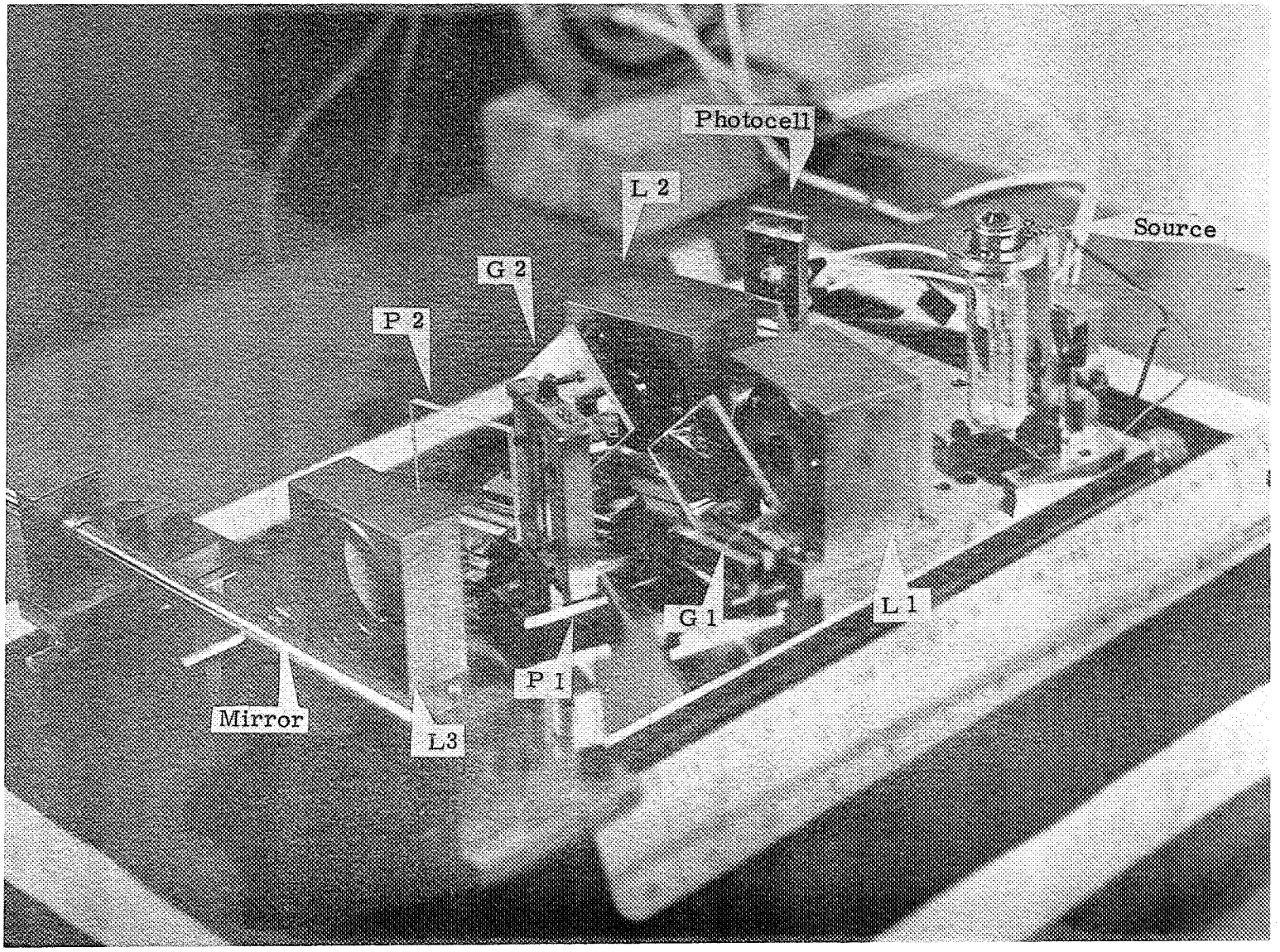

FIG. 22 PHOTOGRAPH OF THE OPTICAL LEVER BENCH AND COMPONENTS

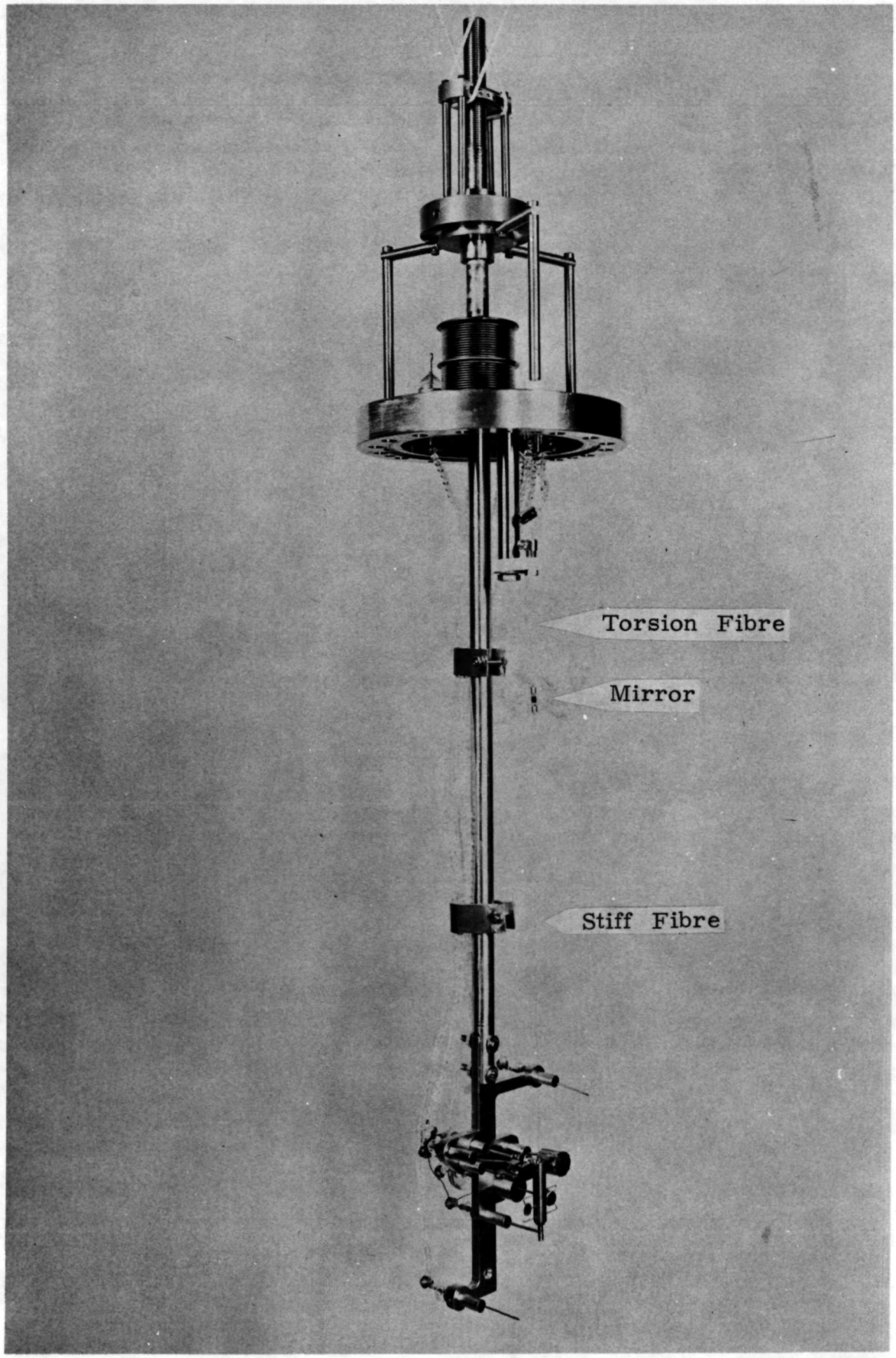

FIG. 23 PHOTOGRAPH OF COMPLETE TORSION BALANCE ASSEMBLY AND SUPPORT SYSTEM

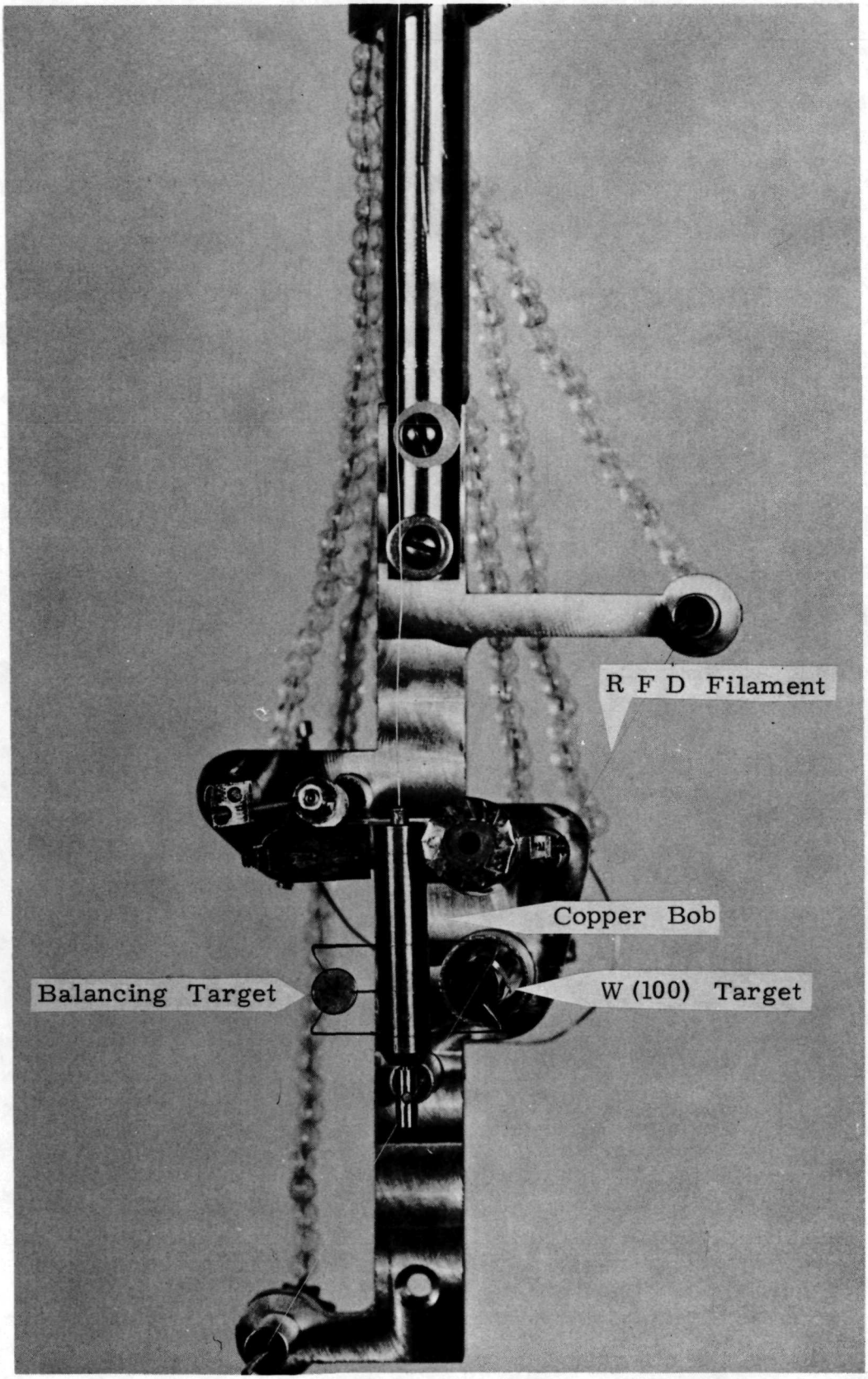

FIG. 24 FRONT VIEW OF LOWER PORTION OF TORSION BALANCE AND SUPPORT STRUCTURE

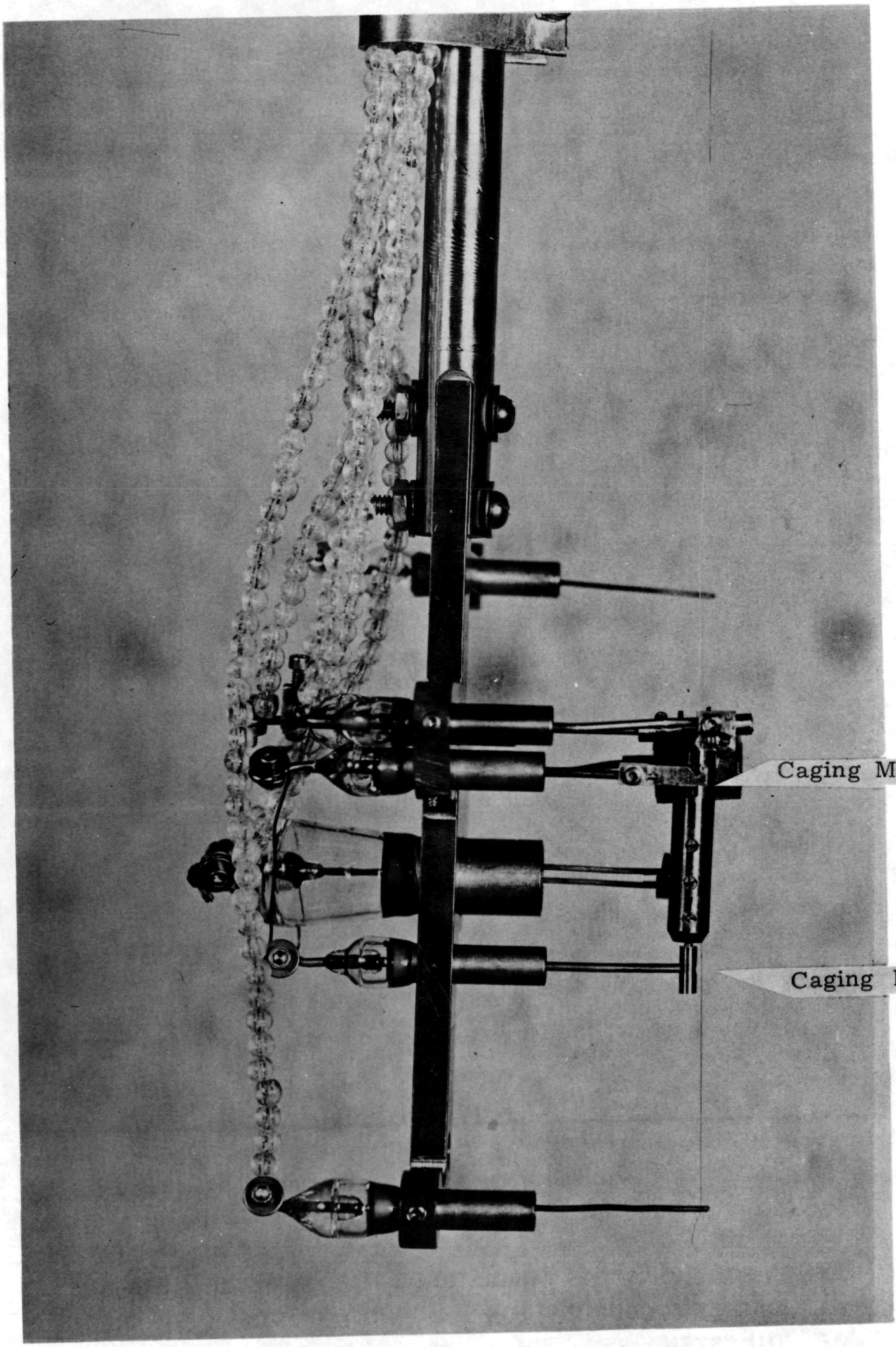

FIG. 25 SIDE VIEW OF LOWER PORTION OF TORSION BALANCE AND SUPPORT STRUCTURE

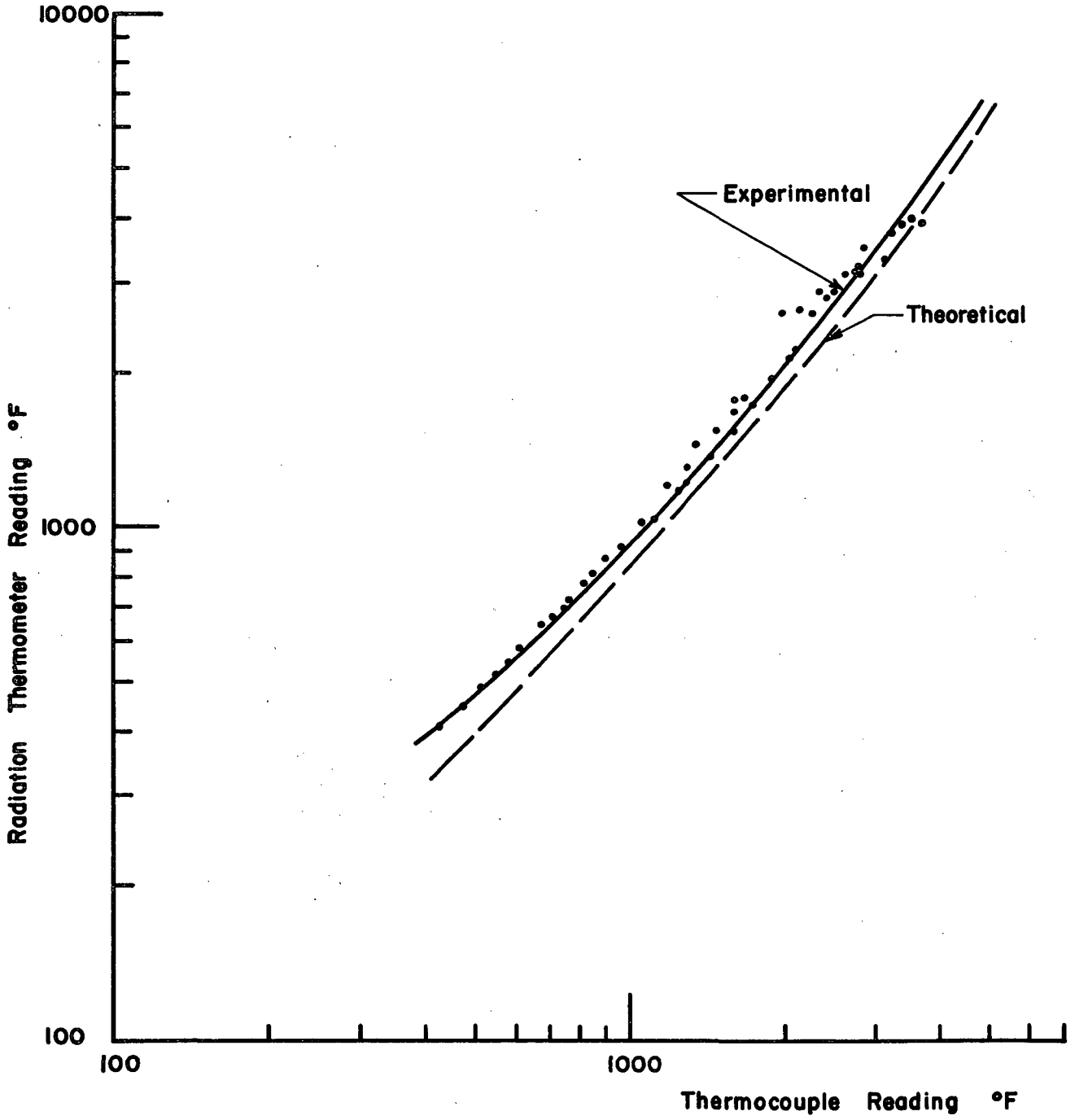

FIG. 26 COMPARISON OF THE RADIATION THERMOMETER READING TO A THERMOCOUPLE FOR A HEATED POLISHED PIECE OF TUNGSTEN

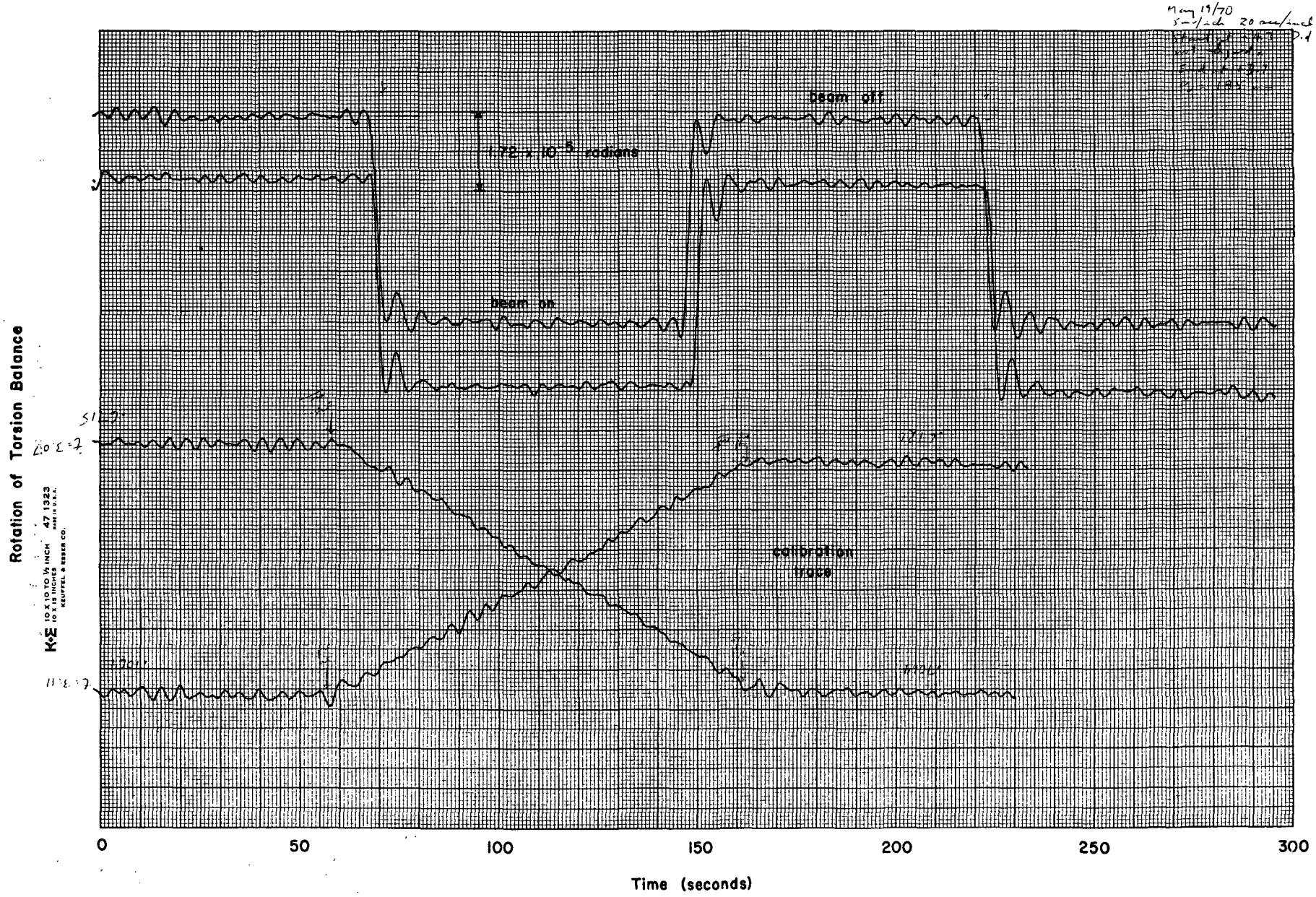

FIG. 27 OUTPUT OF OPTICAL LEVER FOR A TORSION BALANCE FORCE MEASUREMENT AND A CALIBRATION TRACE

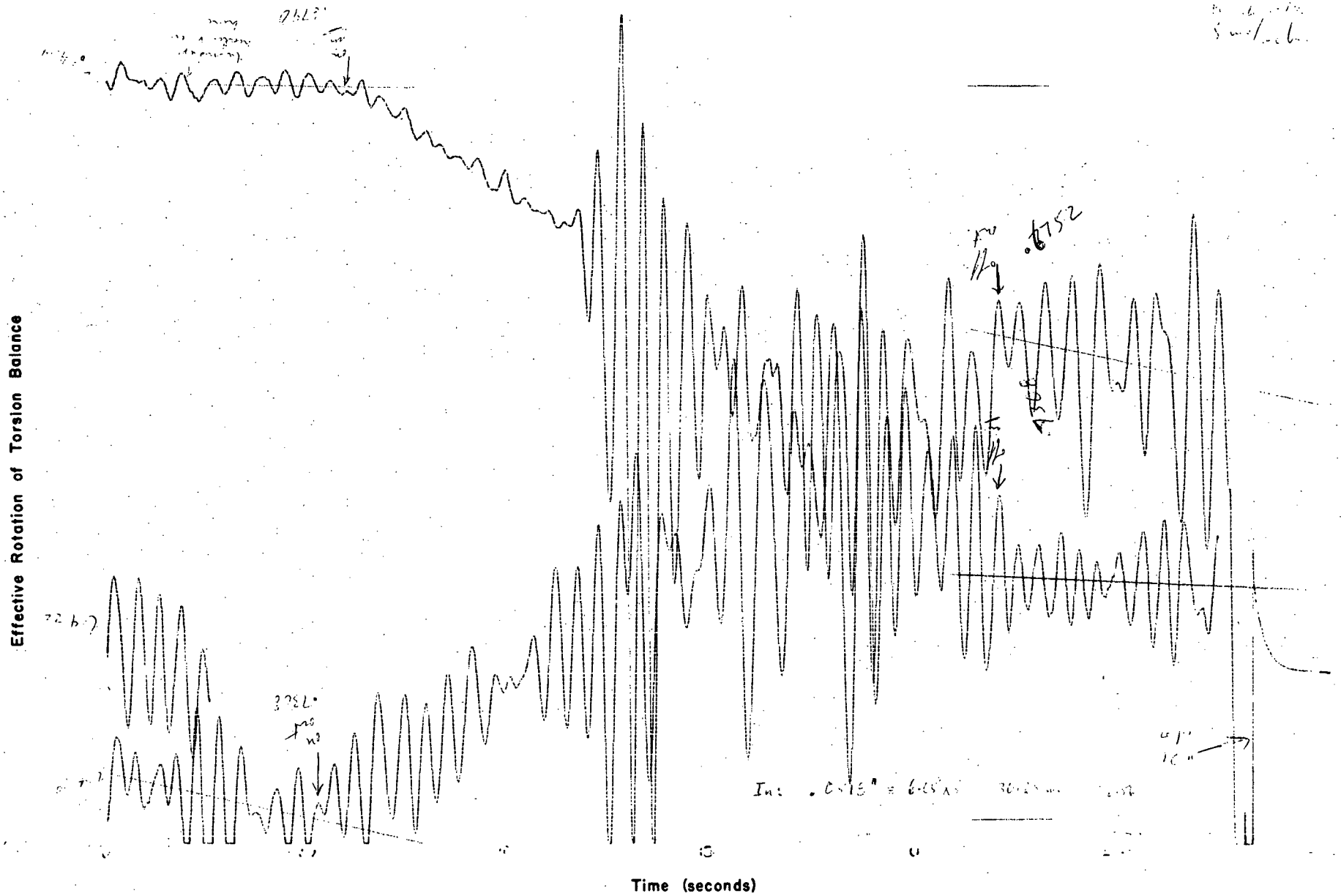

FIG. 28 PLOT OF AN ATTEMPTED CALIBRATION TRACE SHOWING THE EFFECTS OF AN EARTHQUAKE

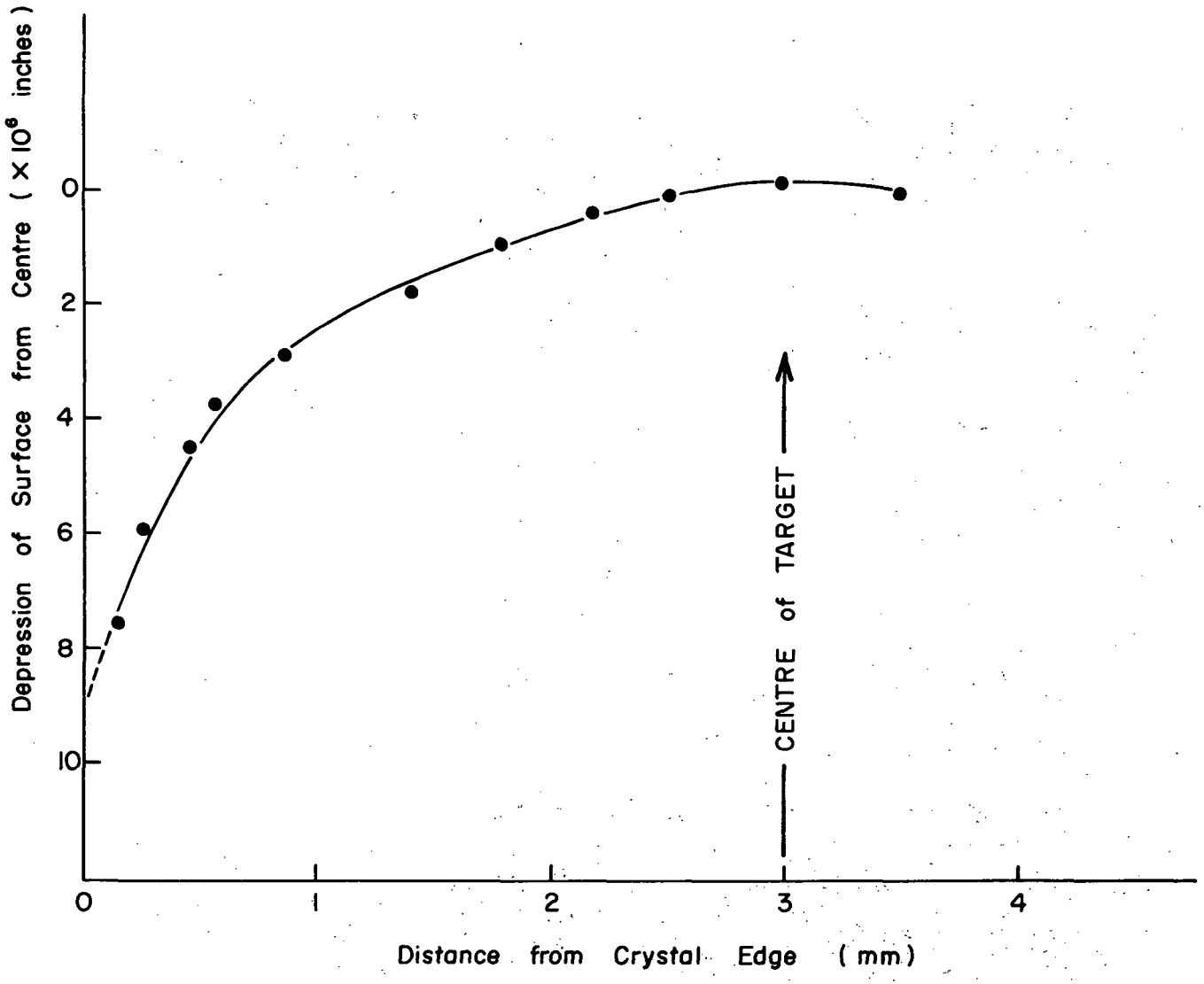

FIG. 29 SURFACE CONTOUR OF W (100) CRYSTAL

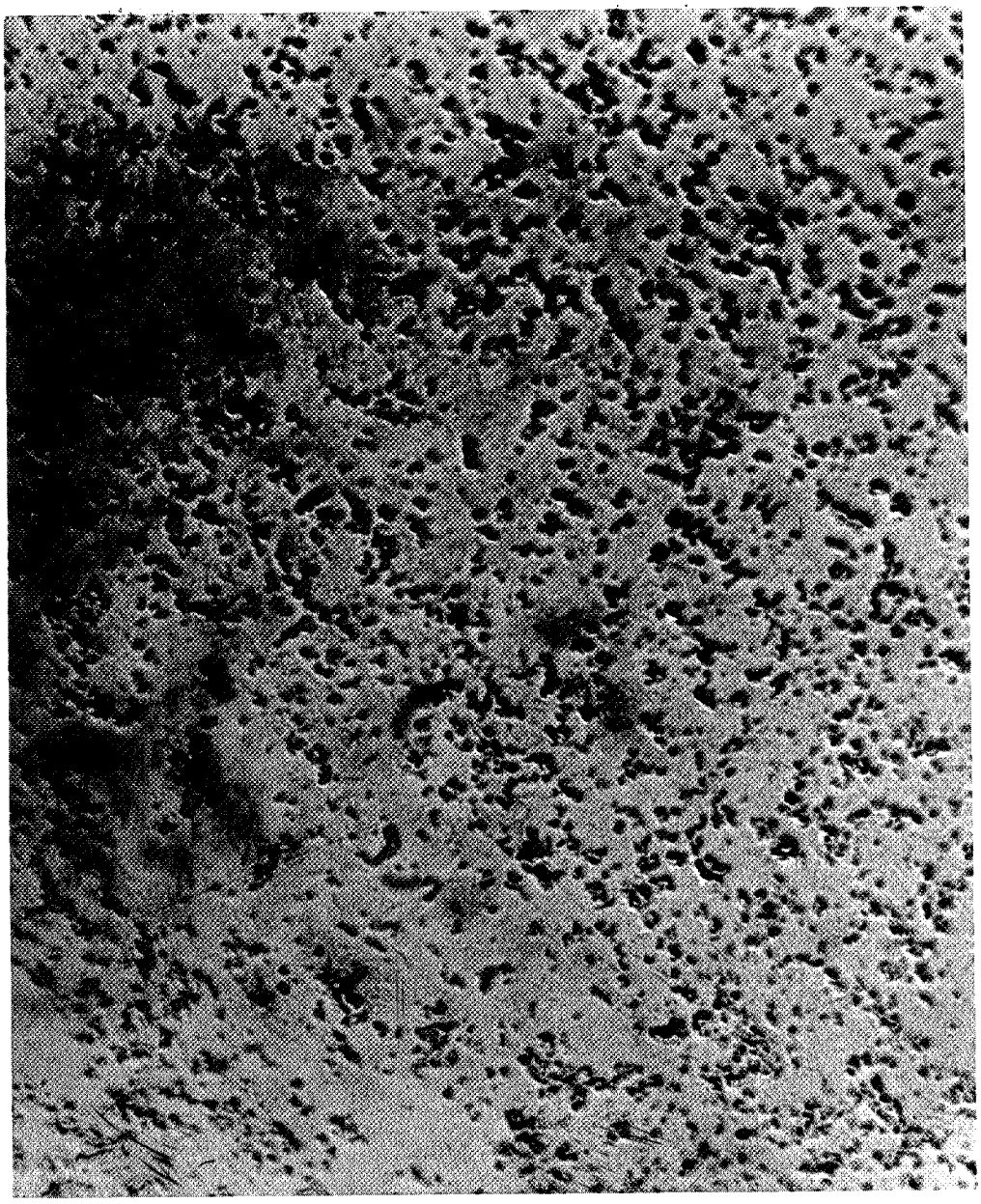

FIG. 30 500X MICROPHOTO OF MECHANICALLY POLISHED POLYCRYSTALLINE SAMPLE (NOT HEATED)

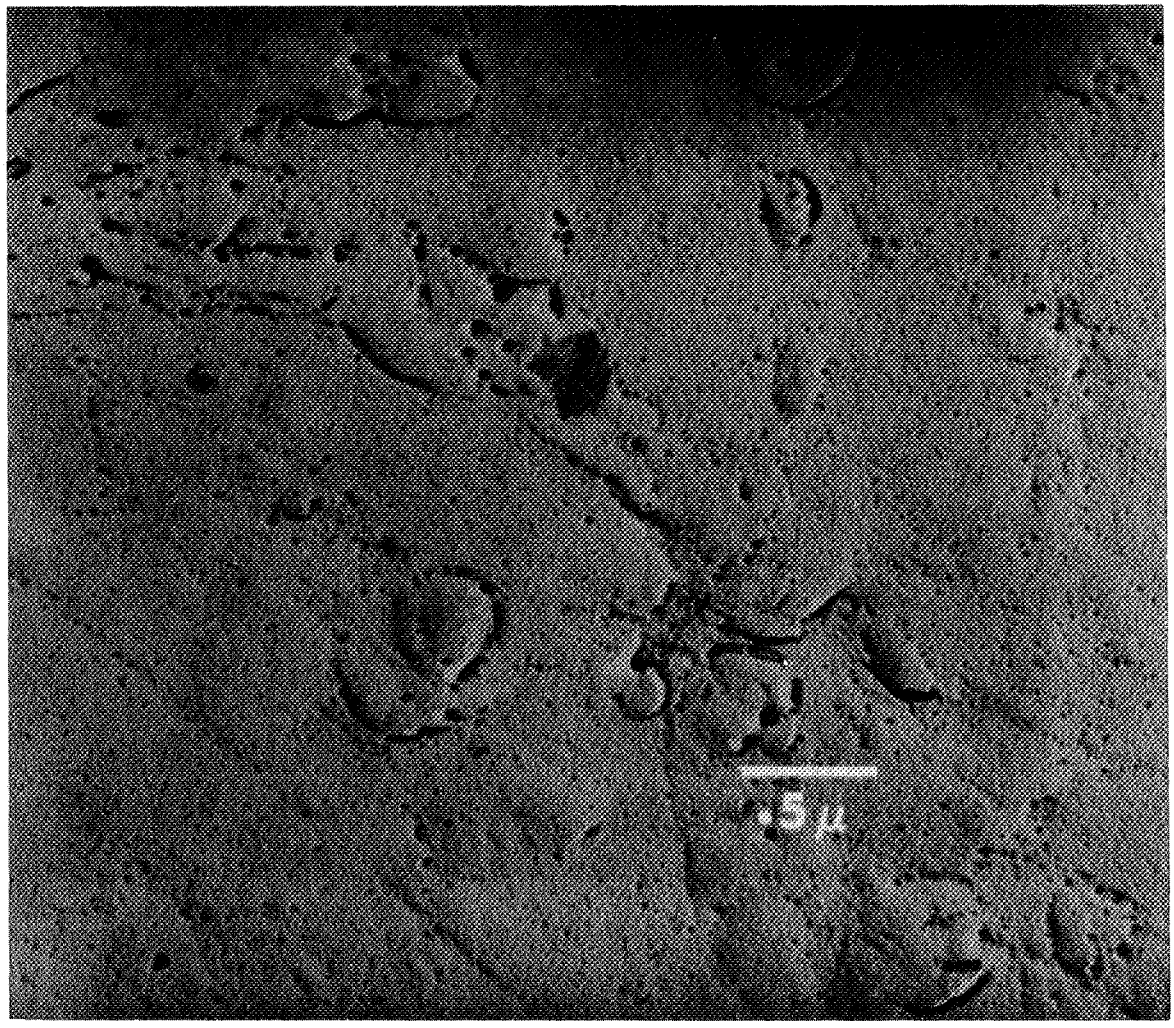

FIG. 31 ELECTRON MICROPHOTO OF A MECHANICALLY POLISHED POLYCRYSTALLINE SAMPLE (NOT HEATED)

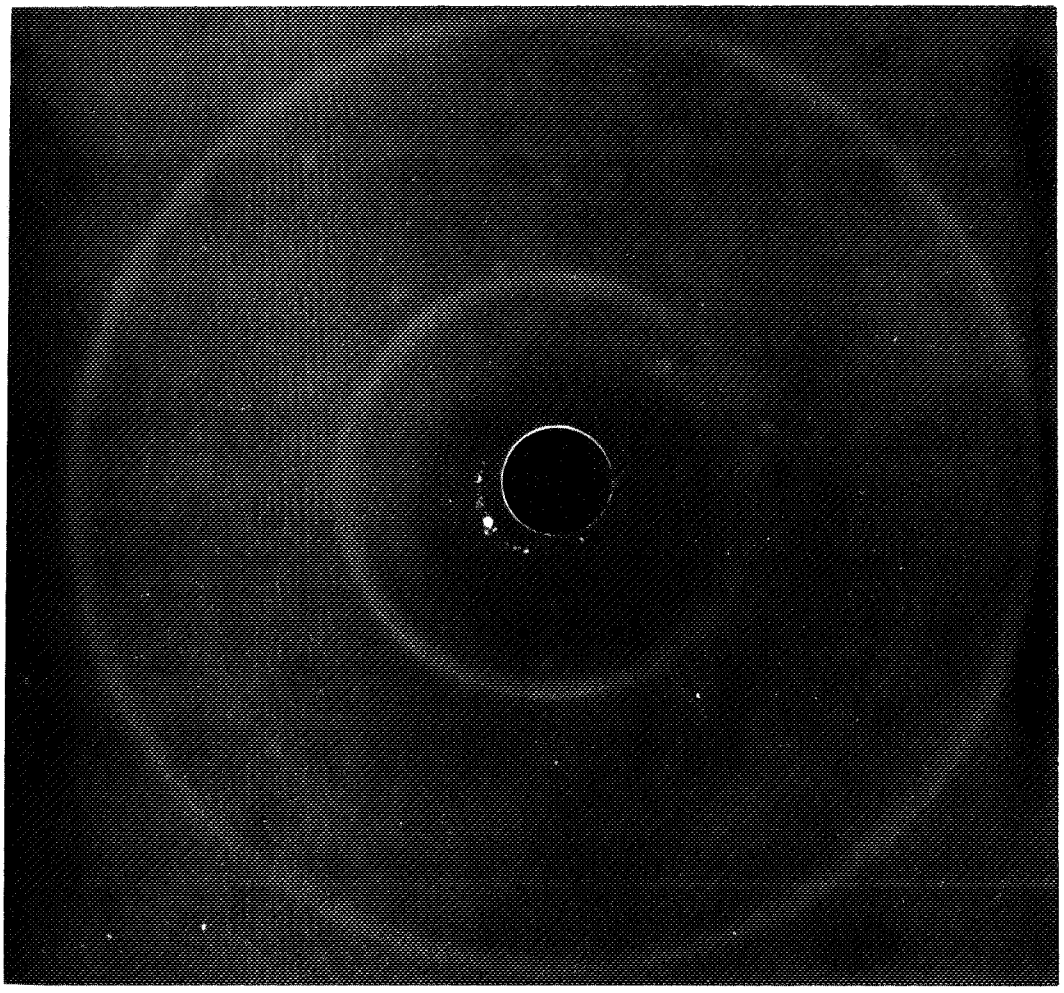

FIG. 32 X-RAY DIFFRACTION PATTERN FROM A MECHANICALLY POLISHED POLYCRYSTALLINE SAMPLE (NOT HEAT TREATED)

FIG. 33 500 X MICROPHOTO OF MECHANICALLY POLISHED POLYCRYSTALLINE SAMPLE AFTER 5 MINUTES OF HEATING AT 2000°C IN A VACUUM

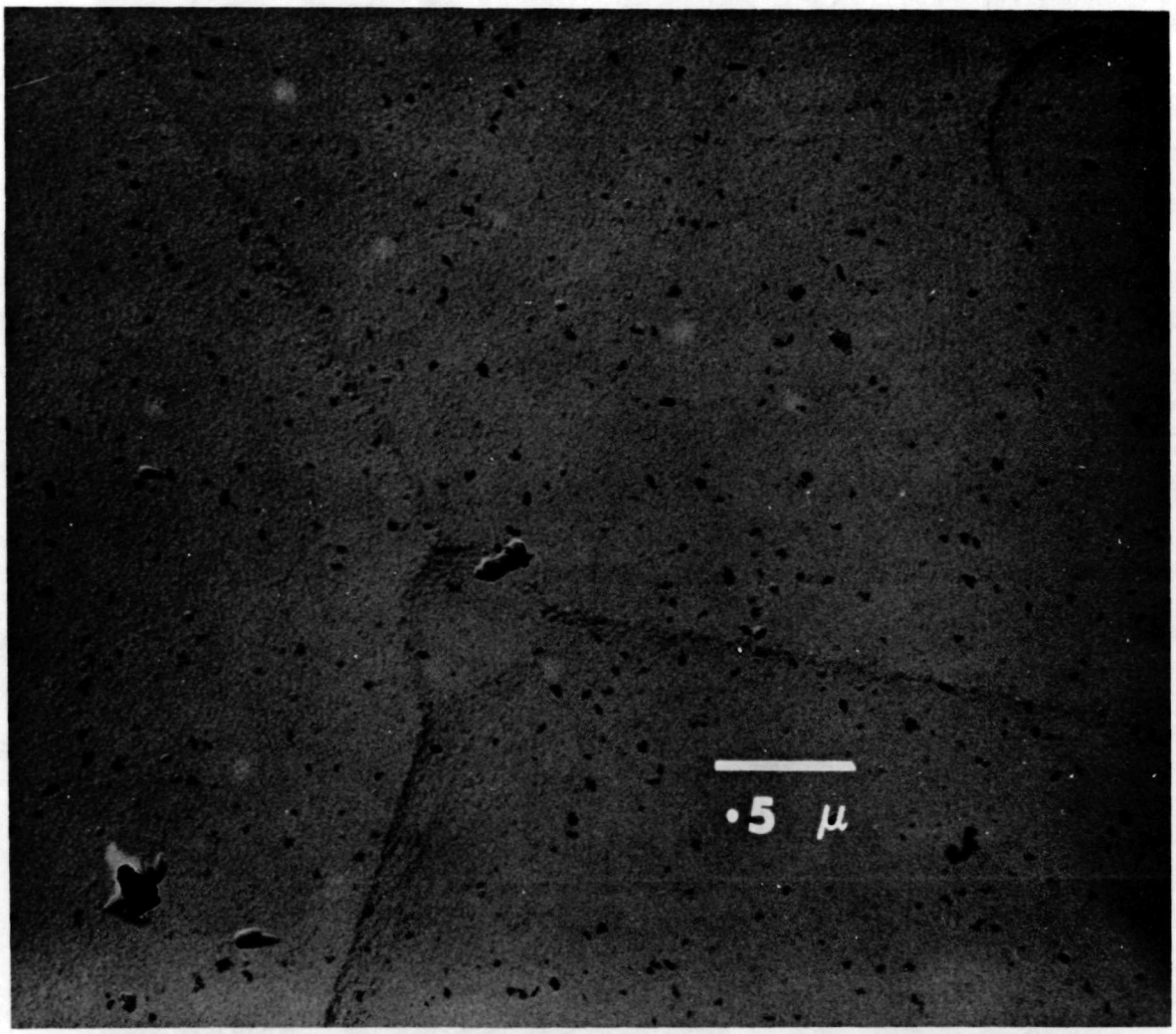

FIG. 34 ELECTRON MICROPHOTO OF A MECHANICALLY POLISHED POLYCRYSTALLINE SAMPLE AFTER FIVE MINUTES OF HEATING AT 2000°C IN A VACUUM

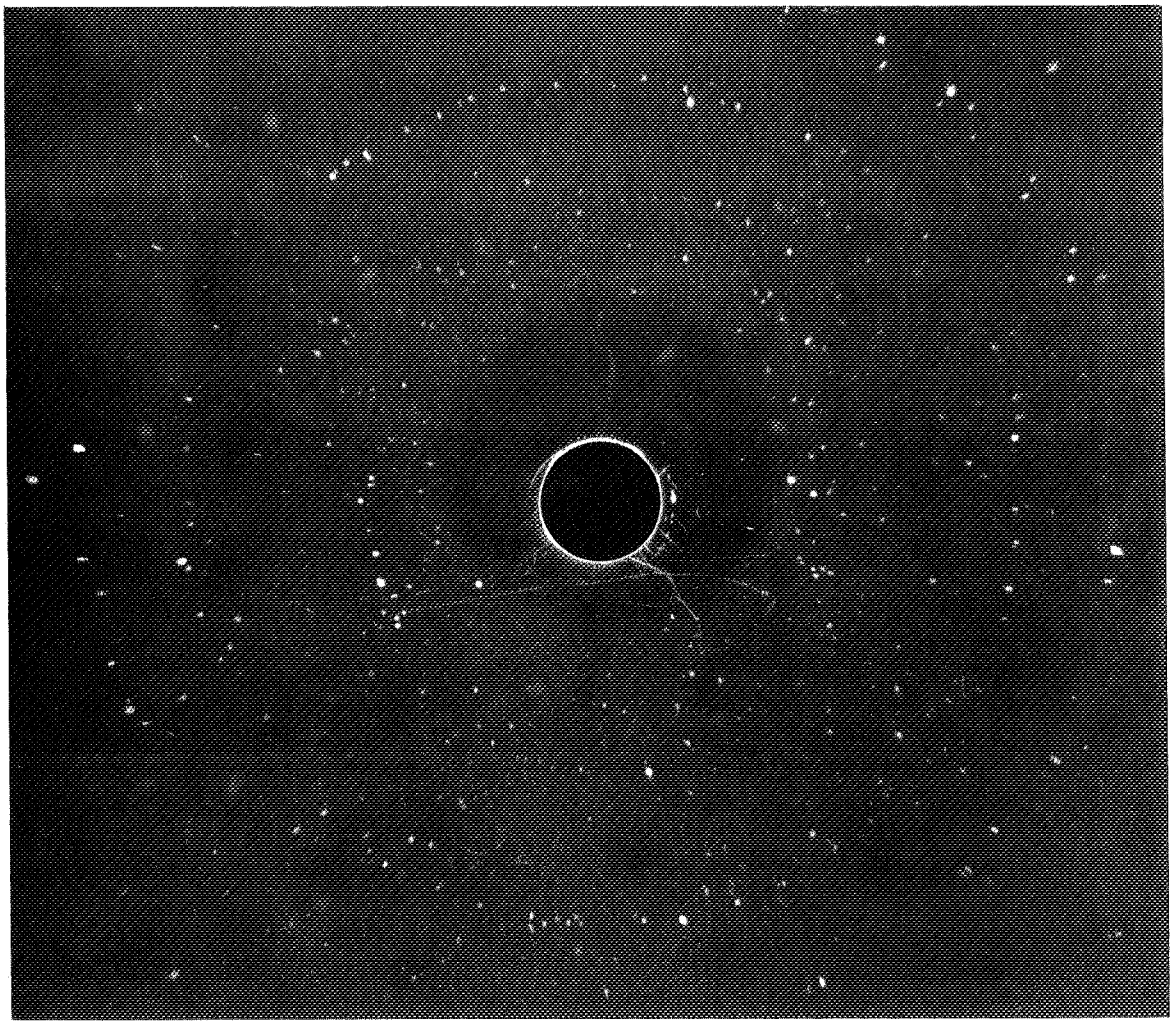

FIG. 35 X-RAY DIFFRACTION PATTERN FROM A MECHANICALLY POLISHED POLYCRYSTALLINE SAMPLE AFTER FIVE MINUTES OF HEATING AT 2000°C IN A VACUUM

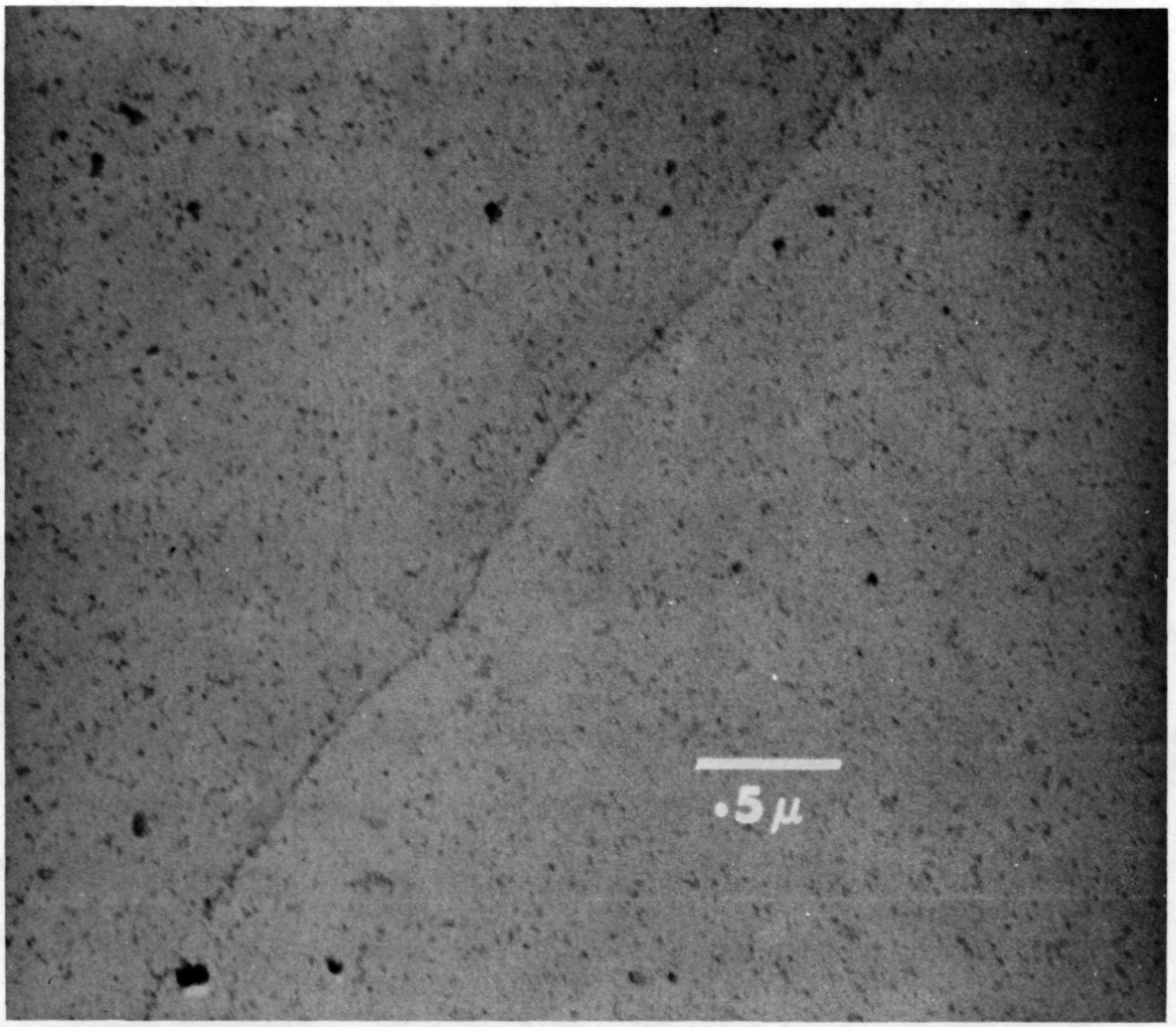

FIG. 36 ELECTRON MICROPHOTO OF A MECHANICALLY POLISHED W(100) SINGLE CRYSTAL SAMPLE AFTER ANNEALING IN A VACUUM

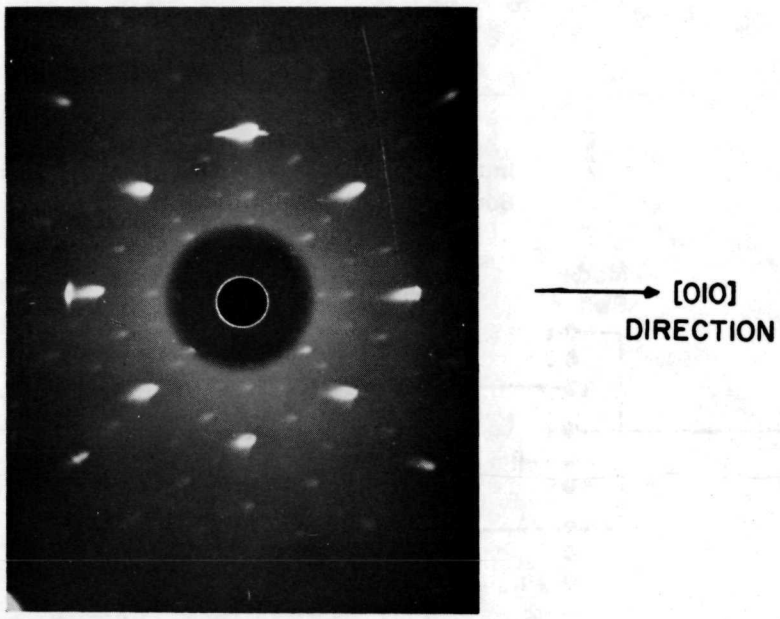

FIG. 37 X-RAY DIFFRACTION PATTERN FROM A W(100) TARGET BEFORE ANNEALING IN A VACUUM

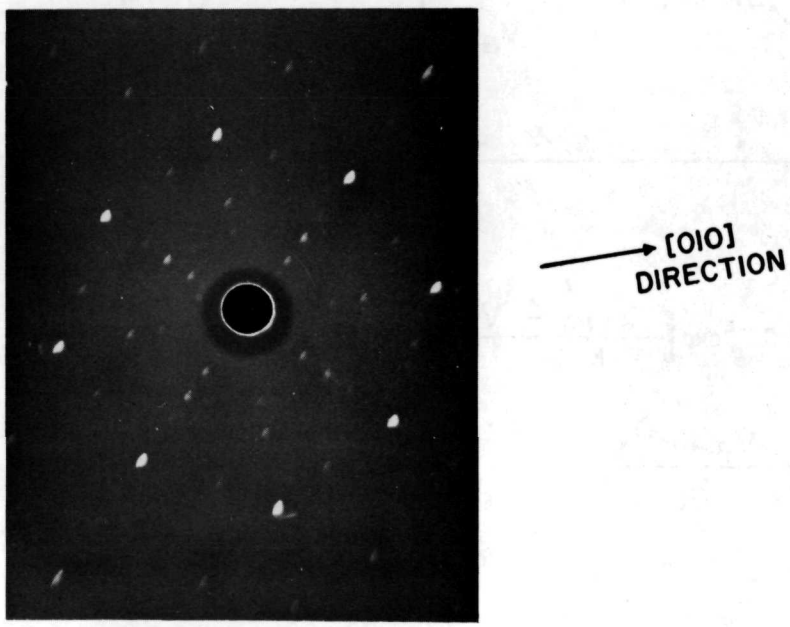

FIG. 38 X-RAY DIFFRACTION PATTERN FROM A W(100) TARGET AFTER ANNEALING IN A VACUUM

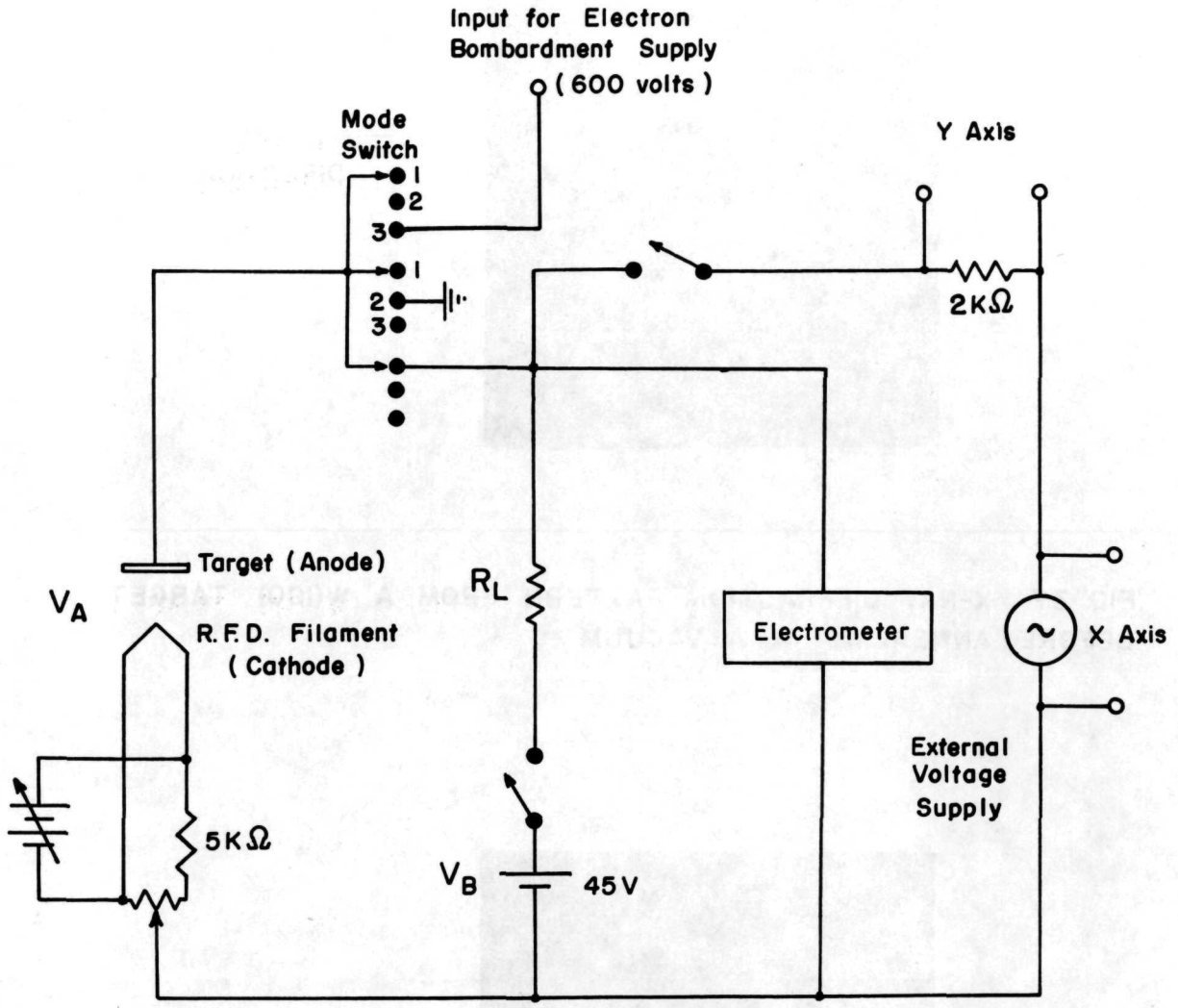

$$I_A = C\,T_e^2 \exp\left[\frac{-e\,(\phi_A - V_A)}{k\,T_e}\right]$$

$$I_A = \frac{V_B - V_A}{R_L} \qquad \text{if} \quad k\,T_e \ll e\,(V_B - V_A)$$

$$\text{then} \qquad \Delta\phi_A = \Delta V_A$$

FIG. 39 RETARDING FIELD DIODE CIRCUIT

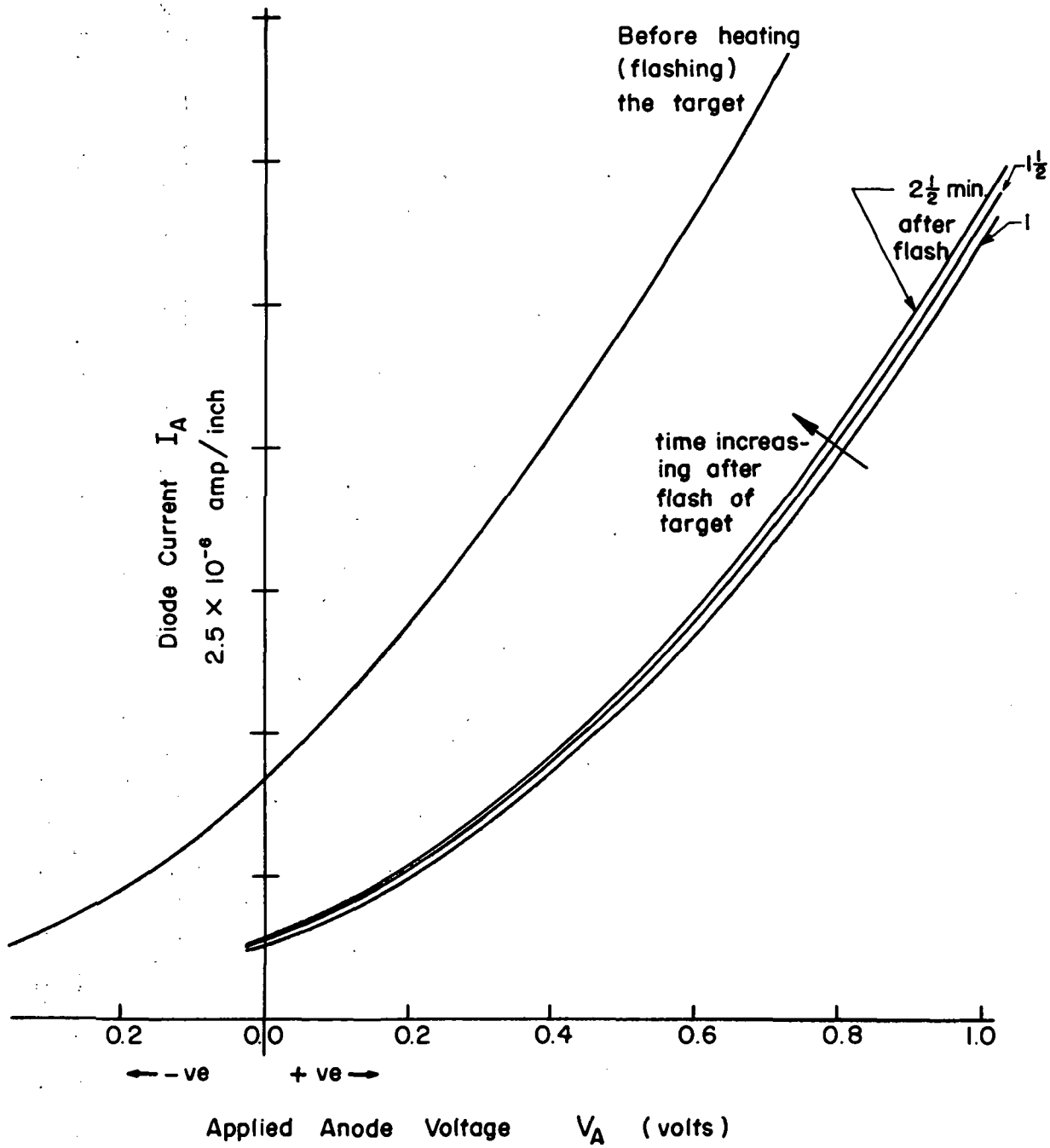

FIG. 40 RETARDING FIELD DIODE CURRENT - VOLTAGE CHARACTERISTICS

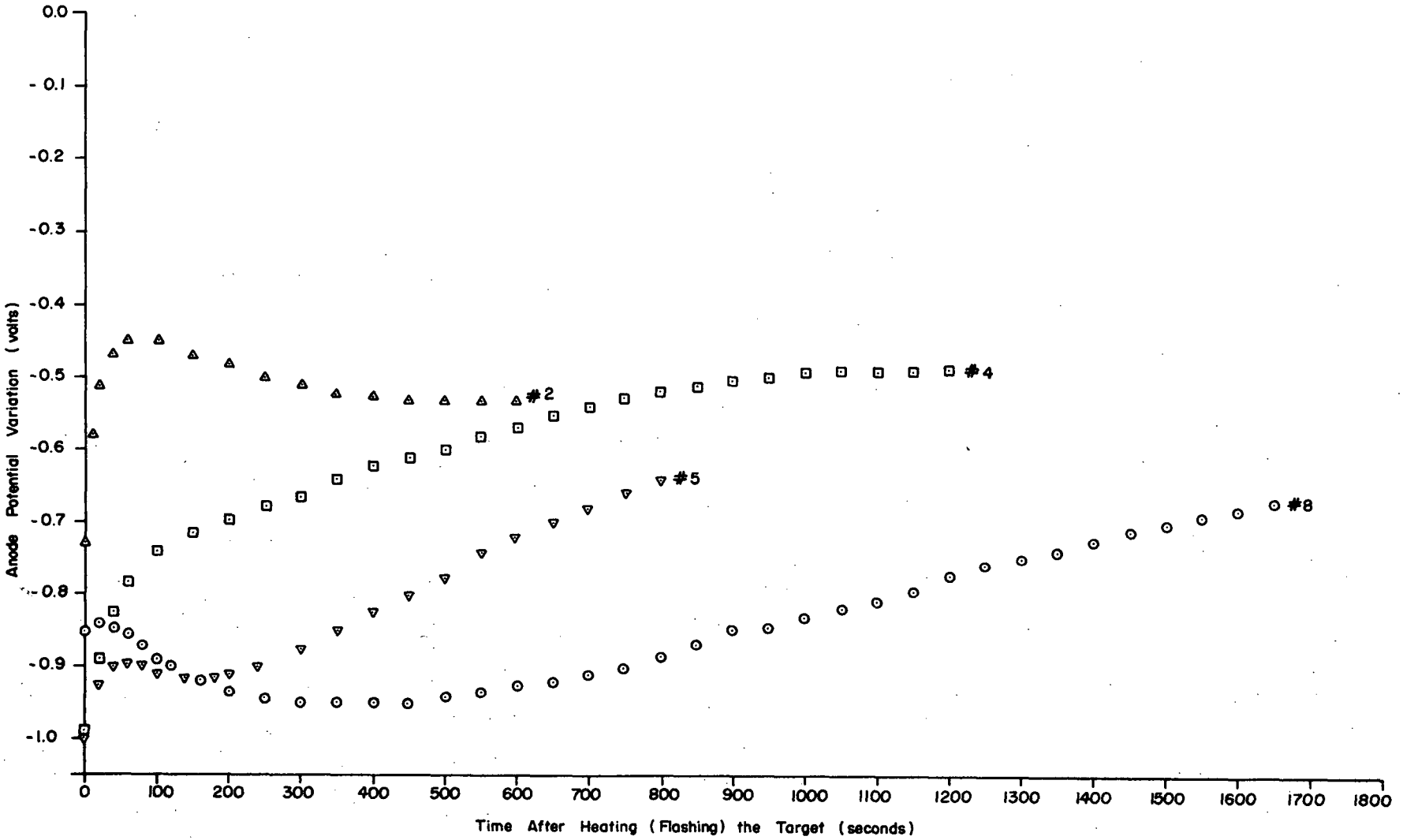

FIG. 41 (100) TUNGSTEN TARGET (ANODE) SURFACE POTENTIAL VARIATION AFTER REPEATED FLASHES WITH A FALLING PRESSURE TARGET HAD BEEN EXPOSED TO ATMOSPHERIC AIR.

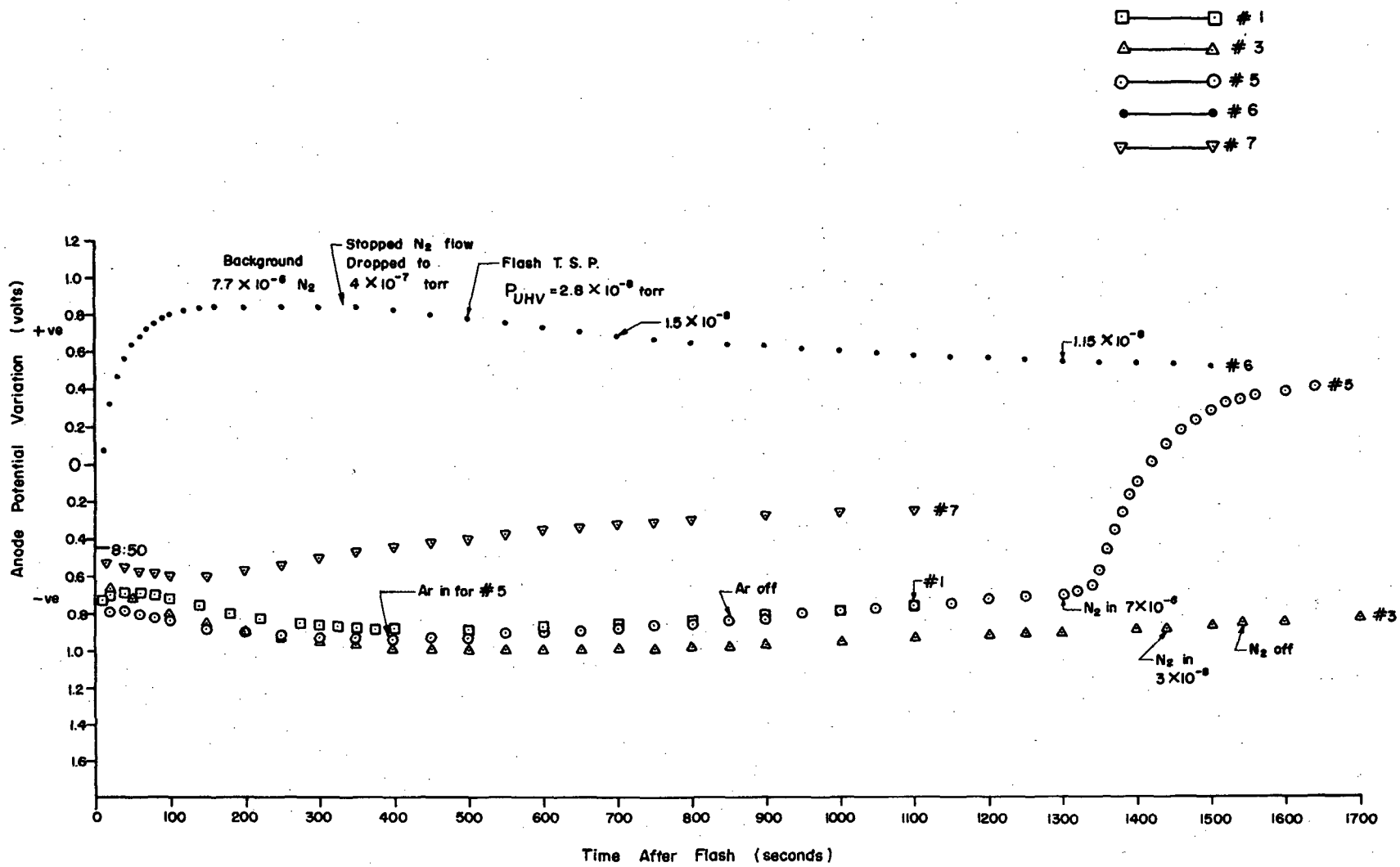

FIG. 42 (100) TUNSTEN TARGET SURFACE POTENTIAL VARIATION WITH SURFACE EXPOSED TO VARIOUS BACKGROUND GAS CONDITIONS AFTER FLASHING

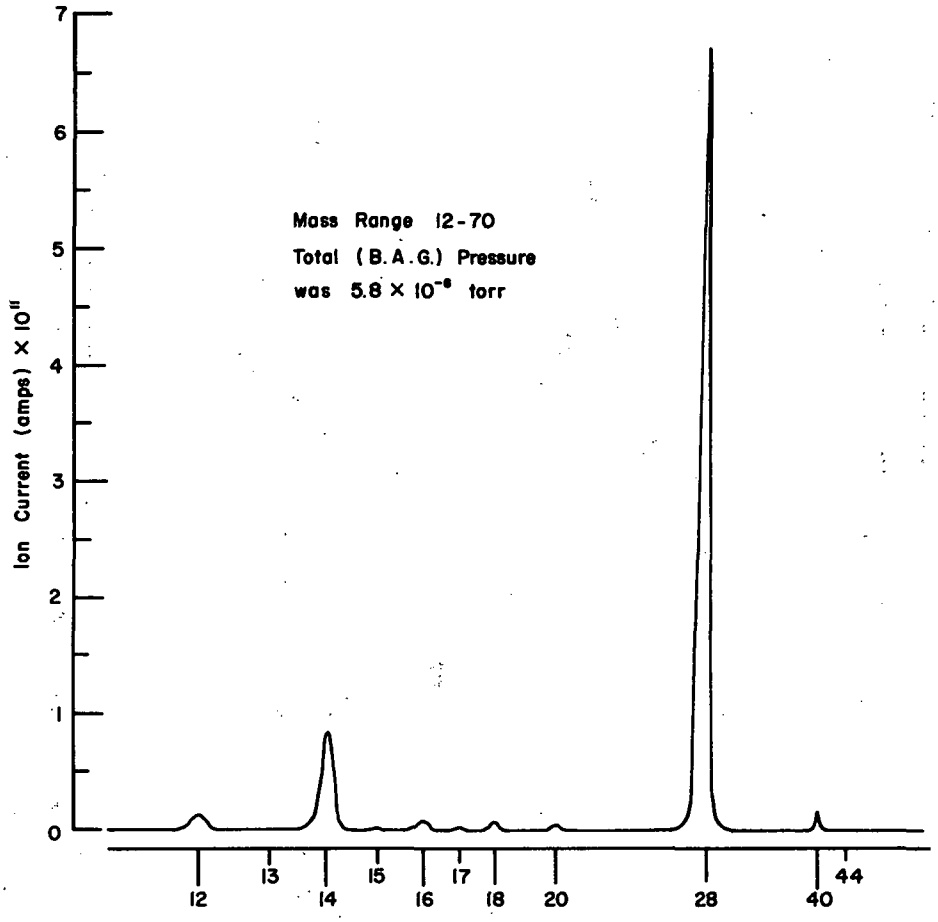

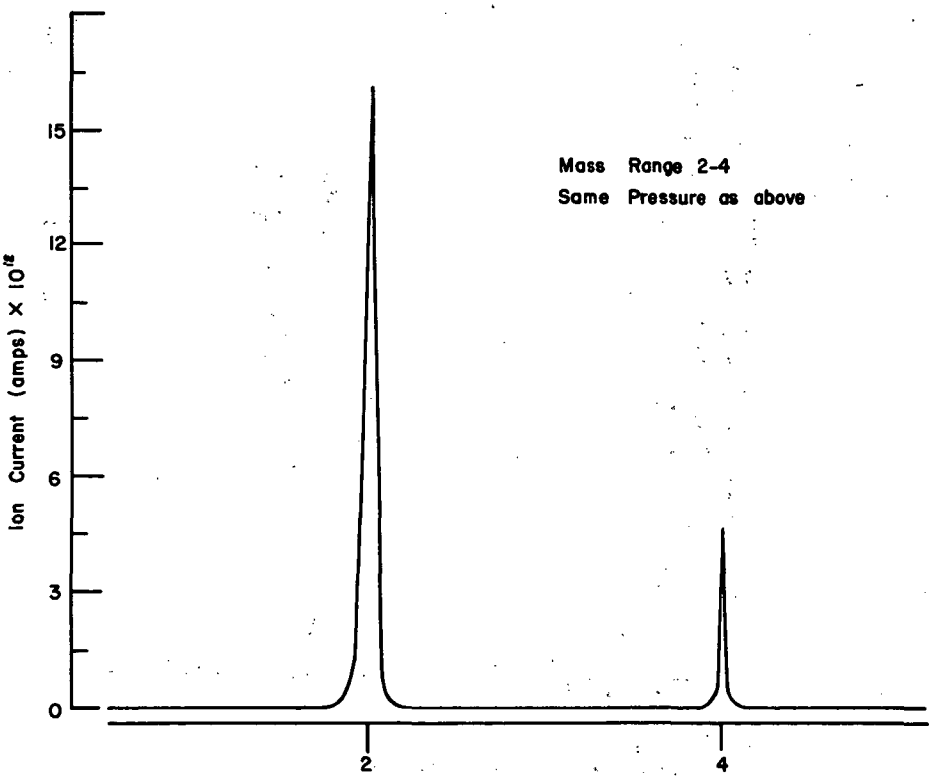

FIG. 43 MASS SPECTROMETER READING OF GASES IN UHV CHAMBER ON ADMITTING THE GAS N_2 UNTIL $P = 5.8 \times 10^{-8}$ torr (B.A.G.)

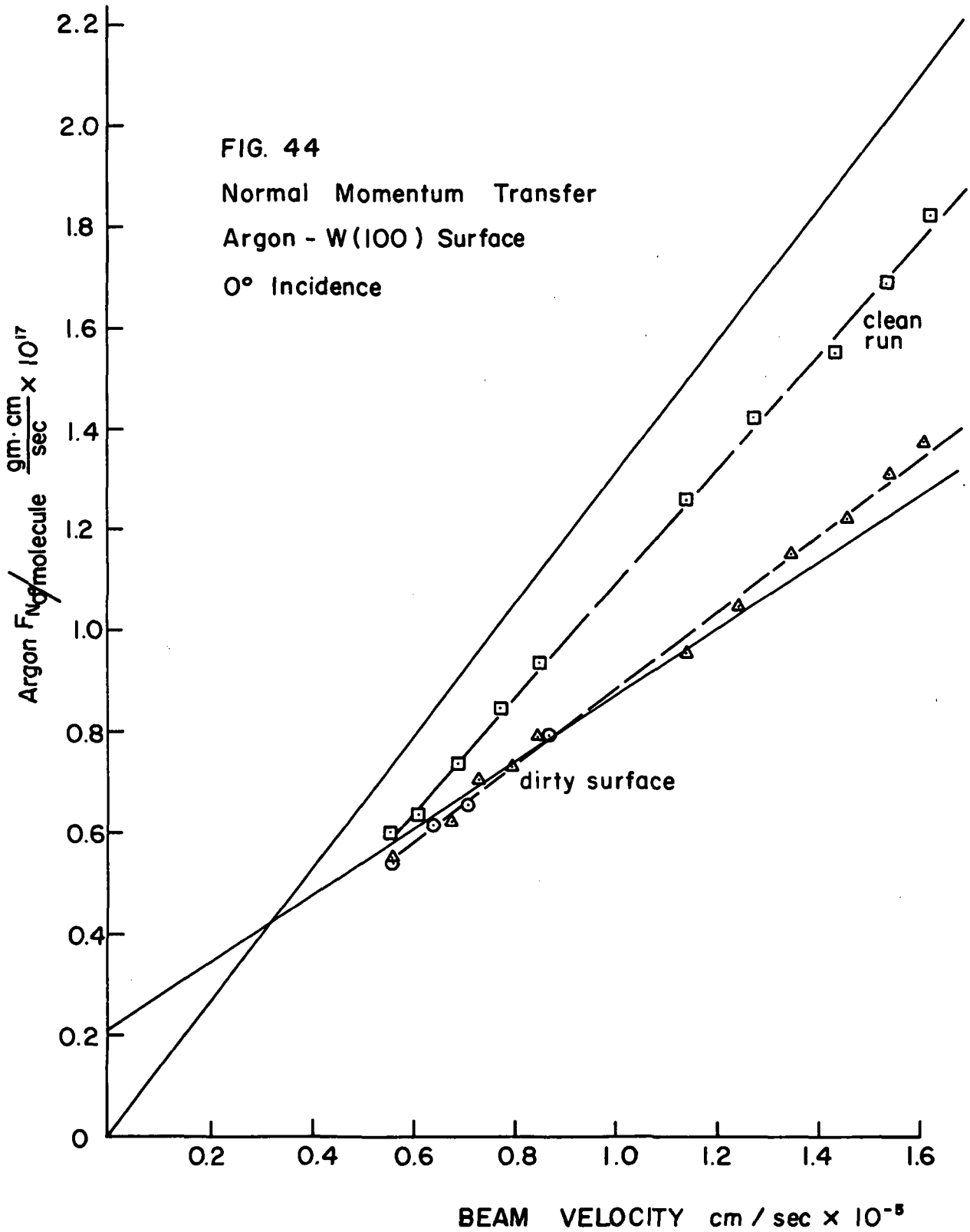
FIG. 44
Normal Momentum Transfer
Argon - W(100) Surface
0° Incidence
clean run
dirty surface
Argon F_N gm/molecule $\frac{gm \cdot cm}{sec} \times 10^{17}$
BEAM VELOCITY cm / sec $\times 10^{-5}$
2.2
2.0
1.8
1.6
1.4
1.2
1.0
0.8
0.6
0.4
0.2
0
0.2
0.4
0.6
0.8
1.0
1.2
1.4
1.6

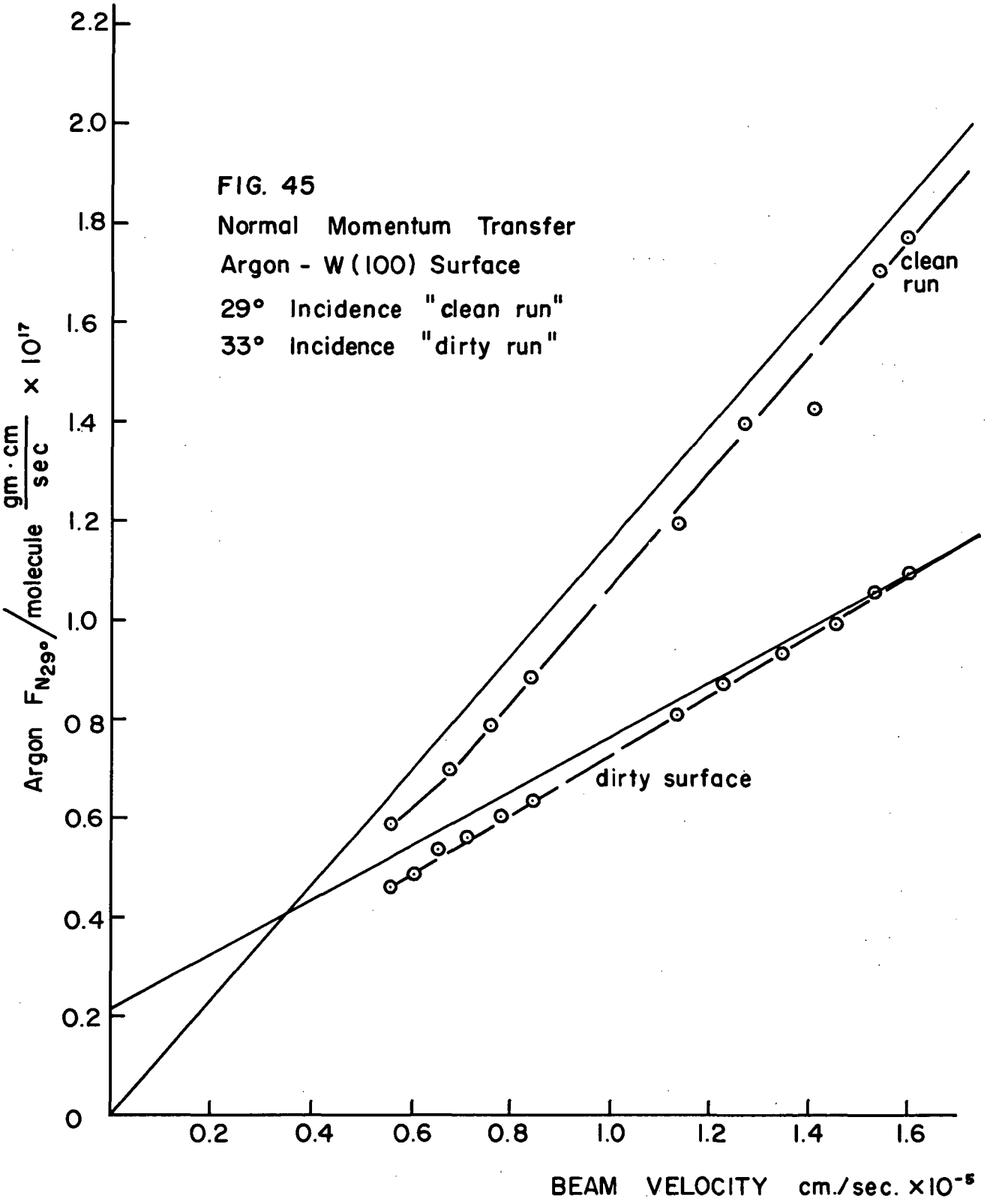
FIG. 45
Normal Momentum Transfer
Argon - W(100) Surface
29° Incidence "clean run"
33° Incidence "dirty run"
clean run
dirty surface
Argon $F_{N29°}$ / molecule $\frac{gm \cdot cm}{sec} \times 10^{17}$
BEAM VELOCITY cm./sec. $\times 10^{-5}$
0
0.2
0.4
0.6
0.8
1.0
1.2
1.4
1.6
1.8
2.0
2.2

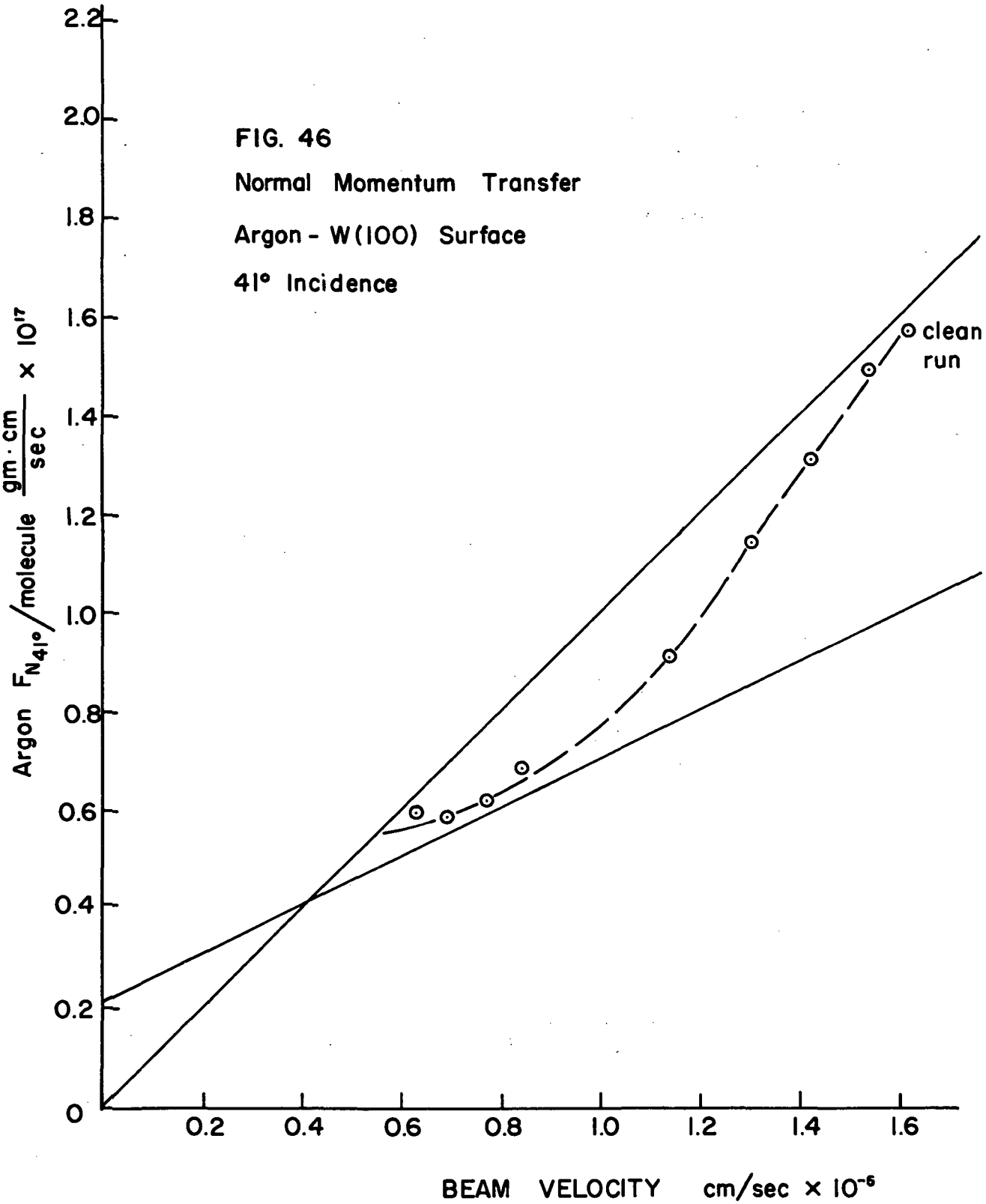
FIG. 46
Normal Momentum Transfer
Argon - W(100) Surface
41° Incidence
clean run
Argon $F_{N41°}$/molecule $\frac{gm \cdot cm}{sec} \times 10^{17}$
BEAM VELOCITY cm/sec $\times 10^{-5}$
0
0.2
0.4
0.6
0.8
1.0
1.2
1.4
1.6
1.8
2.0
2.2

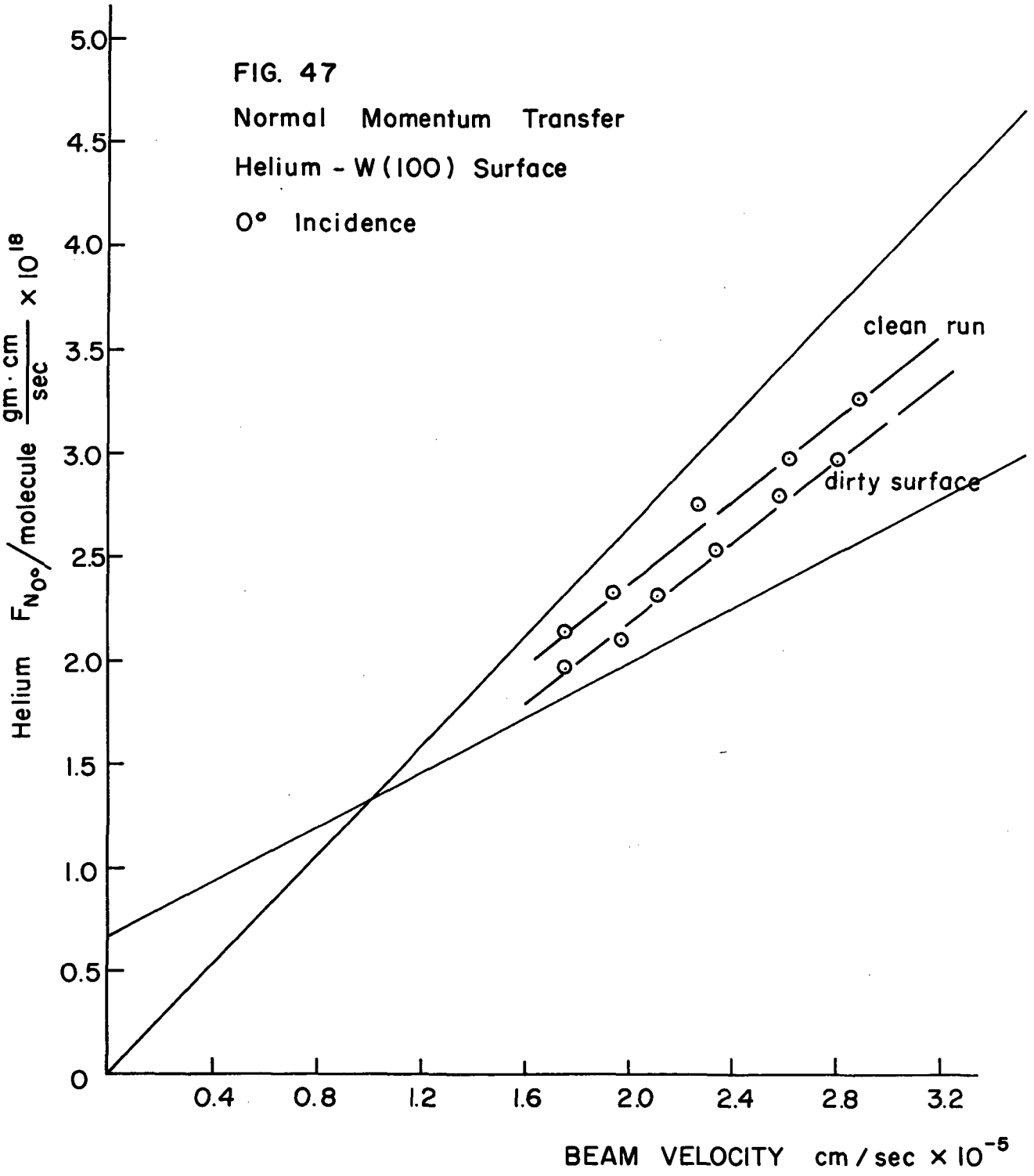
FIG. 47
Normal Momentum Transfer
Helium - W(100) Surface
0° Incidence
clean run
dirty surface
Helium $F_{N0°}$/molecule $\frac{gm \cdot cm}{sec} \times 10^{18}$
5.0
4.5
4.0
3.5
3.0
2.5
2.0
1.5
1.0
0.5
0
0.4
0.8
1.2
1.6
2.0
2.4
2.8
3.2
BEAM VELOCITY cm / sec $\times 10^{-5}$

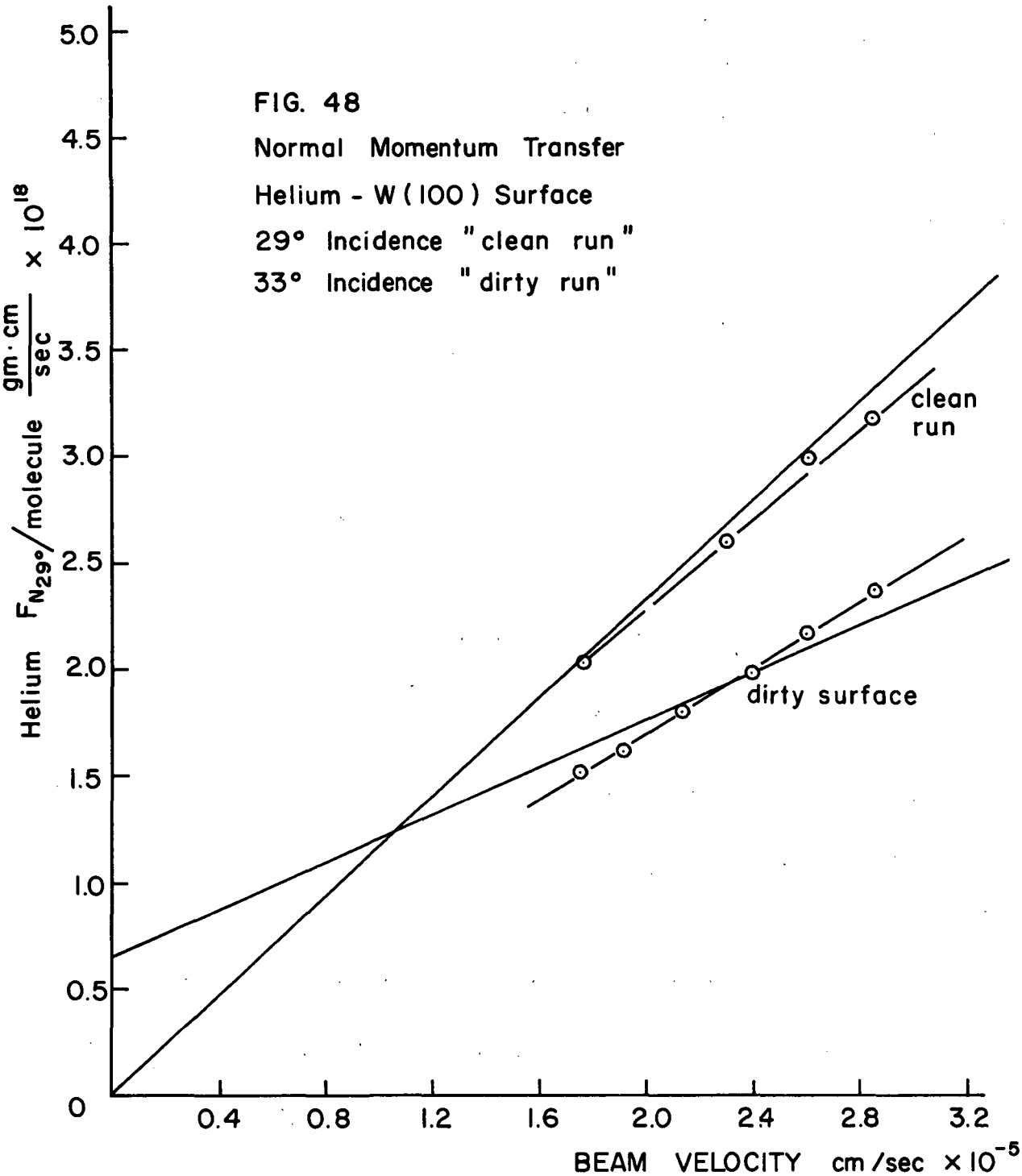
FIG. 48
Normal Momentum Transfer
Helium - W (100) Surface
29° Incidence "clean run"
33° Incidence "dirty run"
clean run
dirty surface
Helium $F_{N29°}$/molecule $\frac{gm \cdot cm}{sec} \times 10^{18}$
BEAM VELOCITY cm/sec $\times 10^{-5}$
5.0
4.5
4.0
3.5
3.0
2.5
2.0
1.5
1.0
0.5
0
0.4
0.8
1.2
1.6
2.0
2.4
2.8
3.2

FIG. 49

Normal Momentum Transfer

Helium - W (100) Surface

41° Incidence

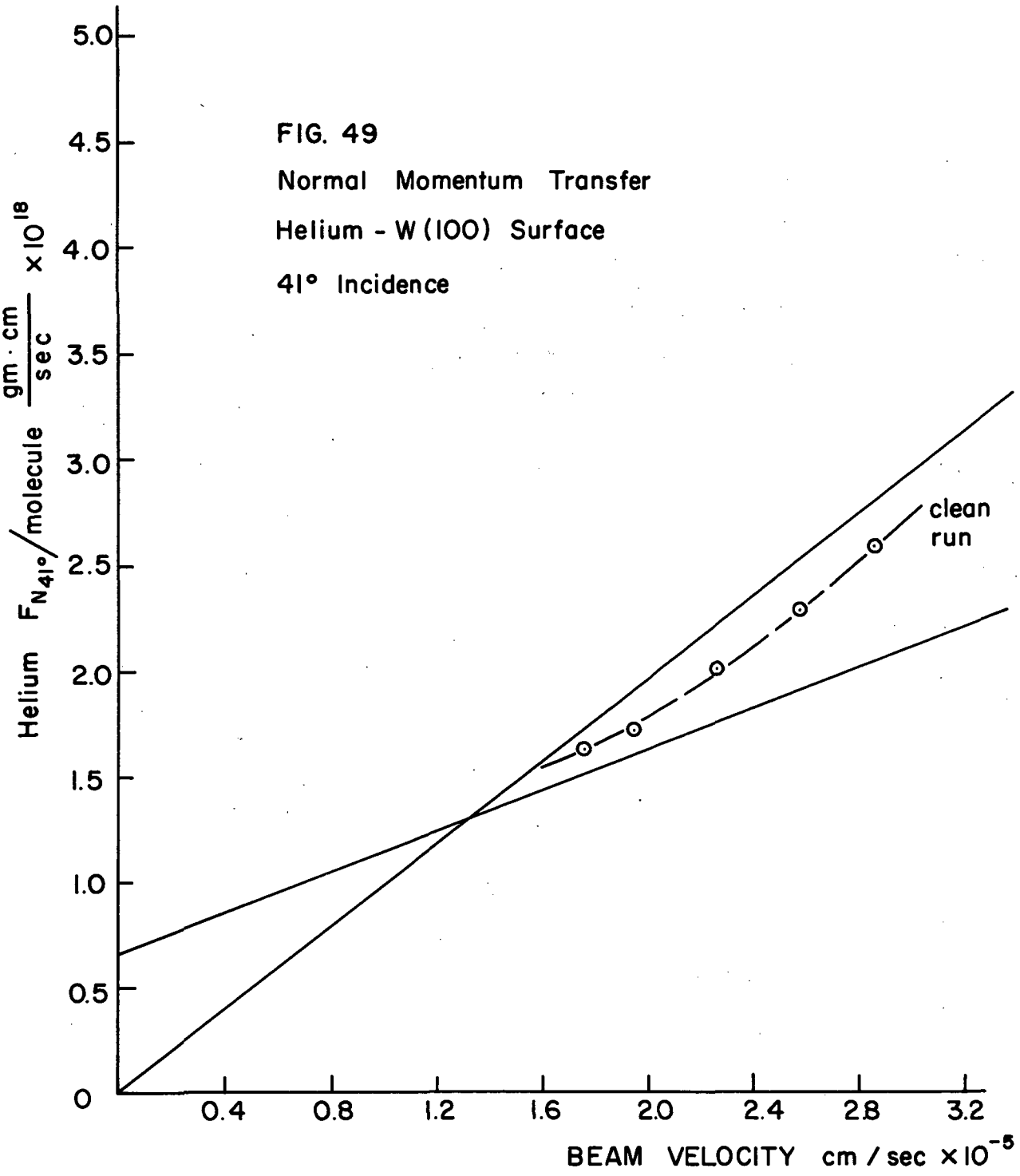

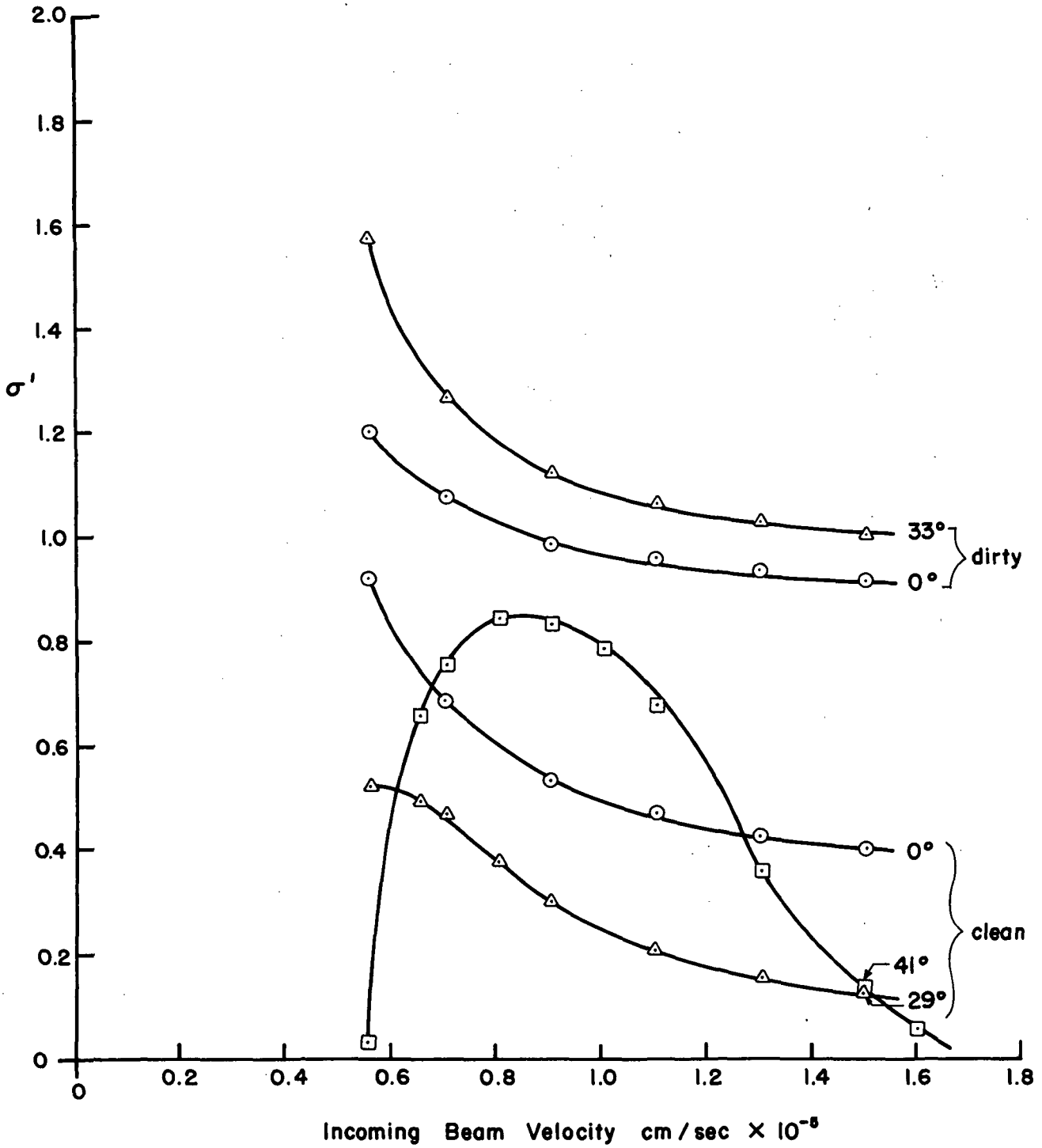

FIG. 50 PLOT OF NORMAL MOMENTUM ACCOMMODATION COEFFICIENT σ' VS. INCOMING ARGON BEAM VELOCITY FOR BOTH A CLEAN & A DIRTY TUNSTEN W(100) SURFACE

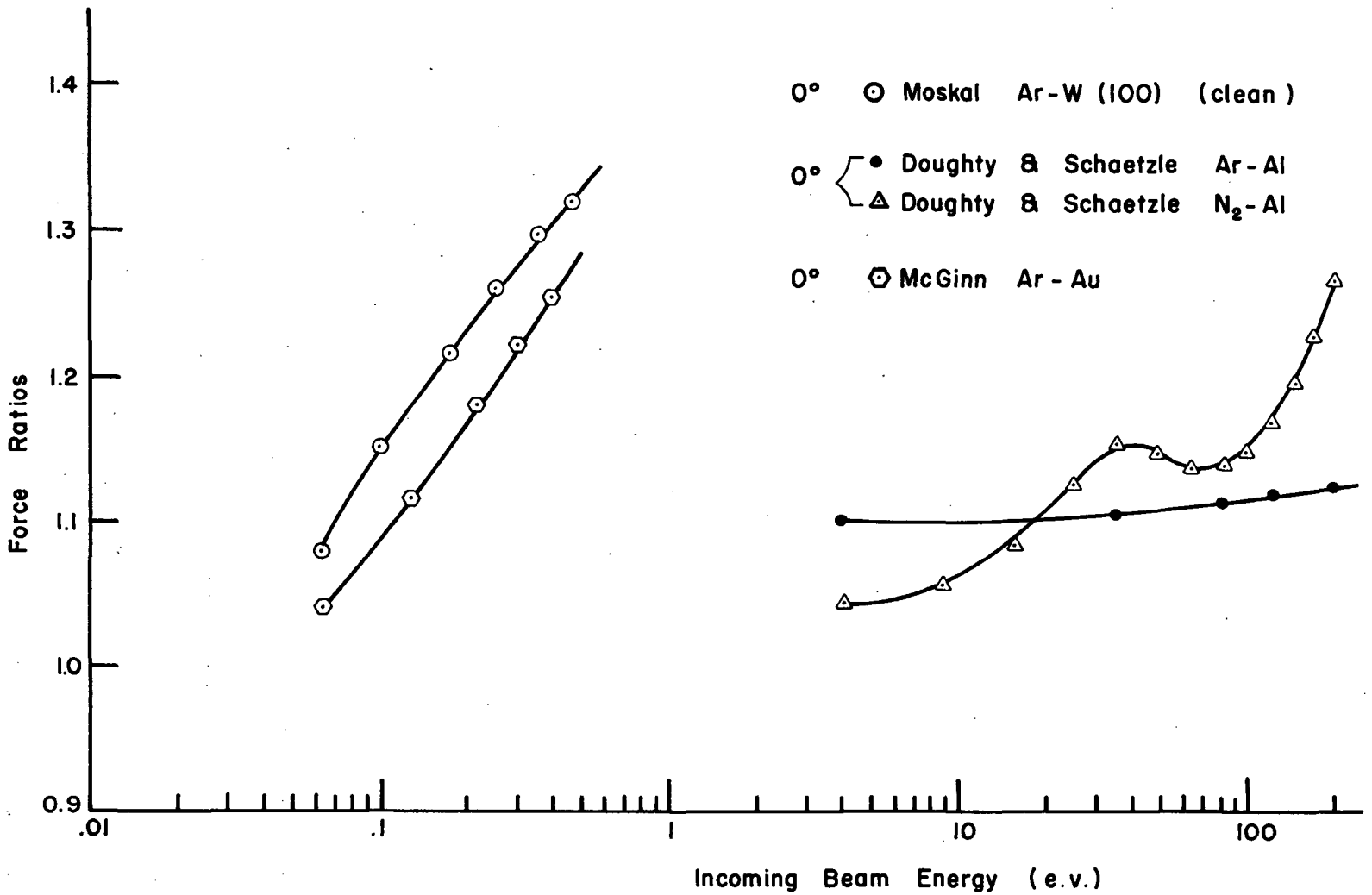

FIG. 51 COMPARISON OF THE FORCE RATIO $\frac{P_i + P_r}{P_i + P_w}$ VS INCOMING BEAM ENERGY FOR CLEAN & DIRTY OR ROUGH SURFACES FOR A NORMALLY INCIDENT BEAM OF ARGON OR N_2 PARTICLES

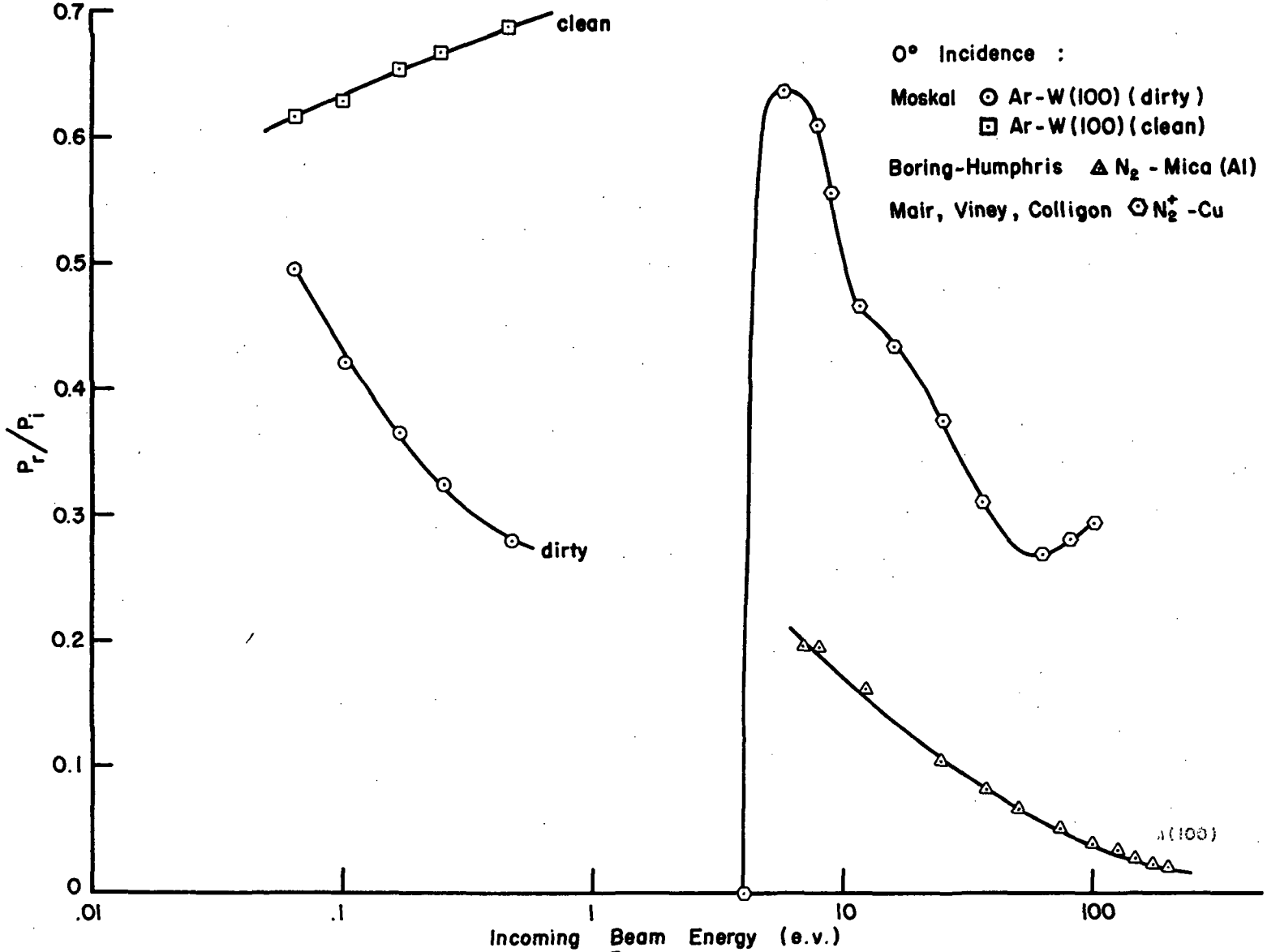

FIG. 52 COMPARISON OF THE FORCE RATIO $\frac{P_r}{P_i}$ VS INCOMING BEAM ENERGY FOR CLEAN & DIRTY OR ROUGH SURFACES FOR A NORMALLY INCIDENT BEAM OF PARTICLES

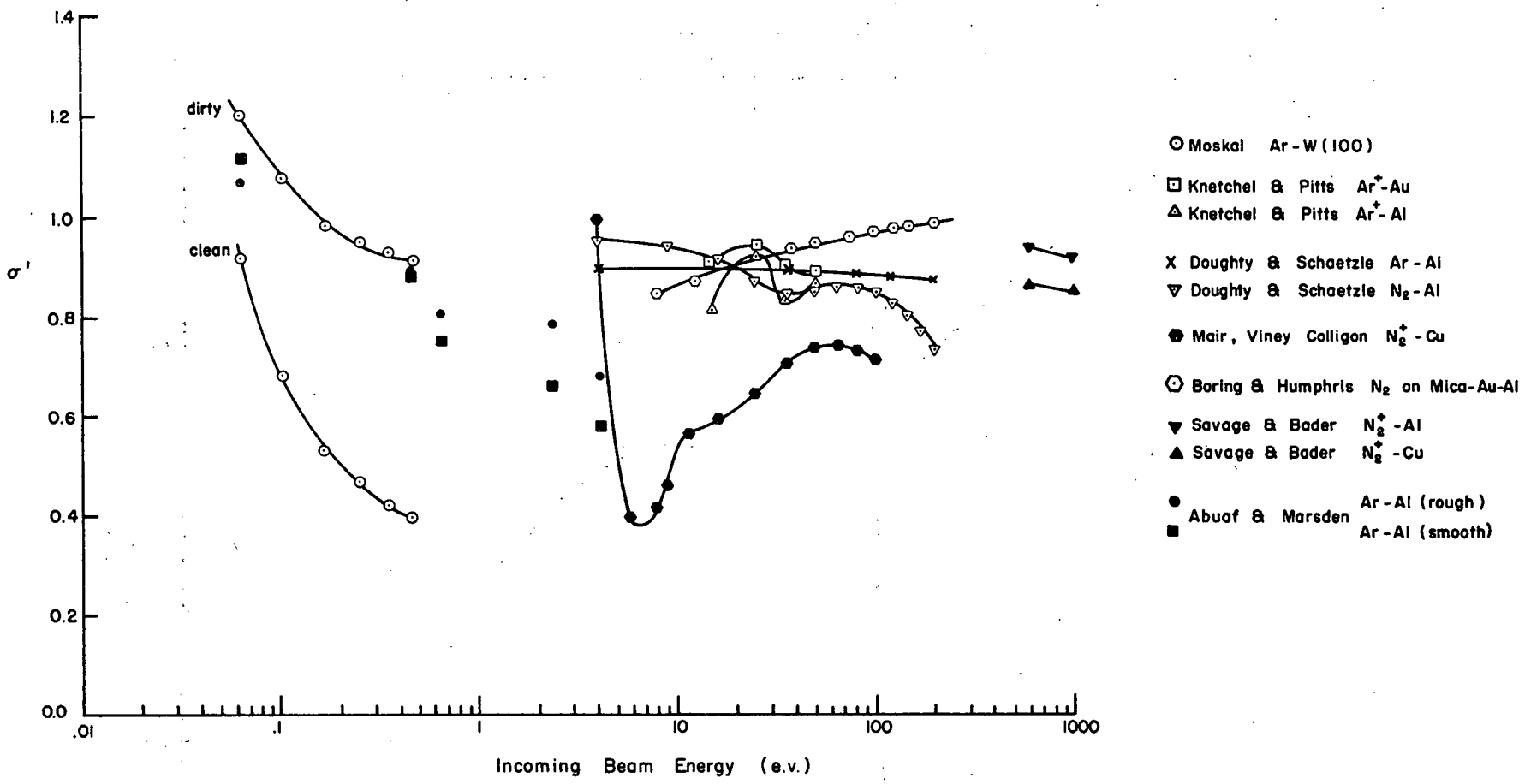

FIG. 53 COMPARISON OF NORMAL MOMENTUM ACCOMMODATION COEFFICIENTS σ' VS INCOMING BEAM ENERGY FOR VARIOUS GAS-SURFACE COMBINATIONS FOR $\theta_i = 0°$

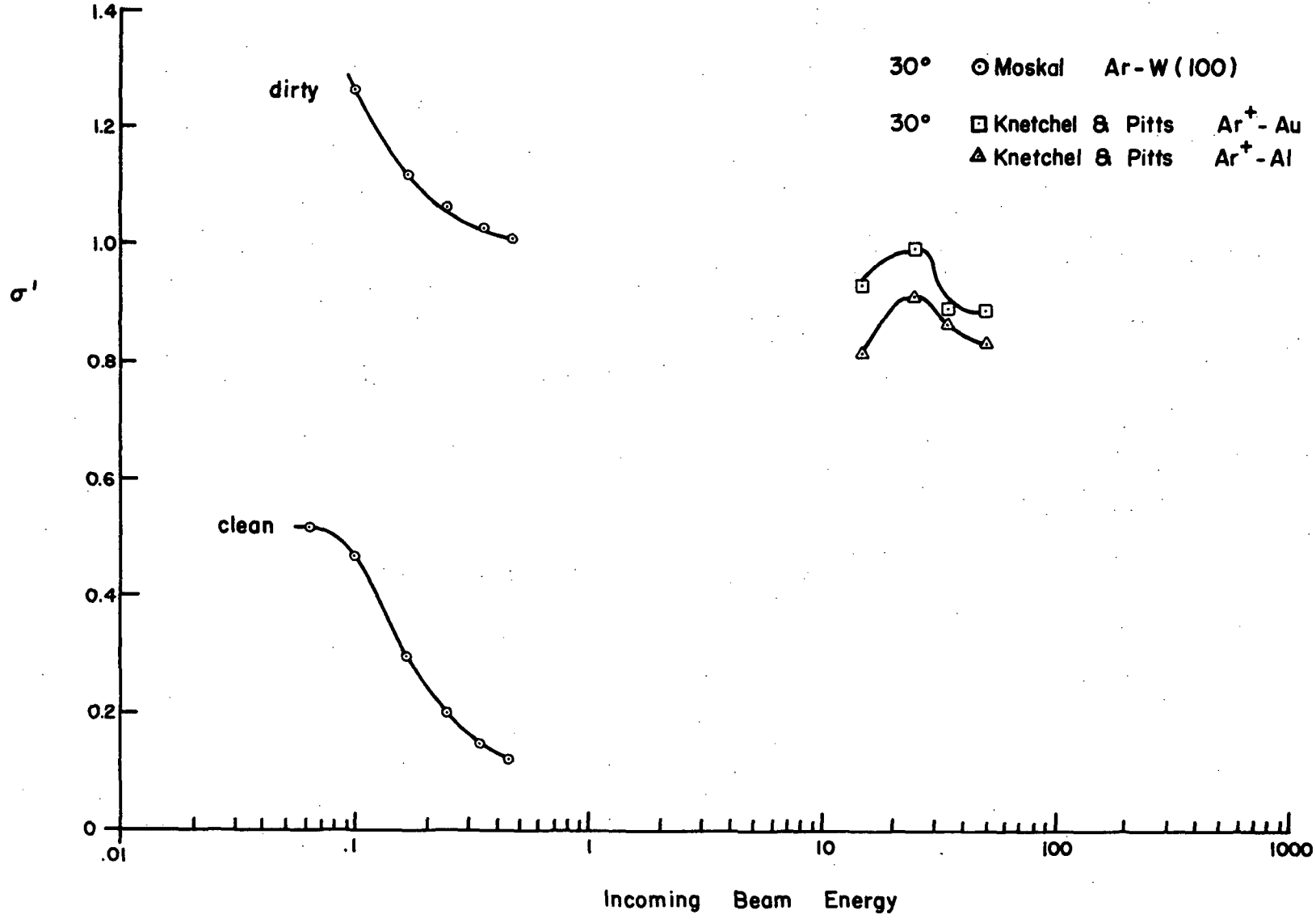

FIG. 54 COMPARISON OF NORMAL MOMENTUM ACCOMMODATION COEFFICIENTS σ' VS INCOMING BEAM ENERGY FOR VARIOUS GAS - SURFACE COMBINATIONS FOR $\theta_i \approx 30°$

TABLE I.

Reference	Surface & Method	Gas	ϕ & $\Delta\phi$	Tdes.	Desorp. Activ. Energy	Monolayer Coverage	Initial Sticking Coefficient	Time to Coverage	Surface Temp. & Comments
Tamm & Schmidt 88	W(100). Pressure vs. time curve after flashing in flowing gas.	H_2		450° β_1 550° β_2		β_2 2.5 x 10^{14} β_1 5.0 x 10^{14} total = 7.5 x 10^{14}	0.14 for $\beta_1 + \beta_2$ up to 2 x 10^{14} part./cm^2		300°K Desorption complete at 750°K
Tamm & Schmidt 83	W(100). 1/4" diameter disc.	H_2			β_1 26.3 kcal/mole β_2 32.3 kcal/mole			1.4 x 10^{16} molec/cm^2 or ~ 1 x 10^{-5} torr.-sec.	
Hopkins & Pender 91	W(100) 6 mm. dia. discs. Zisman (contact potential)	H_2	Φ = 4.65 $\Delta\phi$ = 0.54					5 x 10^{16} molec/cm^2 or ~ 3.5 x 10^{-5} torr.-sec.	H_2 pressure dropped from 10^{-7} to 10^{-10} over 1 hour, & c.p.d. remained constant.
Collins & Blott 92	W(100) selected plane of tip. FEM Fowler-Nordheim plots.	H_2	ϕ = 4.65 $\Delta\phi$ = 1.09						Work function was constant after a pump-down to 1 x 10^{-10} torr, for most planes.
Abey 93	W(100) single crystal foil. Filament & collector method.	H_2	$\Delta\phi$ = 0.21				0.63		
Estrup & Anderson 76	W(100) foil. FEM	H_2	$\Delta\phi$ = 0.9			11.5 x 10^{14}. assumes full coverage 10 x 10^{14}	0.66	2.5 x 10^{-6} torr.-sec.	
Armstrong 94	W(100). 3 mm. dia. buttons LEED. Electrons electrostatically retarded at surface	H_2	$\Delta\phi$ = 0.88				0.1	5 x 10^{-6} torr.-sec.	
Estrup Anderson 95	W(100). LEED	N_2	$\Delta\phi$ = -.65	<1200°K		4 x 10^{14}, assumes full coverage 5 x 10^{14}	0.55	1.4 x 10^{-6} torr.-sec.	T = room temp. One desorption peak
Van Oostrom 96	W(100) selected plane of emitter. FEM Fowler-Nordheim plot.	N_2	ϕ = 4.65 $\Delta\phi$ = -.31				0.25		

TABLE I (continued)

Reference	Surface & Method	Gas	ϕ & $\Delta\phi$	T_{des}	Desorp. Activ. Energy	Monolayer Coverage	Initial Sticking Coefficient	Time to Coverage	Surface Temp. & Comments
Delchar & Ehrlich 97	W(100) button Contact Potential	N_2	$\phi = 4.7$ $\Delta\phi = -.4$	>1000°K	75 kcal/mole			0.7×10^{15} molec/cm^2 or 1.8×10^{-6} torr-sec.	1 peak. T_s = 300°K. 100% desorp. of monolayer after 3.5 sec. for T_s > 1000° K.
Estrup & Anderson 98	W(100) foil. LEED Retarding potential method.	CO	$\Delta\phi = 0.43$ $\Delta\phi = -.16$ (heated)	β_L 1150°K β_H 1380°K		~ 1×10^{15}		3.6×10^{-6} torr-sec.	Room Temperature
Armstrong 99	W(100)	CO	$\Delta\phi = 0.38$				0.25	1×10^{-7} torr-min.	for P = 3×10^{-9} torr.
Hopkins & Pender 100	same as above (Ref. 66)	O_2	$\Delta\phi = 1.6$	1800°K (110)Surf.				1×10^{17} molec/cm^2	Surface cleaned at 2500°K
Bell, Swanson, Crouser. 101	W(100) selected plane of emitter. FEM Fowler-Nordheim	O_2	$\phi = 4.4$ $\Delta\phi = 1.5$ at 78°K						Shows that heating to $T_s \geq$ 2000° gives ϕ typical of clean surfaces.
Engel & Gomer 102	W(100). FEM	O_2	$\Delta\phi = 1.4$ at 100° K						Monitor surface condition by recording No. of doses.
Estrup & Anderson 103	W(100). Retarding Potential method.	NH_3	$\Delta\phi = -.1$	1375°K			> 0.45	5×10^{-6} torr-sec.	Adsorption at room temp. is non-dissociative
Hughey & Waclawski 104	W poly. ribbon. Static capacitor meth.	H_2O	see comments					6×10^{-6} torr-sec.	$\Delta\phi$ changes from max. of + .45 to + .2 as OH displaces H.
Engel & Gomer 105	W(100) FEM	Ar	$\Delta\phi = -.46$ at 4.2°K	24° multi 34° mono	Binding Energy 1.9 kcal/mole	7.9×10^{14}			
Muller - McLane Panitz 106	W	He			Adsorption energy ~ 300 kcal/mole				He not adsorbed on metals at temp. as low as 21°K.